Nanoporous materials for optical applications

Dissertation

zur Erlangung des akademischen Grades
des Doktors der Naturwissenschaften
der Naturwissenschaftlich-Technischen Fakultät
der Universität des Saarlandes

Seongjun Kim

Saarbrücken, 2020

Tag des Kolloquiums:	04.12.2020
Dekan:	Prof. Dr. Jörn E. Walter
Berichterstatter:	Prof. Dr. Eduard Arzt Prof. Dr. Rainer Birringer
Vorsitzender:	Prof. Dr. Martin Müser
Akad. Mitarbeiter:	Dr.-Ing. Frank Aubertin

Table of contents

Acknowledgement

This work was done in the Optical Materials group at the INM - Leibniz Institute for New Materials in Saarbrücken. Without the support of many colleagues at INM, it would not have been possible to do my work. I would like to sincerely thank for all the helps.

First of all, my thanks go to PhD supervisor Prof. Dr. Eduard Arzt and my group leader Dr. Peter W. de Oliveira for the possibility of this work at INM and the numerous supports during this time. Likewise, I would like thank Prof. Dr. Birringer for the role as the second reviewer of my doctoral thesis.

Special thanks go to Dr. Peter König, who had been always there and open for every question and discussion during the entire period of my PhD. Without his support, it would not have been possible to complete my work. I would like to also thank Dr. Peter Rogin for his support, especially for the laser experiment and discussion. I appreciated for countless support and help from the other colleagues in the Optical Materials group. I need to mention my special thanks to Bruno Schäfer and Jenny Kampka for the experiments and measurements.

Finally, I would like to sincerely thank my family in South Korea for their support and encouragement, and, *last but not least*, my wife Hyejeong Lee for your love and unconditional support through all these years. Glad that I have you in my life.

Kurzzusammenfassung

In dieser Arbeit wurde ein neues Verfahren zur Herstellung von Nanobläschen in transparenten Polymeren entwickelt. Die azo-chemischen Initiatoren AIBN (Azobisisobutyronitril) und ABVN (2,2'-Azobis(2,4-Dimethylvaleronitril)) wurden als chemische Treibmittel (CBA) verwendet, die Stickstoff zur Bildung der Blasen abgeben. Der Photoinitiator Irgacure 819, der durch längeres UV-Licht (405 nm) als AIBN (345 nm) aktiviert werden kann, wurde zu der Lösung gegeben, um die Zersetzung der Azochemikalien während der ersten Stufe, der Probenvorbereitung durch UV-Vorhärtung, zu minimieren. Die nicht umgesetzten CBAs, zersetzten sich bei Erwärmung und fungierten als Treibmittel. Die Bedingungen der Aufschäumprozesse wurden variiert, um kritische Faktoren zu untersuchen, die Keimbildung und Wachstum von Blasen beeinflussen. Die Ergebnisse wurden auf der Grundlage der Thermodynamik im Kontext der konventionellen Keimbildungstheorie diskutiert. Die schrittweise Optimierung dieser Faktoren führte zur Erzeugung von Nanobläschen. Diese Technik könnte allgemein auf UV-härtbare Polymersysteme anwendbar sein. Dieser neuartige Ansatz wurde verwendet, um für optische Anwendungen Prototypen herzustellen, wie z.B. Beschichtung von Sicherheitsmarkierungen und Lichtauskopplung in optischen Wellenleitern.

Diese Studie liefert auch wichtige Informationen zu Keimbildung und Wachstum von Blasen im metastabilen Zustand von Polymeren, die zur Verifizierung der Hintergrundtheorien beitragen könnten.

Abstract

In this work, a new process of generating nanobubbles[*] in transparent polymers was developed. The azo-chemical initiators AIBN (Azobisisobutyronitrile) and ABVN (2,2'-Azobis(2,4-dimethylvaleronitrile)) were used as chemical blowing agents (CBA) that deliver nitrogen gas to form the bubbles. Specifically, the photo initiator Irgacure 819, which could be activated by a longer wavelength of UV (405 nm) than that of AIBN (345 nm), was added to the solution in order to minimize the decomposition of the azo chemicals during the first stage of sample preparation by UV-pre-curing. As a result, the CBAs remained unreacted, thus they could decompose and be used merely as a blowing agent. In addition, the post-foaming processes were conducted under the different foaming conditions to investigate critical factors affecting the nucleation and growth of bubbles. The results were discussed based on thermodynamics, mainly by conventional nucleation theory (CNT). Finally, stepwise optimization of those factors led to the generation of nanobubbles. This technique could be applicable to UV curable polymer systems in general. This novel approach was used to make prototype optical devices, such as security mark coating and light out-coupling in optical waveguide.

This study also gives important information about the nucleation and growth of bubbles in meta-stable state of polymers, which could help to verify the background theories.

* Nomenclature of nanobubble

According to ISO/TC 281 and ISO 20480-1 (**Figure 1**), a bubble smaller than 100 µm in size is considered as ‘fine bubble’. The bubble range from 1 to 100 µm is defined as ‘microbubble’, whereas a bubble smaller than 1 µm is called ‘ultrafine bubble’. In this work, I used the term ‘nanobubble’ instead of ultrafine bubble to describe sub-micron bubble and to distinguish with ‘microbubble’. In the field of nanoparticles, the term ‘nano’ is generally applied only to the particles that are less than 100 nm in size. [1]

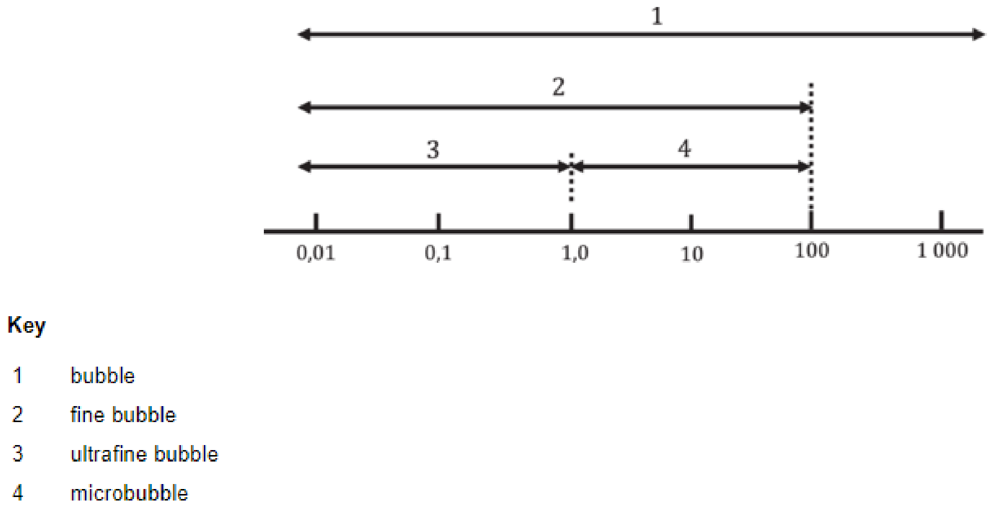

Figure 1. Scale diagram showing bubble diameters (dimensions in µm) – ISO 20480-1 (2017)

List of abbreviations

ABS: Acrylonitrile butadiene styrene

ABVN (V- 65): 2, 2'-Azobis (2,4-Dimethylvaleronitrile)

ADCA: Azodicabonamide

AIBN: 2, 2´-Azobis (2-methylpropionitrile)

AR-coating: Antireflective coating

CBA: Chemical blowing agent

CNT: Classical Nucleation Theory

CW: CO_2-in-water emulsion

DLS: Dynamic light scattering

DSC: Differential scanning calorimetry

EGDMA: Ethyleneglycol dimethacrylate

HEMA: Hydroxyethyl methacrylate

HIPE: High internal phase emulsion

LDUPR: Low-density unsaturated polyester resin

LPBC: Laplace pressure bubble catastrophe

MAM: Methylmethacrylate – butylacrylate – methylmethacrylate

MTMS: Methyltrimethoxysilane

NRHB: Nonrandom Hydrogen-Bonding Model

OM: Optical microscope

O/W: Oil-in-water emulsion

PLA: Polylactic acid

PBA: Physical blowing agent

PDMS: Polydimethylsiloxane

PES: Polyethersulfone

PESQ: Polyethylsilsesquioxane

PETA: Pentaerythritol triacrylate

PFMA: Perfluorooctylethyl methacrylate

PFS: 4-(perfluorooctylpropyloxy) styrene

PHEMA: Poly (2-hydroxyethyl methacrylate)

PMMA: Poly (methyl methacrylate),

PP: Polypropylene

PS: Polystyrene
PSU: Polysulfone
PVSQ: Polyvinylsilsesquioxane
SAD: Supercritical alcohol drying
SCD: Supercritical CO_2 drying
SCF: Supercritical Fluid
SEM: Scanning electron microscopy
sPMMA: syndiotactic Poly (Methyl Meth Acrylate)
STP: Standard temperature and pressure, 0 °C and 1 atm
TEOS: Tetraethoxysilane
TMAOH: Tetramethylammonium hydroxide
UPR: Unsaturated polyester resin
UV**:** Ultraviolet
V-70: 2, 2'-Azobis (4-Methoxy-2,4-Dimethylvaleronitrile)
W/O: Water-in-oil emulsion

1. Introduction

There are lots of interesting examples in our daily life related with the properties of light. For example, a beautiful rainbow in the sky after a shower is attributed to the 'refraction' of light between water droplets and air. Likewise, a pencil in water seems to be shifted and an object in the water looks closer than what it really is. In physics, refraction is the change in direction of a wave passing from one medium to another or from a gradual change in the medium. The dimensionless refractive index '*n*' is defined as

$$n = c / v$$

c: speed of light in vacuum
v: velocity of light in various medium

It describes, by the definition, how fast light goes through the material. In other words, the velocity of light changes depending on the medium. The smaller the refractive index is (close to 1), the faster light goes through the material. For example, a material with refractive index of 1.5 has the velocity of 66.7 % (i.e. 1/1. 5 = 0.666) compared to that in vacuum. Therefore, when light passes from one substance to another, the path of the light changes, resulting in refraction according to Snell's formula,

$$n_1 \sin(\theta_1) = n_2 \sin(\theta_2)$$

n_1, n_2: refractive index of material 1 and 2
θ_1: incident angle, θ_2: refracted angle

In addition, the difference in the refractive index also affects the amount of light reflected from the interface, according to Fresnel equations [2].

$$\textit{Reflectivity (R)} = \frac{(n_1 - n_2)^2}{(n_1 + n_2)^2} \textit{ at normal incidence}$$

$$\textit{Transmittivity} = 1 - R$$

n_1, n_2: refractive index of material 1 and 2

For example, the reflectance and transmittance from an air-glass interface, when n_1 (air) = 1 and n_2 (glass) = 1.5, are 4% and 96 % respectively. Since most optical properties are directly related to the refractive index ‘n’, it is one of the most important factors in optics.

It is worth to note that the refractive index usually increases from gases, liquids, and solid state in that order when the density of the substance increases. A remarkable exception of decreasing refractive index from liquid to solid is found only for water, caused by crystallization of ice that leads to so-called density anomaly.

Table 1 and **Table 2** show the refractive index, n, of most widely used materials and their states.

Materials	**Average Refractive index**
Al_2O_3 (corundum, sapphire)	1.76
C (diamond)	2.417
$CaCO_3$ (calcite)	1.65
CaO (lime)	1.84
Glass, flint	1.65
Glass, Soda-lime-silica	1.51 - 1.52
Glass, silica	1.458
Glass, borosilicate (Pyrex)	1.47
H_2O (l)	1.33
H_2O (s)	1.30
MgF_2	1.38
SiO_2 (quartz)	1.55
TiO_2 (rutile)	2.68
TiO_2 (anatase)	2.55
ZrO_2	2.1 - 2.2

Table 1. Refractive index of ceramics, glasses, and ionic solids **[3]**

Materials	**Average Refractive index**
Epoxies	1.55-1.60
Polyamides; Nylon 66	1.53
Polycarbonate	1.586
Polyester	1.52 - 1.57
Polyethylene, low density	1.51
Polyethylene terephthalate	1.64
Polyethylene, high density	1.545
Polymethylmethacrylate	1.49
Polypropylene	1.47
Polystyrene	1.59
Polyvinyl chloride	1.54 - 1.55
Polyvinylidene fluoride	1.42
Urethanes	1.5 - 1.6

Table 2. Refractive index of polymers **[3]**

Although the refractive index represents an intrinsic value of materials at each state and structure, it could be tuned when two different materials combine and form a composite, according to Lorentz-Lorenz equation as shown in **Equation 1 [4]**.

$$\frac{n^2-1}{n^2+2}\cdot\frac{M}{\rho}=\sum_{i=1}^{m}\frac{n_i^2-1}{n_i^2+2}\cdot\frac{f_iM_i}{\rho_i}$$

Equation 1. Lorentz - Lorenz equation

where, n is the refractive index of a composite material of average molecular weight, M, and density, ρ, whose constitution is m materials each of mole fraction, f_i, molecular weight, M_i, and density, ρ_i.

The Lorentz-Lorenz equation indicates the effect of density and volume fraction of the composite material on refractive index. Apparently, the refractive index, n, of transparent polymers could be increased relatively simply by making composites with other materials which have higher refractive index than that of matrix polymers. For example, materials such as TiO_2 (where n are 2.55 and 2.68 for anatase and rutile) and ZrO_2 (where n is 2.1 - 2.2) could be used for increasing the refractive index. When it comes to optical applications, however, simply increasing the volume fraction of materials with high refractive index is not enough because a certain level of transparency is required in most cases. In other words, the size of added materials also matters, since light is scattered by inclusions. The bigger the particles are, the more light scatters, making materials opaque as shown in **Figure 2** [5], the so-called Rayleigh equation.

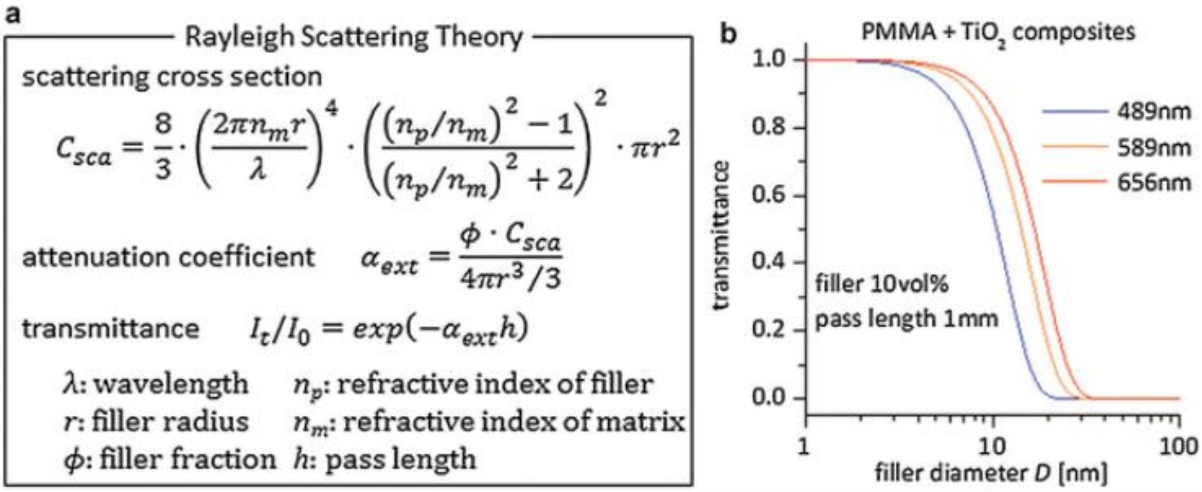

Figure 2. Scattering loss by Rayleigh scattering (a) scattering theory (b) an estimated example based on the theory. Reprinted from [5] with permission, copyright (2014) Springer Nature

Therefore, ZrO_2 nanoparticles, for example, below 10 nm have been widely used to increase the refractive index of transparent organic-inorganic hybrid coatings [6-8], considering the wavelength of the visible, 380 – 740 nm. That explains why the particles should be 'nanoparticles' especially in optics to minimize scattering effect. It should be noted from the equation that not only the size, but also the volume fraction of the particles also matters, meaning higher contents of the particles lead to low transmittance.

To reduce the refractive index, on the other hand, is more challenging because there is almost no such material that has a refractive index lower than 1.3 (ice), except gases. Teflon AF has the refractive index in the range of 1.29 – 1.31 [9]. However, the refractive index of amorphous PTFE is around 1.356. Furthermore, dissolved gas in water has little effect on the refractive index, around 10^{-6} to 10^{-4} [10]. Therefore, it seems that one possible way to reduce the refractive index of transparent materials is to create nano-porous structures. By the Lorentz-Lorenz equation, the refractive index of PMMA, 1.49, could be reduced by increasing the volume fraction of nitrogen gas, as nanobubbles, in the matrix as shown in **Figure 3**.

Based on the calculation, a PMMA film with 40 % volume fraction of nitrogen, which has the refractive index of 1.23, would be a perfect candidate for an AR (Anti-reflection) coating.

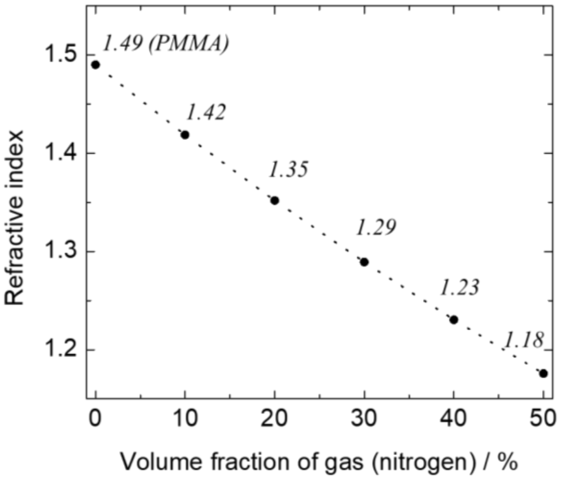

Figure 3. Refractive index of PMMA depending on the different volume fraction of nitrogen (N_2)

However, it is very difficult to fabricate nanoporous material starting from generation of nanobubbles, followed by continuous freezing. Furthermore, the existence and the stability of nanobubbles in liquid is still controversial in terms of thermodynamics [1]. This theoretical problem will be discussed in detail in the next chapter. Therefore, porous silica or CVD MgF_2 (refractive index: 1.38 _ **Table 1**) coating is widely used for low refractive index materials in practical applications due to the difficulty of fabricating nano pores directly from gas.

The aim of the study is to develop an appropriate and cost-effective method to generate nanobubbles in transparent polymers for optical applications. Firstly, in literature research section, the challenges to generate nanobubbles are reviewed based on the thermodynamic theory. In addition, current methods to fabricate nano porous materials as well as their advantages and disadvantages are reviewed and summarized.

In the main part of this thesis, the potentials of using chemical blowing agents to generate nanobubbles are investigated and evaluated. Crucial preparation conditions (e.g. temperature, pressure, surface tension, and so on) influencing the nucleation and growth of bubbles are tested and optimized stepwise based on the theories and results in order to achieve a transparent polymer with nanobubbles. The aim of each experiment will be explained and discussed in detail.

Furthermore, two different prototype optical devices (i.e. a transparent security mark and an out-coupling point for optical wave guide) for optical applications are developed which prove that this technique has a large potential to be exploited in various industry fields.

Finally, the entire progress optimized during this study will be summarized and promising ways to reduce the refractive index further in the future will be suggested.

2. Literature

2.1 Gases in solid materials - Laplace pressure of bubbles in liquid

The strategy to produce nanobubbles in solid materials seems straightforward. First, the desired volume fraction of nanobubbles with targeting size should be injected or generated in monomer solution. The solution containing the bubbles should be solidified or gelled continuously afterwards to freeze the structure, and hence keeping the bubbles stable. However, as it was already mentioned before, each step is hardly possible, especially when the size of bubbles is getting smaller. For example, considering a single gas bubble in liquid, the internal pressure of the bubble would increase with respect to the surrounding. This is the so-called Young-Laplace pressure and was derived by Young and Laplace as [11],

$$\Delta P = \frac{2}{r}\,\gamma$$

Equation 2. Laplace pressure – pressure difference in a spherical gas bubble

where, ΔP is the pressure difference between inside and outside of a spherical bubble of radius r, and the surface tension, γ.

Table 3 shows the ΔP inside an air bubble in water, for example, depending on its size, where $\gamma = 72$ mN/m at 25°C [12].

Diameter of bubble (μm)	ΔP (Pa)	ΔP (atm)
10.0	28,800	0.28
1.0	288,000	2.84
0.1	2,880,000	28.42
0.01 (10 nm)	28,800,000	284.23

Table 3. The pressure inside an air bubble in water

Since the internal pressure of a bubble is higher than that of the surroundings, the bubble could be in equilibrium only if the surrounding solution is supersaturated. In other words, the partial pressure of the bubble is higher than that of 'equilibrium' pressure of the surrounding. For instance, ΔP inside in an air bubbles of diameter 10 nm is 284 atm. Therefore, the gas would diffuse into the solution by Henry's law and disappear very fast by shrinkage. That is why making a gas bubble in equilibrium is impossible, particularly for small bubbles.

Regardless, let us assume a single gas bubble in a solution which is initially supersaturated. A small perturbation of the surrounding could make the bubble either slightly bigger or smaller. If the size of the bubble slightly increases, that would lower the Laplace pressure in the bubble, resulting in more diffusion of gas from the surrounding into the bubble - positive loop. This would make the bubble keep growing until they flow up to the surface by buoyancy. On the other hand, for a negative loop of getting smaller, the bubble would keep shrinking and disappears at the end due to the spontaneous increase of the Laplace pressure in the bubble, increasing the solubility of the gas. That is the so-called Laplace pressure bubble catastrophe (LPBC), implying small bubbles can never be thermodynamically stable [1].

According to the theory from Epstein and Plesset [13], "A gas bubble in a liquid-gas solution will grow or shrink by diffusion accordingly as the solution is oversaturated or undersaturated". From their study, the lifetime of bubbles smaller than 1 μm in saturated solutions is less than 0.02 sec, making it almost impossible to detect or measure the bubbles (**Figure 4**).

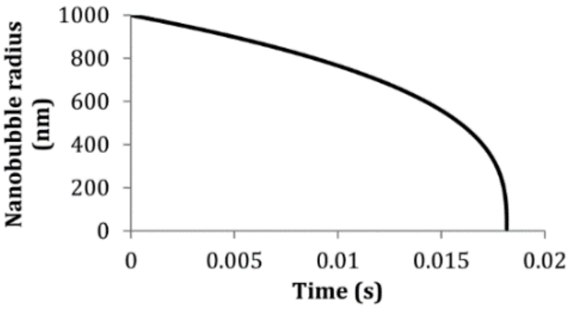

Figure 4. Calculated nano bubble radius versus time using the Epstein and Plesset theory for a nitrogen-filled nano bubble of initial radius 1000 nm in a solution that is saturated with dissolved nitrogen gas. (T = 300 K, γ = 0.072 J m^{-2}, D = 2.0×10^{-9} m^2 s^{-1}, C_{sat} = 0.6379 mol m^{-3}, $\rho_{1\ atm}$ = 40.6921 mol m^{-3})
Reprinted with permission from **[1]**. Copyright (2016) American Chemical Society.

Nevertheless, a lot of studies have proven the evidence of long-term stability of bubbles below 1 μm. For example, Johnson et al. reported the stability of bubbles less than 1 μm in sea water [14] and Bunkin et al. studied the charged sub-micron bubbles in diluted solutions [15, 16]. Other approaches of generating submicron bubbles such as sonification [17], electrolysis [18, 19], and gas injection [20, 21] were also reported. In these ways, such small bubbles could be stable much longer than what is expected by Epstein and Plesset theory. Previous studies have suggested that the main reason for the stability of bubbles is due to the existence of surfactants, hydrophobic nanoparticles, and adsorbed ions that cover the interface of the bubbles, and protect bubbles from collapse. Although there have been many studies and different hypothesis, the stability of nanobubbles is still controversial since it is hard to visualize. Moreover, most of the studies were conducted in liquid state and evaluated by DLS (dynamic light scattering) or by measuring zeta potential or density. There has been no report about nanobubble found in solidified polymer starting from monomer or liquid sol.

In conclusion, the so-called LPBC implies that nanobubbles are thermodynamically never stable [1] and the mechanism of the stability of the bubbles has not been clearly understood.

In the following chapters, I review different methods for introducing gas directly into polymers, i.e. foaming by chemical or physical blowing agent. I compare their microstructure with other materials fabricated by indirect ways such as precipitation polymerization, block-co-polymerization (BCP), high internal phase emulsion (HIPE), and aerogel process.

2.2 Chemical and physical blowing agents

Blowing agents are substances that could produce gas molecules in the materials and could be classified into chemical and physical blowing agents.

Chemical blowing agents (Azo chemicals)

Chemical blowing agents include isocyanates, sodium bicarbonate, and other nitrogen-based chemicals. They produce CO_2, CO, nitrogen, and ammonia gases depending on their chemical composition. Among them, nitrogen-based azo initiators are possible candidates for thermoplastic and elastomeric polymer foams since the azo group (R-N=N-R') could decompose under UV radiation and/or thermal heating into two free radicals and one nitrogen gas molecule as shown in **Scheme 1** [22, 23].

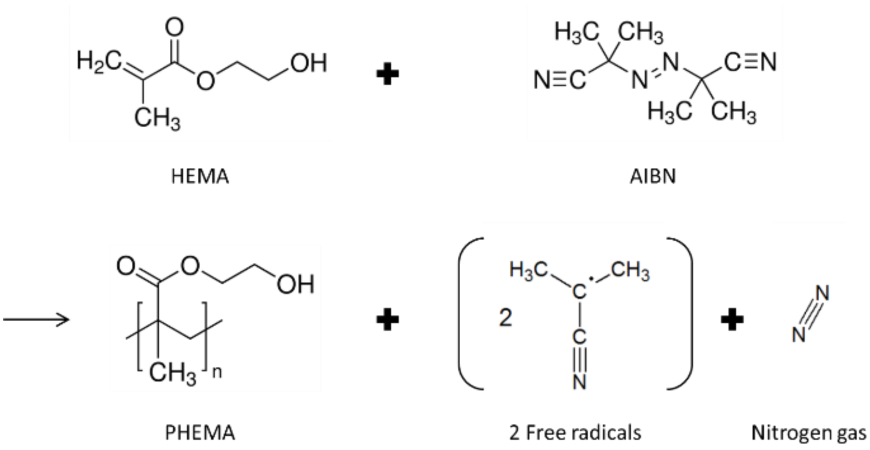

Scheme 1. Free radical polymerization of PHMEA and N_2 production by AIBN decomposition

The free radicals mainly initiate polymerization at relatively low temperature of 60 – 80 °C [24, 25]. Meanwhile, nitrogen gas (N_2) could either be dissolved in the metastable matrix or it forms bubbles when the matrix is supersaturated by gas. In other words, the formation of bubbles and polymerization occurs simultaneously when the reaction starts from a liquid mixture at low viscosity, making it difficult to control the size and density of bubbles. Due to the difficulty of controlling continuous polymerization reaction, this method is not well recommended. For example, Přádný, M. et al. compared five different methods for preparing macroporous hydrogel including crosslinking polymerizations, lyophilization, electrospinning, and addition of azo initiator AIBN [26]. **Figure 5** represents the typical porous structures depending on the processes. They concluded 'the least suitable method seems to be the preparation of porous hydrogels by polymerization using gas (nitrogen) releasing initiator, 2,2´-azobisisobutyronitrile (AIBN)'. The shape of pores was vertically oriented because of the nitrogen flow by buoyancy.

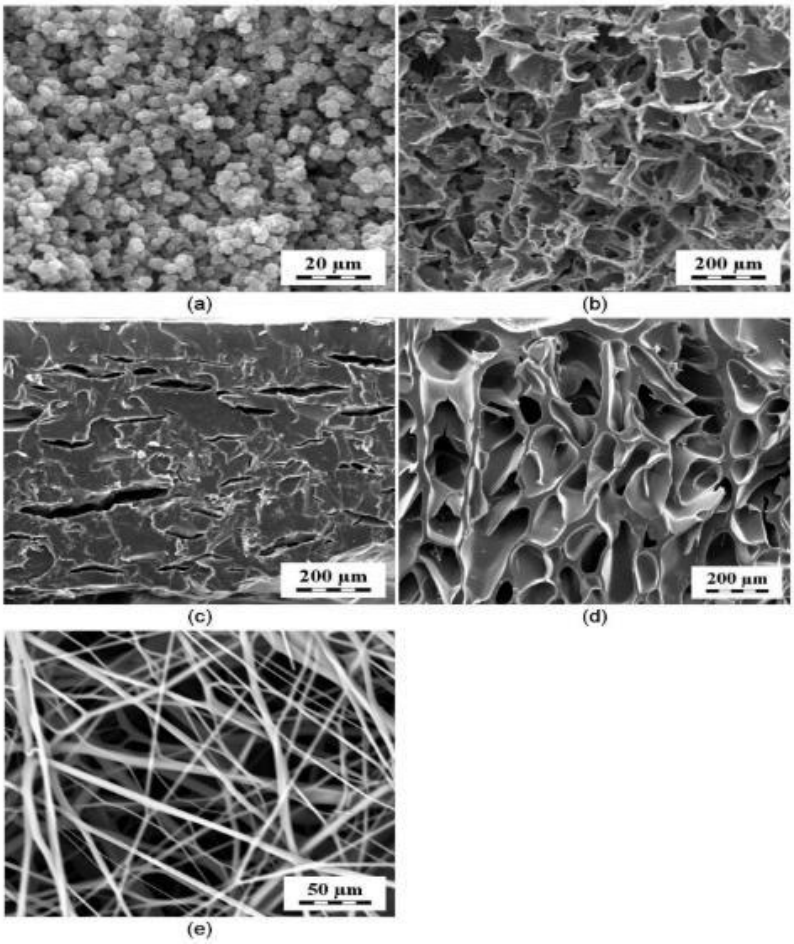

Figure 5. SEM micrographs of macro porous hydrogels. Porosity caused by (a) precipitation polymerization of HEMA in dodecan-1-ol – cyclohexanol mixture, 1/1.5 (v/v), (b) polymerization in the presence of NaCl particles (200 – 250 μm), (c) polymerization in presence of (0.7 g AIBN /3.8 g HEMA), (d) lyophilization of HEMA-MA (26 wt. % MA) copolymer and (e) by voids between poly (HEMA) nanofibers.
Reprinted from [26] with permission.

In addition, in one study by Liang-Zhi Guo et al., AIBN and ABVN were used as main and assistant foaming agents to fabricate low-density unsaturated polyester resin (LDUPR) as shown in **Figure 6**. Although there was an improvement in terms of homogeneity and the apparent density of their LDUPR was 0.37 g/cm^3 under the optimized condition, the size of the bubbles was still around 100 µm as shown in **Figure 7** [27].

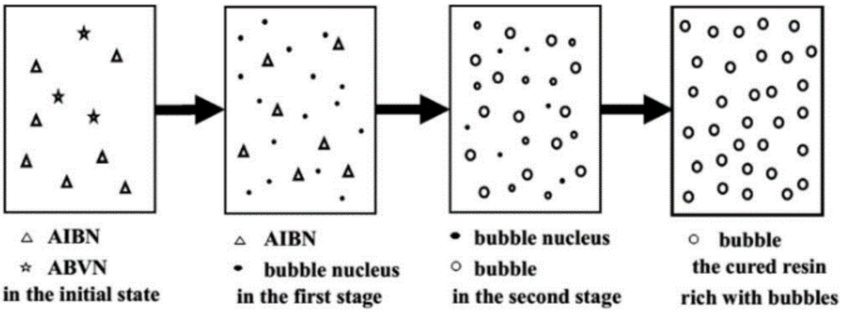

Figure 6. Dual-foaming mechanism of the composite foaming agent for UPR (a) in the initial state, (b) in the first stage, and (c) in the second stage and (d) the cured resin rich with bubbles.
– Reprinted from [27] with permission.

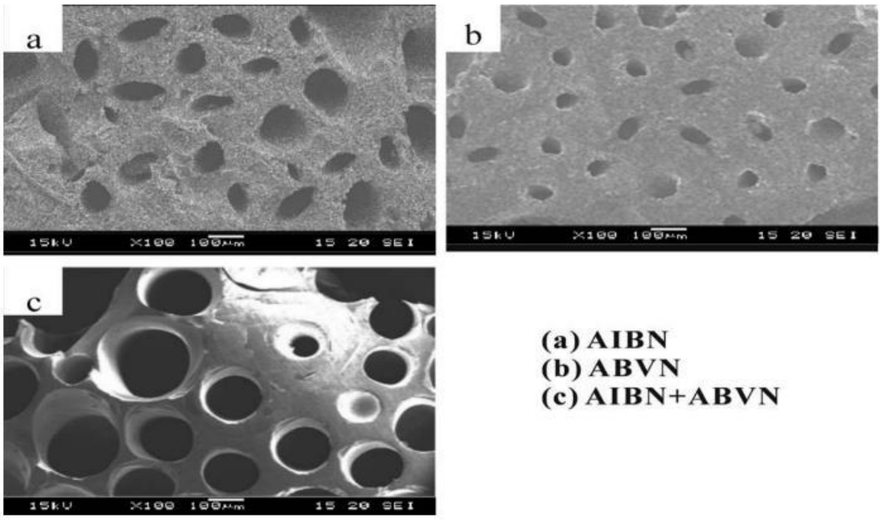

Figure 7. SEM micrographs of LDUPR with different kinds of foaming agents
– Reprinted from [27] with permission.

Therefore, commercially available chemical blowing agents are used not for continuous polymerization but for extrusion or injection molding. Azodicarbonamide (ADCA), called a 'yoga mat' chemical, is one of the most widely used chemicals in the production of various foams and it reacts around 200 °C [28-30]. Since ADCA has relatively higher decomposition temperature around 130 – 220 °C, it could stay unreacted until the foaming process. The reaction temperature of ACDA could be tuned by adding additives to control the properties of the foams [29, 30]. However, materials produced at high temperature by extrusion or injection molding are usually colored or opaque because of the light scattering caused by micro pores. Therefore, they are not appropriate for transparent optical materials.

In summary, there are mainly two types of nitrogen-based chemical blowing agents. One is used as an initiator in liquid state to trigger the polymerization at low temperature, generating nitrogen. Until now, the generation of nitrogen gas has been always considered as a problem in conventional polymerization process due to large pores trapped in polymers. The other one is mainly used for extrusion or injection molding at higher temperature. However, unfortunately, none of those could realize nano pores with transparency. Using azo initiators does not seem to be a promising way to produce nanobubbles without groundbreaking improvement.

Physical blowing agent (supercritical CO_2)

Since the generation of nanobubbles by chemical blowing agents is hardly possible, an alternative foaming process using supercritical fluid (SCF) CO_2 becomes one of the alternative ways to introduce porosity in rigid materials. CO_2 is one of the most used substances for the physical foaming because its supercritical point is relatively easy to reach (31 °C, 73 atm) [31] as shown in **Figure 8**. For example, the solubility of CO_2 in polymers such as PMMA and polystyrene (PS) is much higher than that of N_2 due to the better affinity to hydrocarbon and condensability [32]. Above the critical point, CO_2 has the properties of in between gas and liquid in terms of density, viscosity, and diffusivity. It means that CO_2 could diffuse into materials and be absorbed depending on the saturation conditions and the solubility of CO_2 in the matrix.

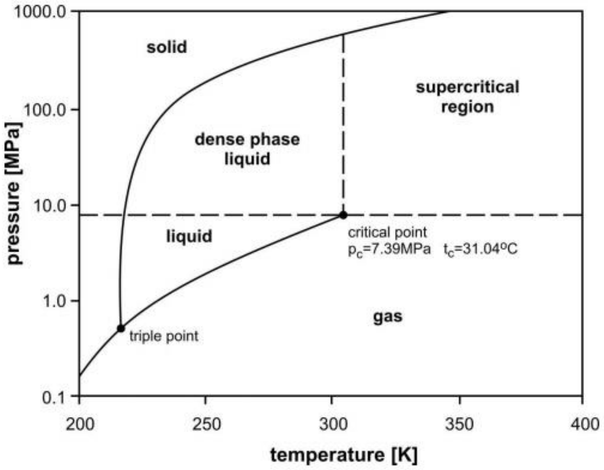

Figure 8. Carbon dioxide pressure-temperature phase diagram [33]

The process starts from putting already cured solid polymers into an autoclave with supercritical fluid CO_2 under the specific conditions. When the external pressure is released, the supersaturated CO_2 starts to form nuclei of bubbles and deforms the materials by ripening and expansion. The reduced solubility for CO_2 in the matrix caused by the fast depressurization is the driving force for the nucleation. As CO_2 forms bubbles or diffuses out, the matrix returns to a glassy state and spontaneously prevents the bubbles from growing. If the depressurization occurs at high temperature near the T_g of the neat polymers, it is called a one-step process (1S) and shown in **Scheme 2** [34].

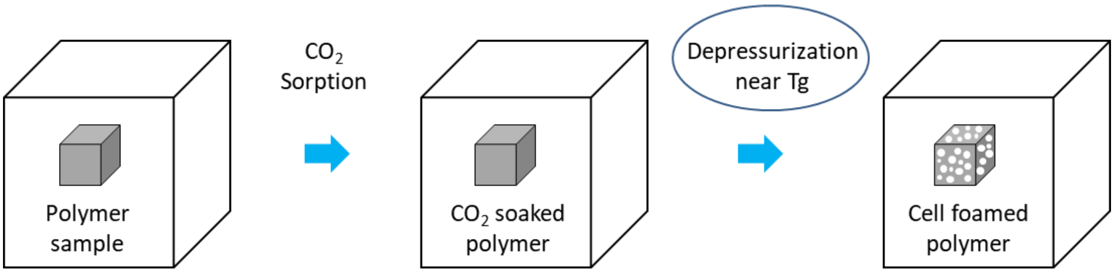

Scheme 2. Pressure induced batch foaming process

Due to the high solubility of CO_2, it is possible to fabricate micro foamed materials at relatively low pressure; below 50 bar. However, in order to reduce the size of bubbles down to 2 - 3 µm, higher saturation pressure (> 350 bar) and rapid pressure drop are required. For example, around 10 – 15 wt% of CO_2 could be absorbed in the neat polystyrene during the one step foaming (1S) depending on the saturation pressure and temperature as shown in **Figure 9**. It should be noted that the glass transition temperature (T_g) of the materials is also reduced as a result of CO_2 absorption [35-37]. Since the weight fraction of CO_2 increases with increasing pressure at a given temperature by Henry's law, the polymer soaked at higher pressure is more supersaturated when the external pressure is released. That makes the size of bubbles smaller while the density of bubbles significantly increases as shown in **Figure 10**. However, the mean diameter of the bubbles foamed at 80 °C and 380 bar was in the range of 2 - 3 µm. It is big enough to scatter the visible light, making the sample opaque. Moreover, it is very dangerous to release the pressure of 380 bar in a short time.

Increasing the foaming temperature, on the other hand, showed a negative effect in terms of the size of bubbles foamed at 100°C as shown in **Figure 11**. There are two possible explanations. First, the amount of CO_2 absorbed in the matrix decreases with increasing temperature, (**Figure 9 (a)**) leading to less supersaturation. Second, the T_g temperature of the CO_2 saturated polymer dramatically decreases down to 30 °C or even below (**Figure 9 (b)**). Although the foaming temperature of 100 °C is below the T_g temperature of the neat polymer (103.8 °C), it is far above the T_g temperature of the CO_2 soaked polymer. Therefore, the matrix expands more easily at the higher temperature, affecting the shape of bubbles as well. Therefore, it is impossible to produce nanobubbles in the neat polymers by 1S CO_2 foaming.

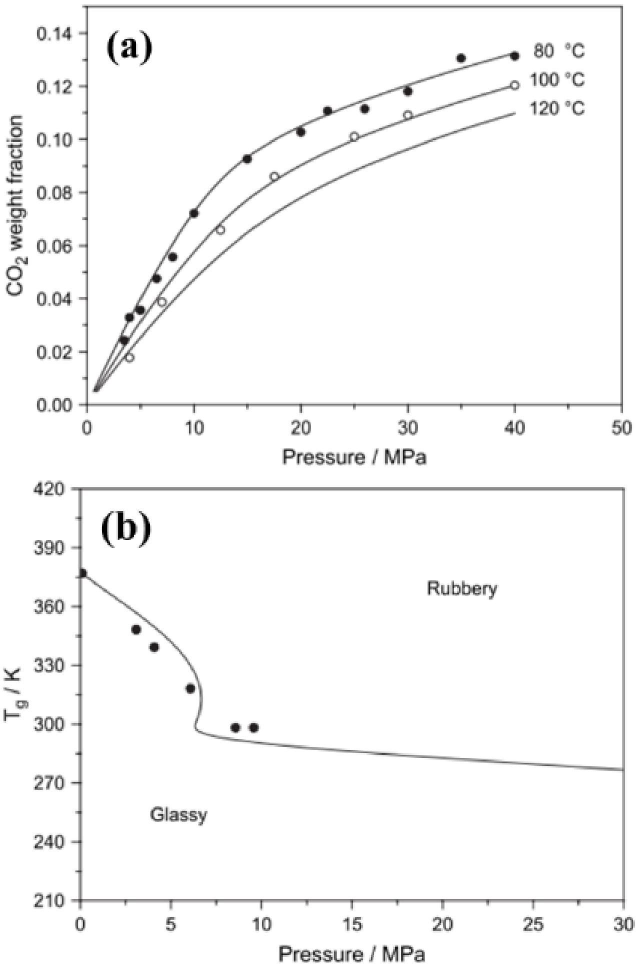

Figure 9. CO$_2$ sorption and glass transition temperature for the polystyrene-CO$_2$ system
(a) CO$_2$ sorption in PS, experimental data (○) 100 °C, (●) 80 °C , (-) NRHB model
(b) Glass transition temperature for the PS-CO$_2$ system: (●) experimental data; (-) NRHB modeling
– Reprinted from [38]. Copyright (2007), with permission from Elsevier.

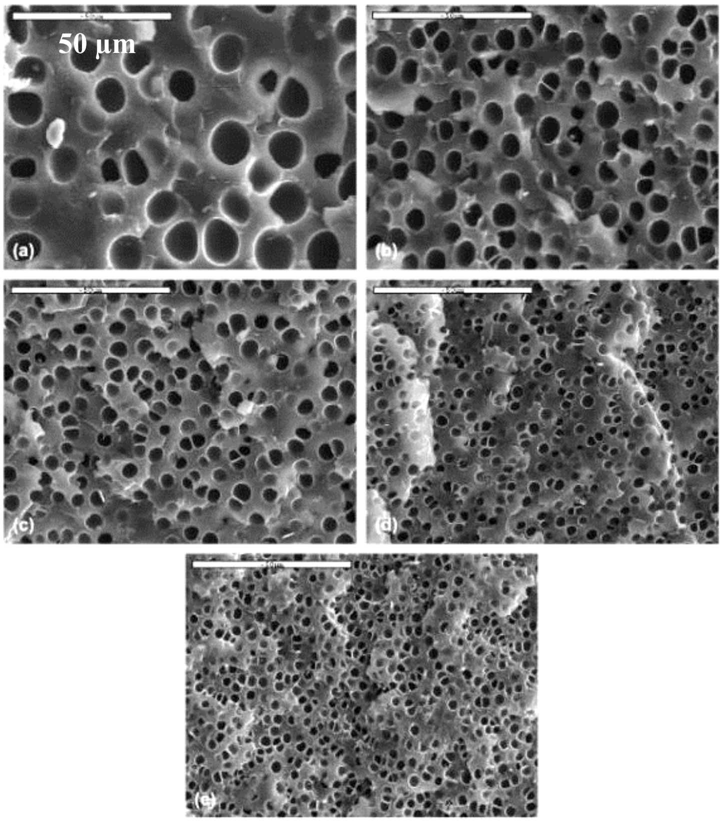

Figure 10. Porous polystyrene (PS) structure (temperature: **80 °C**; pressure: (a) 180, (b) 230, (c) 280, (d) 330, and (e) 380 bar, depressurization time; < 20 sec) scale bar: 50 µm, T_g of the PS : 103.8 °C – Reprinted from [38]. Copyright (2007), with permission from Elsevier.

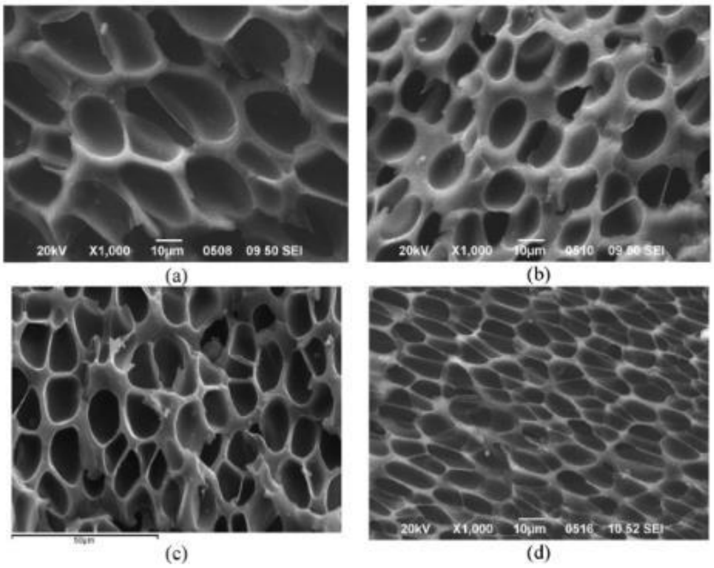

Figure 11. Porous polystyrene (PS) structures obtained at **373.15 K** starting from various saturation pressures: (a) 230 bar, (b) 248 bar, (c) 269 bar, (d) 359 bar – T_g of Polystyrene: 103.8 °C – Reprinted from [39] Copyright (2016), with permission from Elsevier.

Another process, called two-step process (2S), is a way of increasing CO_2 absorption by reducing saturation temperature and pressure so that the matrix could remain below the T_g of the system after releasing the pressure. In other words, the pressure is released at relatively low temperature, near the T_g temperature, so the foaming process could not occur for a while. The process includes afterwards thermal heating by transferring samples into a bath at the foaming temperature - above the T_g temperature of CO_2 impregnated samples - instead of fast pressure drop (1S). It is important to transfer the samples from the autoclave to the foaming bath as fast as possible to minimize the gas diffusion. After being immersed into the bath for a desired time, the samples are cooled down to bring the samples to a glassy state again as shown in **Scheme 3 [34]**.

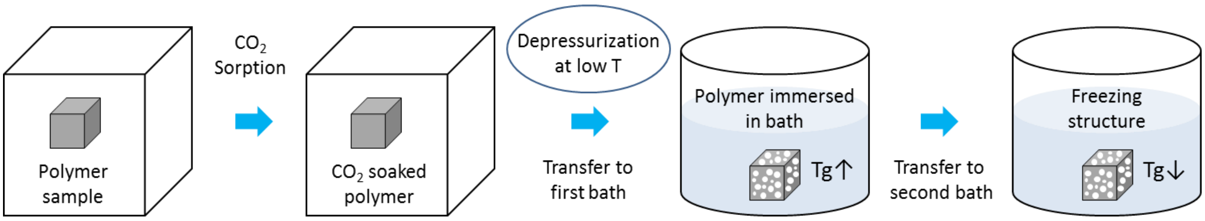

Scheme 3. Temperature-induced bath foaming process.

For example, ABS or PMMA could absorb CO_2 up to 20 wt% at room temperature and 5 Mpa (50 bar), while the matrix is at nearly glassy state as shown in **Figure 12** and **Figure 13**. After that, the foaming process continues below the T_g of the neat polymers in the bath. **Figure 14** shows the PMMA foam fabricated by 2S foaming saturated at 0 °C, 3.2 Mpa and foamed at 90 °C (T_g of PMMA: 112 °C). The density of pores was substantially increased compared to the foams produced by one step foaming. H. Guo et al. reported that the CO_2 absorption in PMMA could be increased up to more than 30% by reducing the saturation temperature below -10 °C [40, 41]. However, the PMMA nano foams from their study have either interconnected porous structure (**Figure 15**) or worm-like nano sturucture rather than nanobubble.

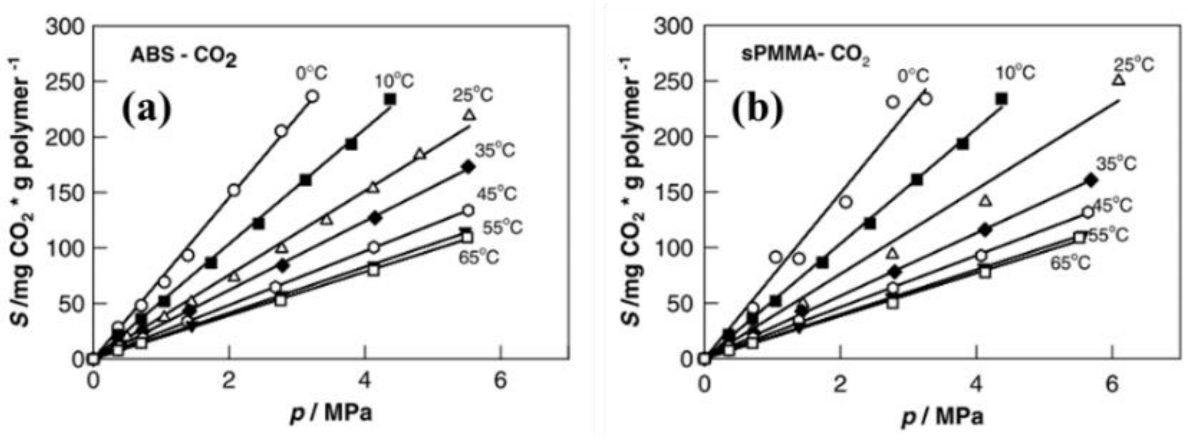

Figure 12. Solubility of CO_2 below T_g of the neat polymer (a) ABS, (b) sPMMA.
The curves are drawn through the points to show the trend in the data. – Reprinted from [42] with permission.

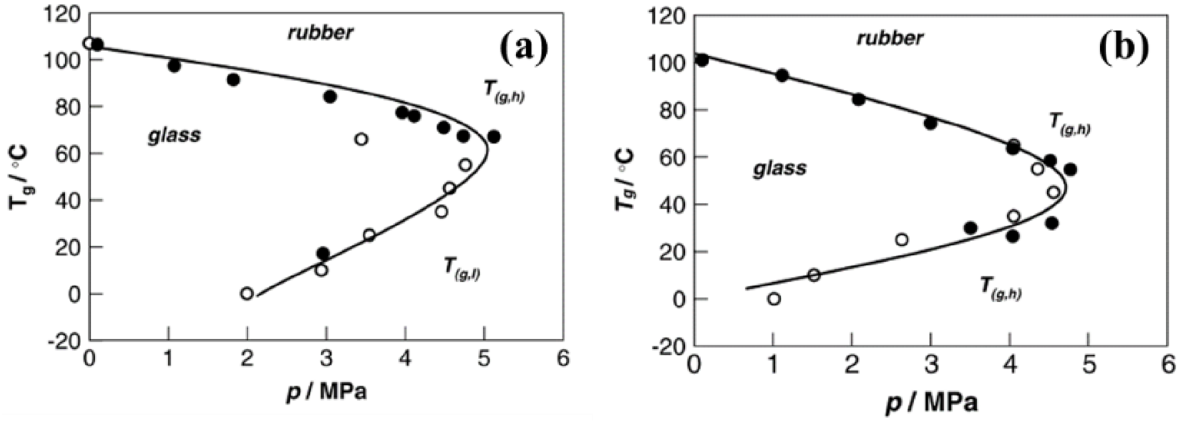

Figure 13. T_g of (a) ABS-CO_2 and (b) sPMMA-CO_2 system as a function of saturation pressure: ○, solubility measurements; ●, DSC measurements. Solid lines are drawn through the points to show the trend.
– Reprinted from [42] with permission.

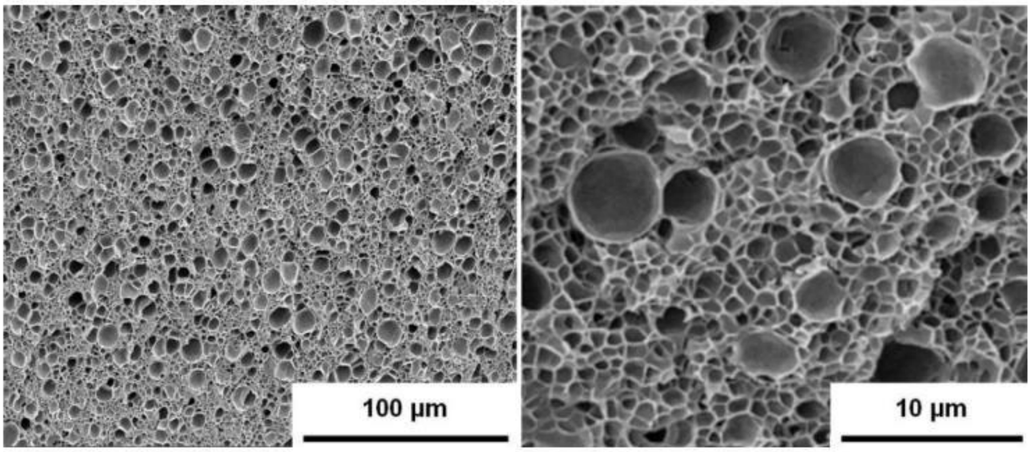

Figure 14. SEM images of PMMA foam. – Saturation conditions: 0 °C, 32 bar, foaming conditions: in a hot water at 90 °C - The PMMA homopolymer (density: 1.19 g cm^{-3}) bath. An average molar mass Mw of 100,000 g mol^{-1} and a glass transition temperature of 112 °C.
Reprinted from [43]. Copyright (2015), with permission from Elsevier.

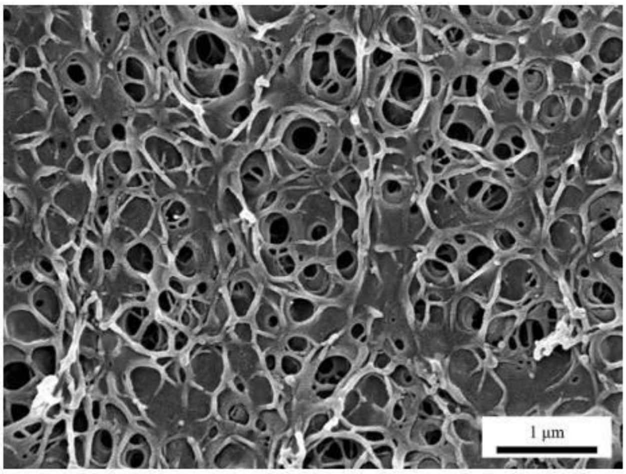

Figure 15. SEM of foamed PMMA. Saturation conditions: -25 °C, 5 Mpa. Foaming temperature : 70 °C, relative density : 23.4 %. Average cell size : 120 nm.
Note that pores are interconnected, indicating porous nature of the structure.
– Reprinted from [41]. Copyright (2015), with permission from Elsevier.

There are also several variations based on these two processes such as blending different polymers that have different CO_2 affinity. For example, Pinto et al. reported that addition of 5 – 10 wt% of methylmethacrylate – butylacrylate – methylmethacrylate (MAM) in PMMA could increase the solubility of CO_2, leading to the average cell size to 200 – 300 nm as shown in **Figure 16** [44-48]. Diblock copolymer with a fluorinated CO_2-philic block, such as PS-b-PFMA (PFMA, perfluorooctylethyl methacrylate) [49, 50] and PS-b-PFS (PFS, 4-(perfluorooctylpropyloxy) styrene) [50], PS-b-PMMA system [51] showed nano pores as well. However, preparing these block-co-polymer or micro phase separation is complicate and time-consuming. The density and size of foamed cells could be further tuned either by adding nanoparticles or making a composite with other substances that have different CO_2 affinity.

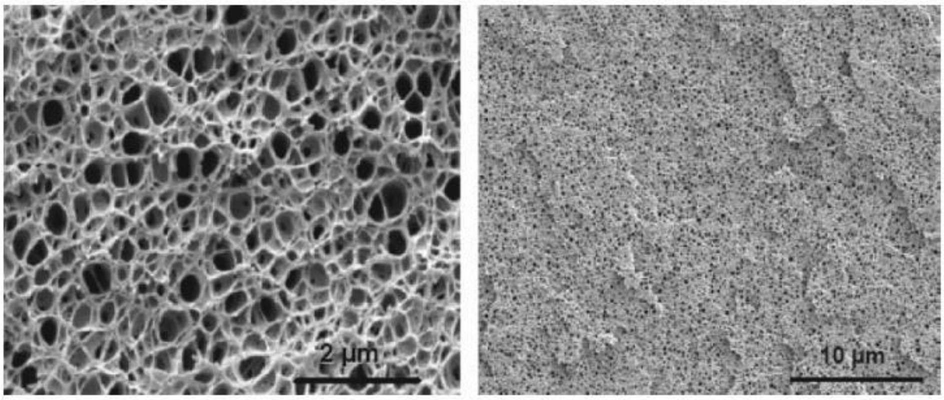

Figure 16. Scanning electron microscopy (SEM) images of PMMA/MAM (90/10) foams saturated at 300 bar, room temperature – foaming was carried out by releasing the pressure inside the reactor at a constant depressurization rate of 15 MPa * min^{-1}.
- Reprinted from [44] with permission.

In summary, physical foaming by supercritical CO_2 is one of well-known ways to manufacture micro or nano foam structures and used for various applications such as light materials, membrane, and thermal insulator. However, high pressure (> 300 bar) is often required to achieve small bubbles, especially for 1S foaming process. In addition, the bubbles obtained from 1S or 2S processes are either microbubbles or interconnected. Another main drawback of this technique is the process time for CO_2 soaking, which takes from several hours to days depending on the temperature and the thickness of the samples. **Figure 17**, for example, shows saturation time required at various temperatures for the PMMA neat polymer of 1.48 mm thickness.

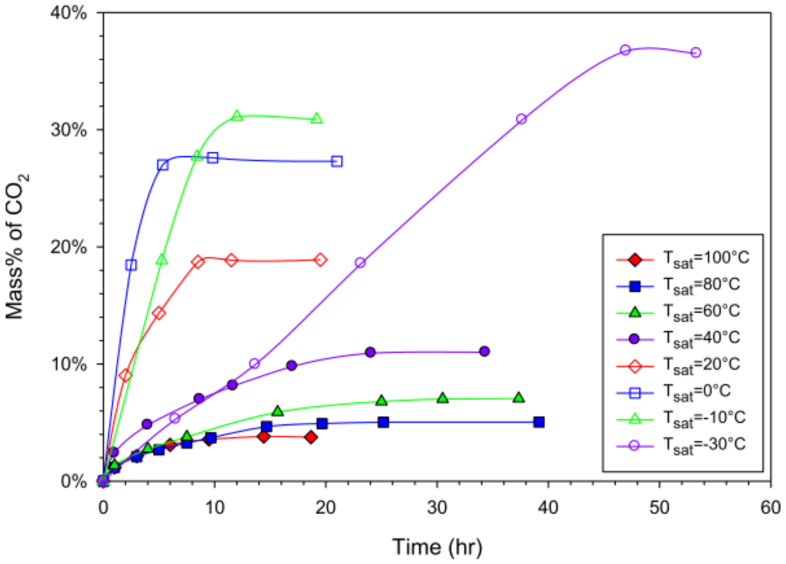

Figure 17. Mass % of CO_2 in PMMA as a function of time at various saturation temperatures. Sample thickness was 1.48 mm. Reprinted from [40]. Copyright (2014), with permission from Elsevier.

Theory for nucleation and growth of pores during foaming process

Classical nucleation theory (CNT) has been used to investigate the nucleation phenomenon in thermoplastic foams triggered by physical blowing agents [38, 39, 52, 53]. The foaming process is assumed as homogeneous nucleation starting from a single phase. The theory describes first order phase separation when the new phase of nucleus occurs and be clearly separated from the initial phase through pressure drop. According to the theory, the free energy of the system is described as the sum of a volume contribution by a new phase, which is proportional to the pressure difference ΔP, and a surface contribution due to the introduction of the interface between a bubble and the surrounding phase. It is described as **Equation 3** [39].

$$\Delta G = -\frac{4}{3}\pi r^3 \Delta P + 4\pi r^2 \gamma$$

Equation 3. Free energy of the system for the nucleation of bubble by classical nucleation theory

where:

$\Delta \mathrm{P}$: pressure difference between gas and matrix, considered as pressure drop

r : radius of bubble

γ : surface tension

Surface energy γ and the degree of supersaturation are dominant factors and bubbles start to form at the critical point where

$$\frac{\mathrm{d}\Delta \mathrm{G}}{\mathrm{dr}} = 0$$

Then, the **Equation 3** becomes

$$-4\pi r^2 \Delta \mathrm{P} + 8\pi \mathrm{r}\gamma = 0$$

Equation 4. equation 4 at the critical point of the nucleation

Therefore, the critical radius for bubble formation is

$$r^{*} = \frac{2\gamma}{\Delta P}$$

Equation 5. the critical radius for bubble formation

the same as described in the formula for Laplace pressure - the pressure difference between the two phases.

By substituting r^{*} into the original equation, the critical Gibb's energy for bubble formation can be written as

$$\Delta G^{*} = \frac{16\,\pi\,\gamma^{3}}{3\,\Delta P^{2}}$$

Equation 6. the critical Gibb's energy for bubble formation

The surface tension is not directly measurable during the foaming process since it keeps changing as the amount of CO_2 sorption in the system is changed by external pressure. However, it is clear that the surface tension becomes lower with increasing amount of CO_2 gas, assuming that the mixture is homogeneous, and the surface tension of the pure supercritical fluid is equal to zero by the empirical equation as

$$\gamma_{mix}^{1/r} = \left(1 - w_{CO_2}\right)\gamma_{pol}^{1/r}$$

Equation 7. the surface tension of mixture with neat polymer and CO_2 gas [39].

where:

γ_{mix} and γ_{pol} : surface tension of mixture and pure polymer

ω_{CO_2}: the weight fraction of CO_2 dissolved in the system

r : estimated value by fitting the equation to experimental data

Since the solubility of the CO_2 increases under higher pressure, the obvious strategy to reduce a free energy barrier is to increase the ΔP and depressurize fast.

In addition, the critical Gibb's energy has a great effect on nucleation rate, N which is described as Arrhenius-equation as below [54]:

$$N = J \exp\left(\frac{-\Delta G^*}{kT} \right)$$

Equation 8. Arrhenius equation of the nucleation rate

where :

J: kinetically determined constant (collision factor)
k: Boltzmann constant
T: temperature (kelvin)

In conclusion, low surface tension, high saturation pressure, and high temperature favor the critical Gibb's energy for the nucleation of bubble. Furthermore, the amount of absorbed CO_2 has an effect not only on the supersaturation of the matrix but also on the surface tension and the T_g temperature of the system. Therefore, the effect of the supersaturation and the surface tension of matrix need to be taken into consideration separately in order to achieve as small bubbles as possible.

Although, the theory gives reasonable speculations and makes it possible to predict the change in the structure of foams, there is inconsistency between theoretical models and experimental results as well. Shirvan, M. M. M., et al pointed out the inconsistency in their review paper about nucleation theories in thermoplastic foams and wrote 'scientists have declared two main reasons for the inconsistency; error in the calculation of variables and simplifying assumptions for the establishment of the relations between variables. The variables include interfacial tension between polymer and solvent, difference between the inside and outside pressure of the nucleolus' [52]. They added that the absence of the effect of time, pressure drop rate and supersaturation content also should be taken into account. This problem would be explained in our system as well in the following discussion.

2.3 Other ways of producing porous materials (templating system)

Chemical and physical blowing processes are the ways of generating pores in the matrix directly from gas. There are also other ways of producing porous materials through so-called templating system. It means the polymerization of a mixture, which contains polymeric precursor and templates (e.g. porogen), followed by removing the templates, leaving pores behind [26, 55, 56]. For example, simply adding water soluble particles (e.g. NaCl) or volatile solvent (e.g. ethanol) to the mixture belongs to this category.

I summarized in this chapter three well-known templating methods to introduce porosity, i.e. self-assembly of block-co-polymer, high internal phase emulsion (HIPE), and aerogel, and compared their processes and structural features of the materials.

First, self-assembly of block copolymer is a well-defined way to fabricate ordered nano structure materials. The unique structures are attributed to the thermodynamic immiscibility of different substances [57-60]. Depending on the composition of each block, the morphology of copolymer changes to spheres, cylinders, gyroid, and lamellae as shown in **Figure 18**.

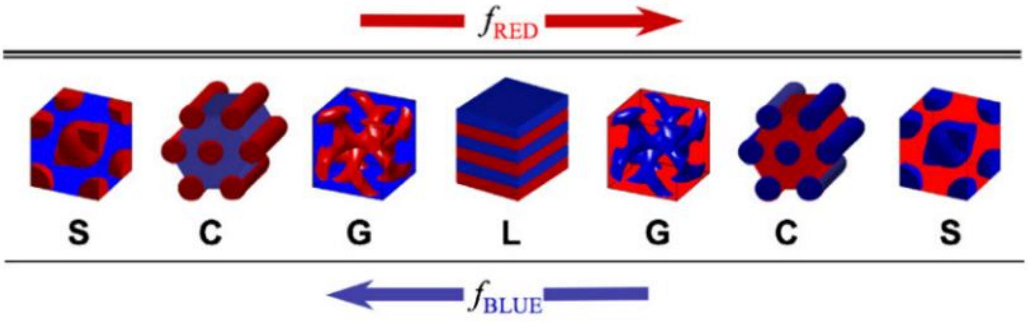

Figure 18. Diblock copolymer morphologies accepted to represent the equilibrium ordered states. Morphologies are shown in increasing red-block (decreasing blue) composition of a red - blue diblock copolymer. (S) BCC spheres, (C) hexagonally packed cylinders, (G) gyroid, (L) lamellae. – Reprinted from [60]. Copyright (2008), with permission from Elsevier.

Although the templating by BCP seems a perfect way to produce nano pattern with well controlled size and shape, it usually includes long process time for each process such as self-assembly, precipitation, drying, and annealing. Furthermore, extracting sacrificial components by heating or specific chemicals is essential [57, 58].

Second, a technique called high internal phase emulsion polymerization (HIPE) has a volume percentage of internal phase more than 74 % (v/v), meaning less than 26 % of external scaffold phase remains after subsequent removal of the internal phase as shown in **Scheme 4** [61]. There are different types of emulsions depending on their systems such as oil-in-water (O/W) [62], water-in-oil (W/O) [63], and CO_2-in-water emulsion (CW) [64, 65]. **Figure 19** shows the typical structure of HIPE materials. They have two types of pores, big voids and small windows which are determined by the components and stability of the emulsions. The size of voids is usually in the range of tens of micron and interconnected by small windows. Therefore, the materials fabricated by this method could be a good candidate for membrane or thermal insulating materials. However, more than 74 % of unwanted internal phase, which is mainly used for template and should be removed afterwards, is the main drawback of this process. In addition, the interconnected microbubbles are not desirable for optical applications due to the low scratch resistance and hardness as well as scattering by microbubbles.

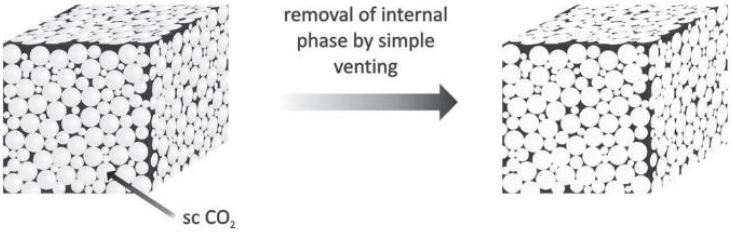

Scheme 4. PolyHIPE prepared by supercritical CO_2 as internal phase.

- Reprinted from [61] with permission

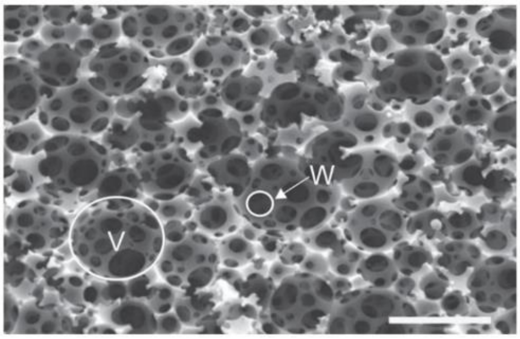

Figure 19. SEM of a typical PolyHIPE material. V indicates void, W indicates window - scale bar = 20 µm - Reproduced from [66] with permission.

Finally, alkoxysilane based silica aerogels are recently attracting attention as transparent thermal insulators or shock absorbing materials due to their transparency and flexibility. The physical properties of the silica-based aerogels could be changed depending on the precursors and process factors such as pH of the solution, aging conditions, addition of surfactant, and drying methods [67]. However, silica aerogels prepared by tetra alkoxysilane (e.g. Tetraethoxysilane, TEOS) [68] are usually transparent but very brittle, while aerogels prepared by tri alkoxysilane (e.g. Methyltrimethoxysilane, MTMS) have better physical properties but they are opaque [69]. Taiyo Shimizu et al. reported a transparent and flexible aerogel by using bridging alkoxysilane such as polyethylsilsesquioxane (PESQ) and polyvinylsilsesquioxane (PVSQ) (**Figure 20**) [70]. Transparency and physical properties were determined by the size and density of the pores as shown in **Figure 21**. However, the high cost of these complex bridging precursors is one of drawback for this PESQ and PVSQ system. Moreover, the aerogel process takes usually 2 - 5 days for condensation or aging, and drying should be done in an autoclave under supercritical alcohol drying (SAD) or supercritical CO_2 drying (SCD) conditions [68-70]. Therefore, more studies are needed to focus on using low cost silanes aerogel or reducing process time.

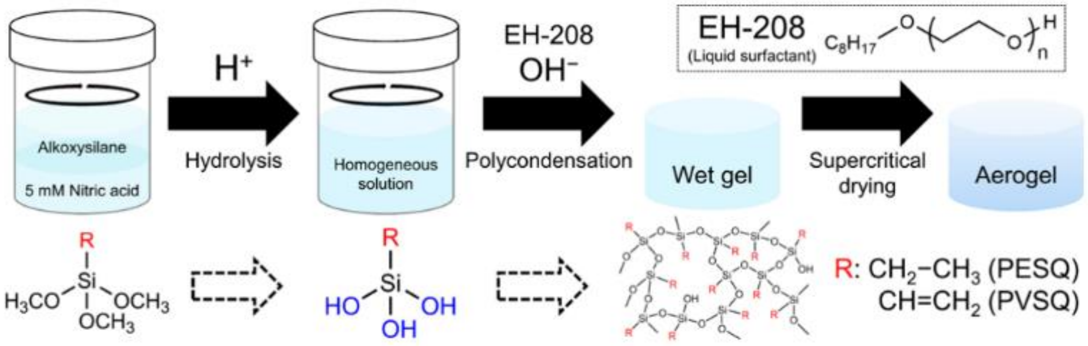

Figure 20. Schematic of the synthetic procedure of polyethylsilsesquioxane (PESQ) and polyvinylsilsesquioxane (PVSQ) aerogels.
– Reprinted with permission from [70]. Copyright (2016) American Chemical Society.

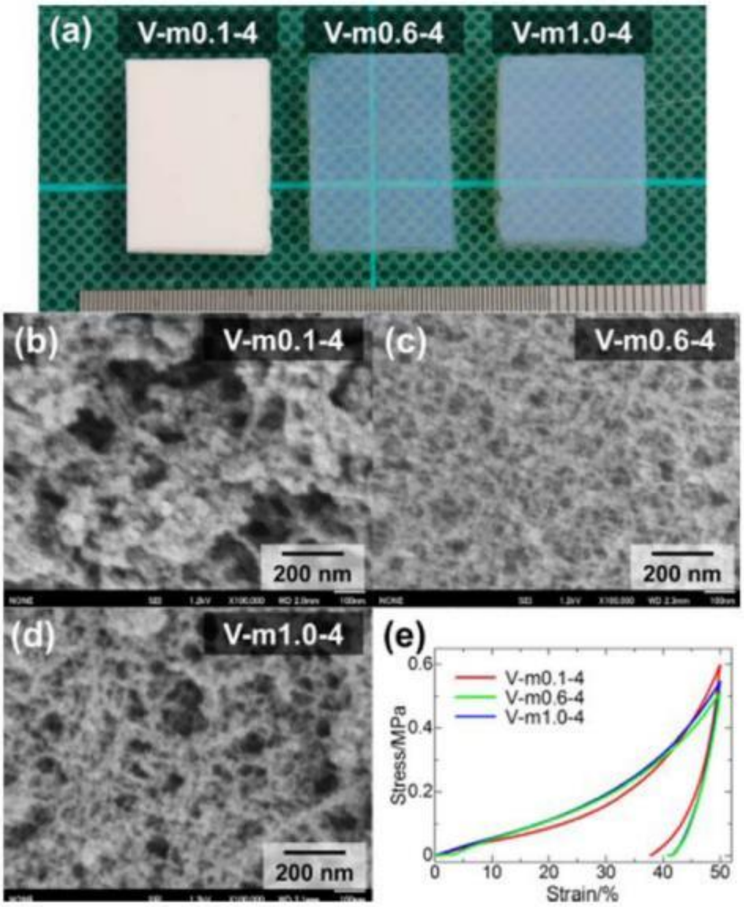

Figure 21. Appearance of PVSQ aerogels, (b-d) FE-SEM images, and (e) Stress-strain curves on uniaxial compression-decompression of PVSQ aerogels, V-m0.1-4, V-m0.6-4, and V-m1.0-4.
m-0.1-4, m0.6-4, and m1.0-4 mean the concentration of base catalyst, tetramethylammonium hydroxide, TMAOH with gelation temperature of 4 °C
- Reprinted with permission from [70] . Copyright (2016) American Chemical Society.

In summary, all templating methods introduced in this chapter have better potential when it comes to controlling the size and structure of pores compared to non-templating chemical and physical blowing agent systems. However, long process time for the templating process (e.g. self-assembly or aging) or necessity for the post process (e.g. extraction, etching, and drying) are the main disadvantages of these processes. As a result, the manufacturing time and costs are much higher than those of chemical or physical foaming.

3. Materials and methods

Materials

2-HEMA (2-Hydroxyethylmethacrylate, 98%), EGDMA (Ethyleneglycol dimethacrylate, 98%), and AIBN (2, 2′-Azobis (2-methylpropionitrile), 98%) were purchased from Sigma Aldrich. UV initiator IRGACURE 819 was purchased from Ciba Specialty Chemicals Inc.
V-65 (2, 2'-Azobis(2,4-Dimethylvaleronitrile) and V-70 (2,2'-Azobis(4-Methoxy-2,4-Dimethylvaleronitrile)) were purchased from FUJIFILM Wako Chemicals, Europe GmbH.
Surfactants of BYK333 and BYK378 were purchased from BYK (BYK Additives and Instruments, Germany). Red dyeing chemical of MACROLEX was purchased from LANXESS. All materials were used without any further purification.
200 µm PVC film (Neschen, Germany) was used to control the thickness of the films.
Two different UV lamps (M405LP1-C5, THORLABS and Thermo Oriel (1000W)) were used to initiate polymerization and post-bubble forming process.

Anti-stick silanization treatment

A microscope slide was first treated with air plasma for 5 min and transferred to a desiccator. 50 µl of tridecafluoro-1,1,2,2- tetrahydrooctyl trichlorosilane (97%, AB111444) was placed in the middle of the desiccator. The desiccator was closed and connected to a pump to reach the inside pressure of 5 mbar. Evaporation of the solution and chemical deposition maintained for 5 min and the pressure was slowly released. This coating, so-called anti-stick silanization, was used to make it easy to remove polymer films when they were cured in between two glasses.

Acrylate silanization coating

A microscope slide was treated with air plasma as descrived above. The surface of the plasma treated microscope was coverd by the solution of 3 - (Trimethoxysilyl) propyl methacrylate (Sigma Aldrich, Germany) and put in a dark box for 3 h so that chemical silanization could occur. The solution was washed away with ethanol and dried in air. This coating, so-called silanization coating was used to increase the adhesion property between glass substrate and acrylate.

Characterization of samples

Optical microscope (Nikon – ECLIPSE LV100ND), and scanning electron microscope (SEM, FEI - Quanta 400F) were used to characterize the bubbles. For SEM measurement, the surface was gold sputtered under 20 mA for 60 sec (JEOL JFC-1300, auto fine coater). Refractive index of films was measured by Ellipsometry (EC-400, J.A. Woollam Co. Inc.) The size of bubbles in the images of OM and SEM was analyzed by ImageJ program.

3.1 Azo-chemical initiator (AIBN) as a blowing agent

One step continuous foaming

A mixture of 2-hydroxyethylmethacrylate (HEMA) monomer and different amounts of 2, 2′-Azobis (2-methylpropionitrile), AIBN, was stirred at room temperature for 1 h. **Table 4**. shows the amount of AIBN in 10 g of HEMA monomer. 2 ml of each solution were put into different glass bottles and thermally cured in the oven at 60 °C in air for 5 h.

	1	**2**	**3**	**4**	**5**	**6**
AIBN (g)	0.01	0.02	0.04	0.08	0.16	0.32

Table 4. Different amounts of AIBN in 10 g of HEMA solution
(0.32 g of AIBN is the maximum solubility in HEMA monomer)

Two step foaming

0.2 % Irgacure 819 was added to the solution 6 in **Table 4** as a photo initiator. The mixture was sandwiched between two microscope slides - one of them had been anti-stick silanization treated - by using 200 µm masking tape as s spacer and then irradiated by UV lamp (405 nm of wavelength) for 5 min. After the UV radiation, the anti-stick microscope slide was removed. The UV pre-cured PHEMA was used for other experiments unless otherwise stated. The film was transferred to a hot plate at 120 °C for 1 h and cooled down to the room temperature. Another film without AIBN, which contains only the monomer and Irgacure, was prepared as a reference. The foamed samples were characterized for the size and distribution of the bubbles by using SEM.

3.2 Factors that affect the nucleation and growth of bubbles

3.2.1. Effect of the temperature

The UV pre-cured PHEMA films, prepared as described in the preceding section, were post-heated on the hot plate at 100 °C, 110 °C, and 120 °C for 3.5 min, 1 min, and 30 sec, respectively. The different foaming conditions at given temperatures were experimentally determined when the samples turned opaque (white). The samples on the hot plate were placed under the optical microscope in order to in-situ measure the foaming process. The nucleation and growth of the bubbles were evaluated by recording the in-situ figures every second under the microscope. The samples were then removed from the hot plate and cooled down to the room temperature. The foamed samples were characterized for the size and distribution of the bubbles by using SEM.

3.2.2 Effect of gas saturation of the matrix – nitrogen soaking

The UV-cured PHEMA was transferred to an autoclave and nitrogen saturated under the pressure of 150 bar at room temperature for 24 h. After releasing the pressure, the film was transferred to the hot plate at 110 °C and heated for 30 sec until the sample turned opaque. Another PHEMA film without AIBN, which contains only HEMA and Irgacure 819, was tested as a reference under the same conditions. The samples on the hot plates were placed under the optical microscope and nucleation and growth of bubbles were in-situ measured as described in the previous chapter. The foamed samples were characterized by using SEM.

3.2.3 Effect of the external pressure and surface constraining layer

The foaming of the UV pre-cured PHEMA films was tested in the autoclave under different nitrogen pressures of 50, 100, and 150 bar. The temperature of the vessel in the autoclave was increased to 120 °C in 5 min (25 °C/min) and maintained for 10 min. After the samples were slowly cooled down to the room temperature in the autoclave, the pressure was released. The film foamed in the autoclave under ambient pressure was used as control. For control, the surface of the films was open to the nitrogen gas in the autoclave.

Another UV-cured film was sandwiched between two microscope slides and fixed together by two clamps, while the film was being foamed in the autoclave under ambient pressure.

The samples were characterized for the size and distribution of the bubbles by using OM and SEM.

3.2.4 Laser heating as a post-heating process

A slightly red colored UV pre-cured PHEMA film was prepared by adding a red dyeing chemical, MACROLEX, to the mixture of HEMA (10 g), AIBN (0.32 g), and Irgacure 819 (0.02 g). Other preparing conditions including UV irradiation were the same as before. A green laser with wavelength of 532 nm was used for the foaming by heating the PHEMA film. **Scheme 5** shows the set up for the laser scribing experiment.

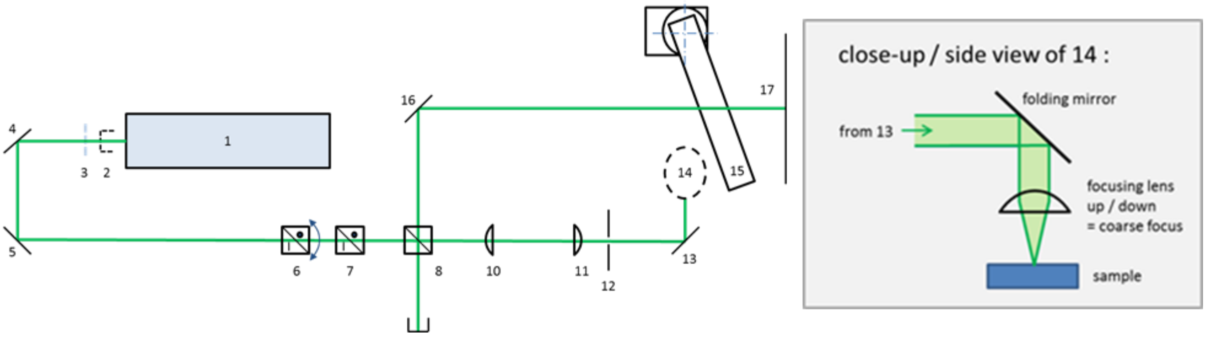

Scheme 5. Thermal laser scribing test set-up

1. Laser head (Millennia Edge)
2. Beam dump (removable)
3. Attenuating filter (optional, for eye-safe alignment)
4,5. Alignment mirrors
6. Crystal polarizer with rotary adjustment (power adjustment)
7. Crystal polarizer, fixed
8. Beam splitter (50 %, non-polarizing)
9. Calorimetric power meter (sample power = 0.709 · display)
10. Lens f = 40 mm
11. Lens f = 100 mm (slide along optical axis for fine focusing)
12. Iris aperture (alignment target)
13. Folding mirror
14. Vertical folding mirror above focusing lens (f=25 mm aspherical)
15. Sample carrier on motorized moving arm
16. Folding mirror for retroreflected beam
17. Monitor screen for retroreflected beam (focusing aid)

Laser heating the film with the film surface open to air

The film was heated by the green laser (532 nm) with 300 mW, while the moving arm (15, from **Scheme 5**) moved under the laser with the speed of 8, 16, and 32 mm/sec (32 mm/sec is the maximum speed of the motorized moving arm). The surface of the film was open to air while being heated. The intensity of the laser and the speed of the moving arm were experimentally determined to achieve the conditions that bubbles were detected on the film by OM and SEM.

Laser heating the film with the surface confinement

A PDMS film was used as a surface constraining layer as shown in **Scheme 6**. The metal frame was then compressed under the load of 250 N (250 N / 0.5 cm^2 corresponding to 50 bar) and firmly fixed. The experiment was optimized to the power of the green laser with 160 mW and the speed of the moving arm with 32 mm / sec. Besides, an optical chopper was mounted in the set-up so that the film could be heated within a specific period of time (0.25 ms) instead of continuously being heated. The foamed samples were characterized for the size and distribution of the bubbles using SEM.

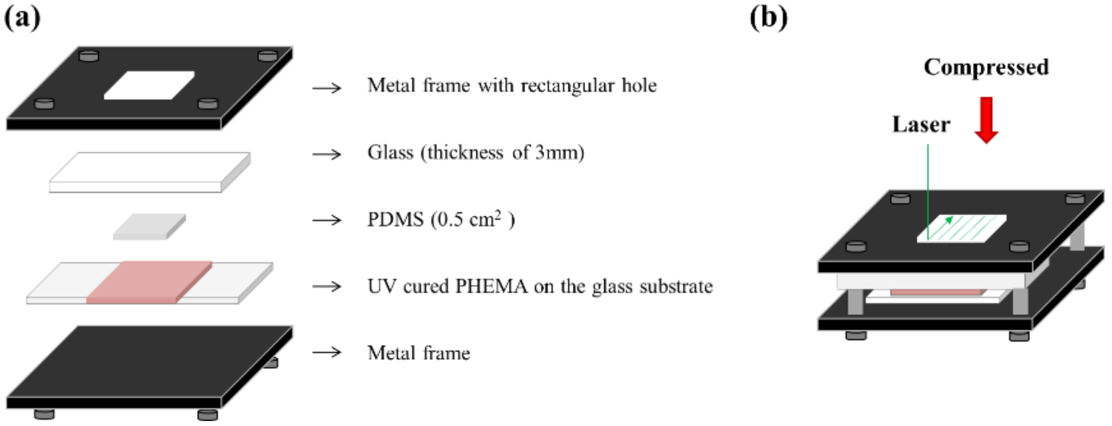

Scheme 6. Laser scribing process (a) components before assembly (b) laser scribing process

3.2.5 Effect of surface tension (surfactants)

Effect of surfactants on the nucleation of bubbles in pre-cured PHEMA films

Various surfactants were added into the mixture of HEMA (10 g), AIBN (0.32 g), and Irgacure 819 (0.02 g). **Table 5** shows the name and concentration of the surfactants used for the experiments. Films were UV pre-cured as before and then foamed on the hot plate at 110 °C for 45 sec and 1 min, respectively. Another film without any surfactant was used as control. The samples foamed under ten different compositions were characterized by using SEM.

Reference sample (1): without surfactant

Surfactants Amount (wt %)	BYK333	BYK378	1H, 1H, 5H-Octafluoropentyl acrylate
0.1	(2)	(5)	(8)
0.2	(3)	(6)	(9)
0.4	(4)	(7)	(10)

Table 5. Various surfactants and their amount added into the basic mixture of HEMA, AIBN, and Irgacure 819

3.2.6 Kinetics of nitrogen generation (ABVN)

Another azo initiator, ABVN, was tested as an alternative for blowing agent instead of AIBN. A mixture of HEMA (10 g), Irgacure 819 (0.03 g), surfactant - BYK 378 (0.4 wt%), and ABVN (0.65 g) was sandwiched between two microscope slides and UV-cured as described before. The UV pre-cured PHEMA films were transferred to the hot plate at 110 °C and foamed for 10 and 30 sec, respectively. **Table 6** shows the summary of the optimized experimental conditions based on the previous experiments. The foamed samples under different foaming time were characterized by using SEM and optical properties of transmittance and haze were measured.

Monomer system	HEMA
Photo initiator	Irgacure 819
Blowing agent	ABVN (instead of AIBN)
Surfactant	BYK 378 (0.4 wt%)
Film condition	Pre-cured PHEMA
Foaming condition	Heating at 110 °C 10 sec 30 sec

Table 6. Summary of the experimental conditions (pre-cured PHEMA) for the optimization of factors

3.2.7 Decomposition of ABVN by thermal heating and UV radiation

Starting from liquid state sol

The same mixture including ABVN (3.2.6) was sandwiched between two microscope slides and directly moved to the hot plate at 70 °C for 5 min without UV radiation. For another sample, UV radiation (1000 W UV lamp) was combined during the thermal heating. The two samples were polymerized and foamed simultaneously starting from liquid state sol.

The foamed samples were characterized by using SEM.

Starting from partially cured PHEMA

The same mixture was sandwiched between two microscope slides and partially cured under the UV-lamp (405 nm) for 2 min. The partially cured sol was then transferred to the hot plate at 70 °C and UV radiated (1000 W) together for additional 2 min. **Table 7** shows the summary of the experimental conditions.

The foamed samples were characterized by using SEM. Optical properties of transmittance, haze, and refractive index were measured.

Monomer system	HEMA
Photo initiator	Irgacure 819
Blowing agent	ABVN (instead of AIBN)
Surfactant	BYK 378 (0.4 wt%)
Film condition	Partially cured PHEMA (405 nm UV for 2 min)
Foaming condition	Protective glass on the surface
	Heating at 70 °C
	High power UV (1000 W)
	2 min

Table 7. Summary of the experimental conditions (partially cured PHEMA) for the optimization of factors

4. Results

4.1 Azo-chemical initiator (AIBN) as a blowing agent

One step continuous foaming

Figure 22 shows that the higher the amount of AIBN in solutions is, the more bubbles are generated during the polymerization process, making polymers opaque due to the scattering of light. Furthermore, the apparent volume of the polymers became doubled (sample 4), tripled (sample 5), and even more than that (sample 6) compared to the polymer with the smallest amount of AIBN (sample 1).

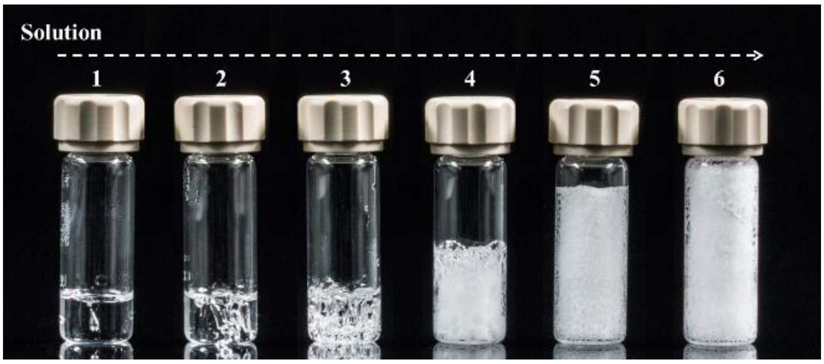

Figure 22 . Thermally cured HEMA samples with different amounts of AIBN
From left - 0.01, 0.02, 0.04, 0.08, 0.16, 0.32 g of AIBN in 10 g of 2-HEMA (2 ml of each solution) cured in the oven at 60 °C in air for 5 h.

Two steps foaming process

In contrast to the thermally cured samples without the UV-initiator Irgacure 819, the UV-cured film remained transparent, although the mixture contained the maximum concentration of AIBN. (see the sample from solution 6 in **Figure 22**). The film with AIBN became opaque (white) after foaming, while the reference film without AIBN remained clear as shown in **Figure 23**.

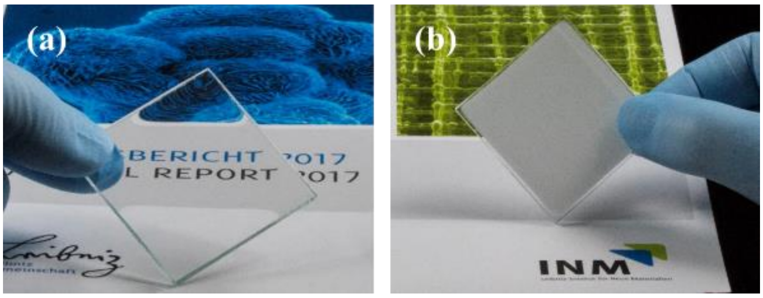

Figure 23. PHEMA films after post-heating at 120 °C for 1 h. (a) without AIBN (b) with AIBN

The thickness of the film also increased from the initial thickness of 200 µm up to 340 µm (1.7 times thicker) after foaming. In addition, the size distribution of bubbles ranged from below 10 µm to 59 µm. Along the long axis of the ellipsoidal shape of the bubbles, they were stretched in vertical direction as shown in **Figure 24 (a)** and **(b).** It is worth noting that there is a dense, non-foamed skin area near the surface, which has a thickness of around 25 – 40 µm (**Figure 24 (c)**).

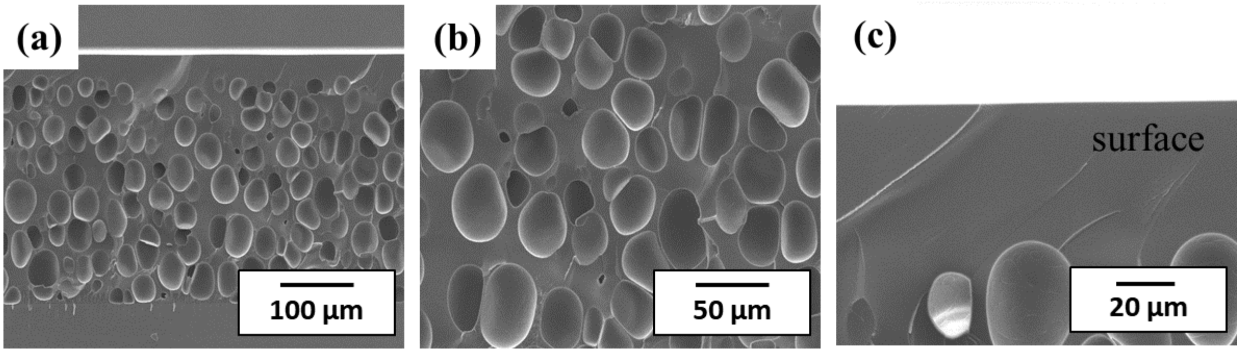

Figure 24. SEM cross section images of foamed PHEMA at 120 °C for 1h from Figure 23 (b).
(a), (b); overview, (c); near the surface area

4.2 Factors that affect the nucleation and growth of bubbles

4.2.1. Effect of the foaming temperature

In-situ OM images taken at different temperature and time are shown in **Figure 25**. The post heating temperature has a significant effect on the nucleation and growth kinetics. In case of the sample heated at 120 °C, it took only 10 sec from the initial nucleation to until it turns opaque, while it took 3 min for the sample heated at 100 °C. Nucleation density also increased by increasing the temperature. In addition, once nuclei are formed in the earlier stage of nucleation, ripening of the already existing bubbles and other nucleation was observed simultaneously.

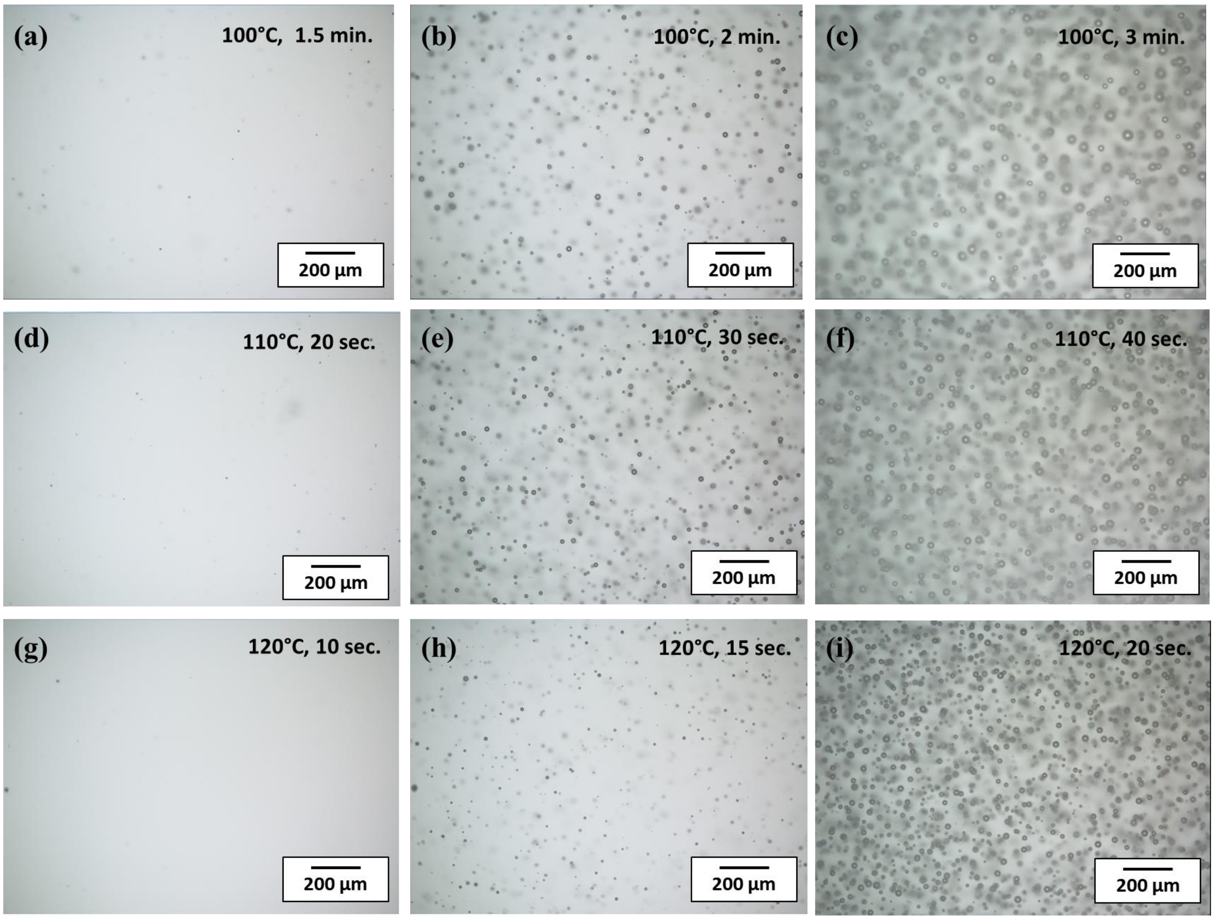

Figure 25. In-situ OM images of UV-cured PHEMA during post-heating at (a), (b), (c); 100 °C at 1.5 min., 2 min., 3 min. (d), (e), (f); 110 °C at 20 sec, 30 sec, 40 sec, (g), (h), (i); 120 °C at 10 sec, 20 sec, 30 sec

Figure 26 shows the cross-section images of the samples after they turned white. As it was pointed out, the sample heated at 120 °C has higher nucleation density and the size of bubbles increased as well. Furthermore, in contrast to the bubbles foamed at 120 °C for 1 h with ellipsoidal shape in the previous chapter (**Figure 24**), the shape of bubbles at early stage of nucleation and growth was still spherical.

The dense skin area was decreased from 60 – 100 µm (100 °C) to 50 – 60 µm (110 °C) and 30 – 50 µm (120 °C) with increasing temperature. However, it was still impossible to generate bubbles when the thickness of the film was below these critical thicknesses (60, 50, and 30 µm) for each temperature (at 100, 110, and 120 °C).

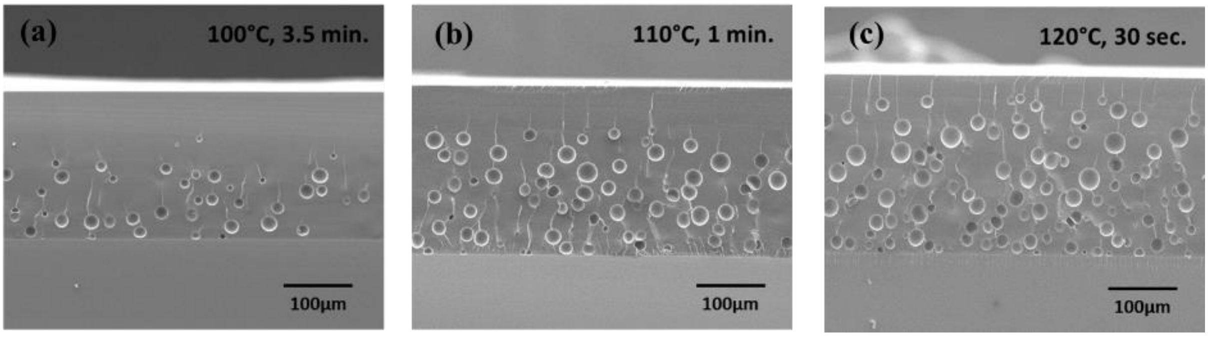

Figure 26. SEM images of foamed PHMEA films after heating
(a) 100 °C for 3.5 min, (b), 110 °C for 1 min., (c) 120 °C for 25 sec

4.2.2 Effect of gas saturation of the matrix – nitrogen soaking

Figure 27 shows the in-situ OM images of the nucleation and growth of bubbles from the sample N_2 soaked before being heated. The nucleation was observed within 5 sec and the sample completely turned opaque within 30 sec.

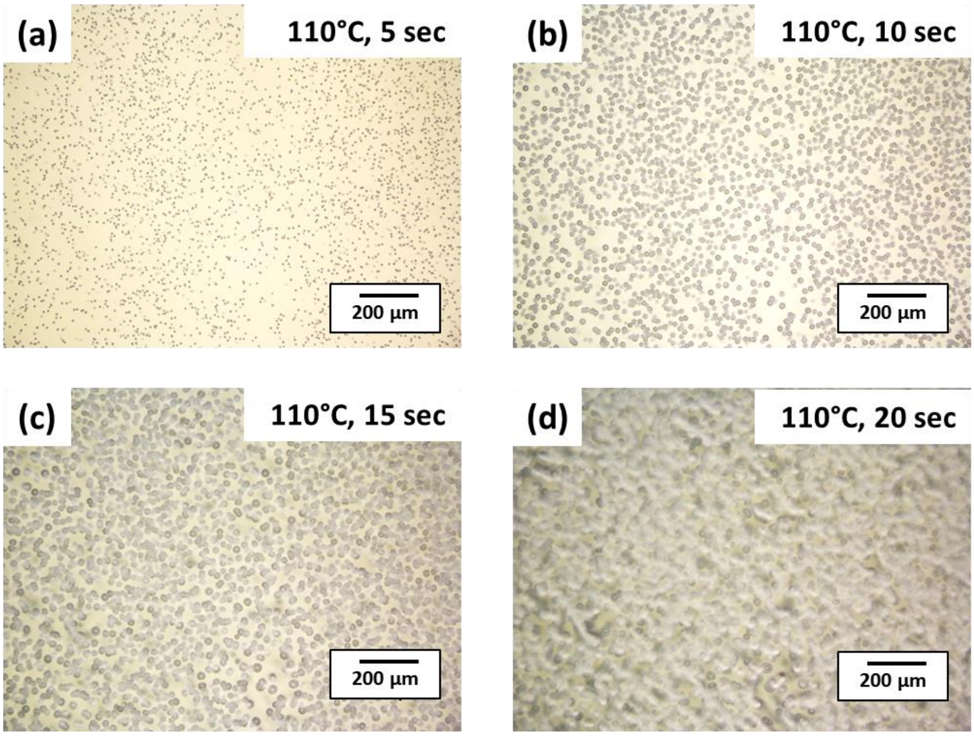

Figure 27. OM images of N_2 soaked (150 bar at room temperature for 24 h) PHEMA with AIBN after heating at 110 °C for (a) 5 sec (b) 10 sec (c) 15 sec (d) 20 sec

Two different types of nucleation and growth of bubbles were observed during the foaming as shown in **Figure 28**. The one near the surface led to smaller bubbles below 25 µm of diameter with higher distribution density, the other one near the bottom resulted in bigger bubbles above 50 µm with lower density. In addition, the thickness of the dense skin area was decreased to 10 – 20 µm.

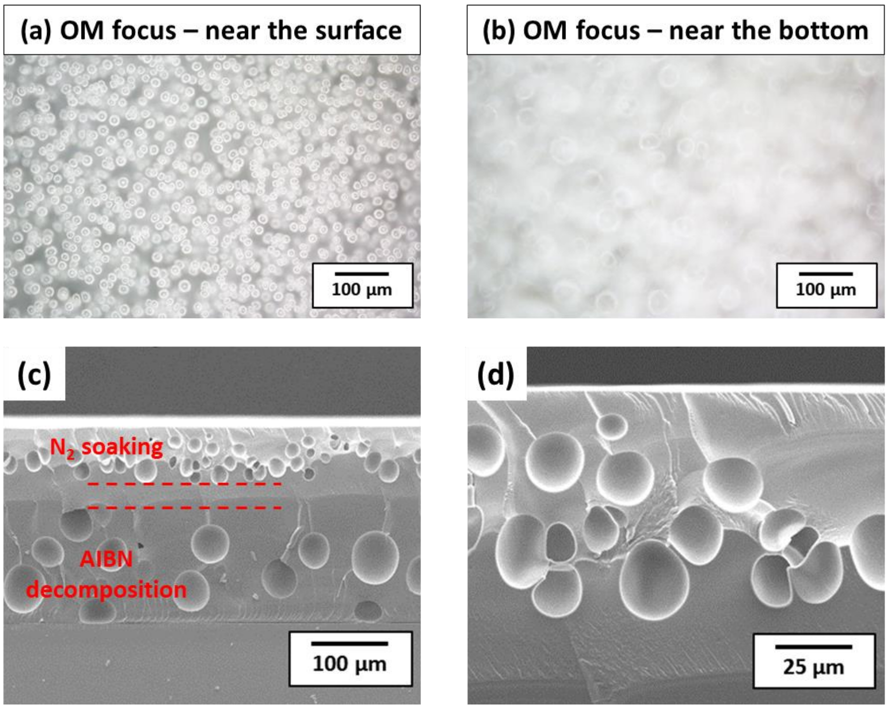

Figure 28. N_2 soaked (150 bar, 24 h) PHEMA with AIBN after post heating process at 110 °C for 30 sec
(a) OM image focused near the surface (b) focused near the bottom
(c) SEM cross section image (d) high magnification of the (c) near the surface

However, the reference sample soaked under the same condition without AIBN, showed much less nucleation and slower growth of bubbles as shown in **Figure 29**.

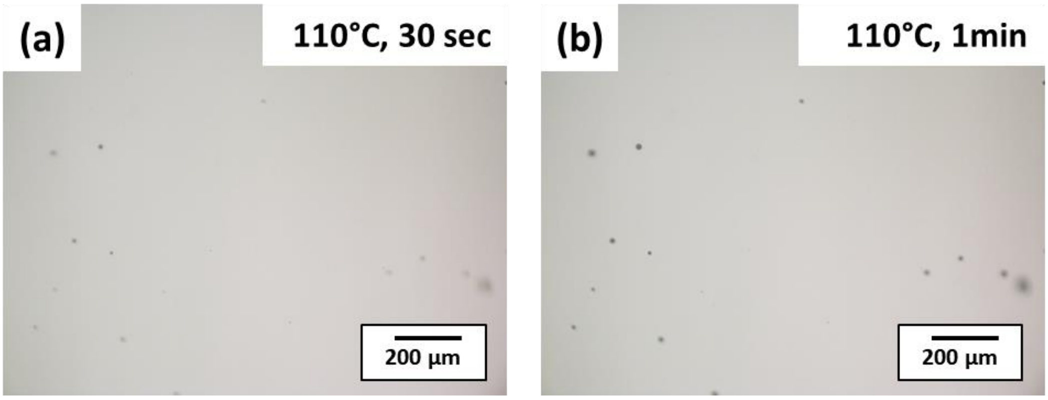

Figure 29. OM images of N_2 soaked (150 bar, 24 h) PHEMA w/o AIBN after post heating process at 110 °C for
(a) 30 sec (b) 1 min

4.2.3 Effect of the external pressure and surface constraining layer

Figure 30 shows the effect of the foaming pressure in the autoclave on the size and distribution of the bubbles. The thickness of the films foamed under ambient pressure increased up to 385 µm (1.9 times), whiles the others foamed under pressure kept their initial thickness of 200 µm (213, 211, and 203 µm under 150, 100, and 50 bar, respectively). Besides, the shape of bubbles changed from random ellipsoidal shape to spherical when the bubbles were foamed under pressure.

The average size of bubbles decreased from 30 - 70 µm (ambient) to 10 - 25 µm (50 bar), 5 - 15 µm (100 bar), and 5 – 10 µm (150 bar) with narrow standard deviation as shown in **Figure 31**, but with lower density. The dense un-foamed surface skin still remained in all the samples as well.

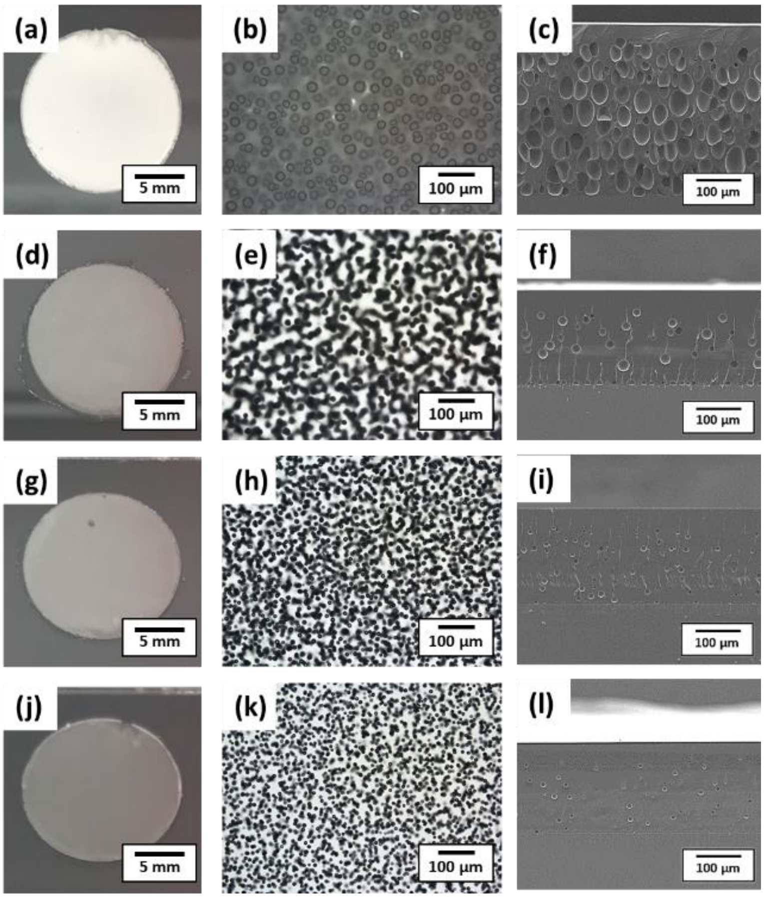

Figure 30. Photos, OM and SEM images of PHMEA heated in autoclave at 120 °C for 10 min. (a),(b),(c); at ambient pressure, (d),(e),(f); 50 bar, (g),(h),(i); 100 bar, and (j),(k),(l); 150 bar

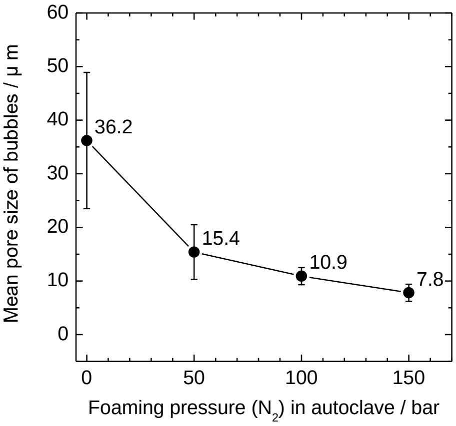

Figure 31. Mean bubble size of bubbles foamed in autoclave at 120 °C for 10 min under different external pressure (N_2) of ambient, 50, 100, and 150 bar, respectively.

Figure 32 shows the effect of the surface constraining layer, both on the nucleation of bubbles and on the thickness of the dense skin area, particularly. Compared to the foamed sample at ambient pressure with open surface (**Figure 32 (a)** and **(b)**), the sample sandwiched and clamped during the foaming (**Figure 32 (c)** and **(d)**) has more nucleation. In addition, the mean diameter of bubbles also decreased from 38 µm to 20 µm, and the dense un-foamed layer became thinner from around 35 µm to 18 µm. The closest distance between a bubble and the surface was 8 µm.

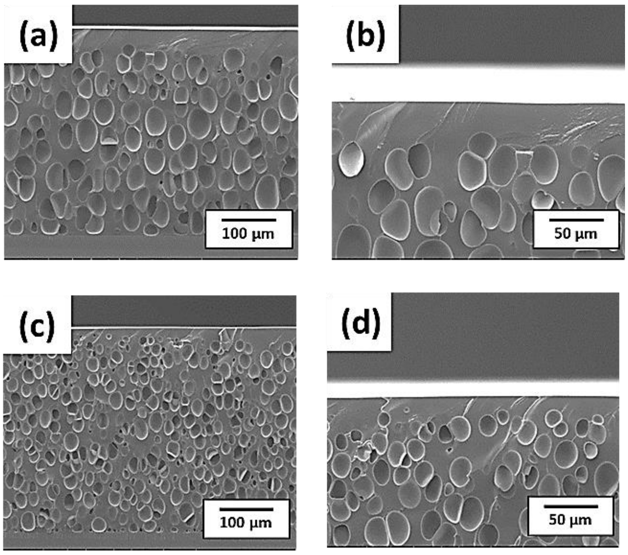

Figure 32. SEM images of bubbles foamed in autoclave (a); open surface to the air (b); near the surface of (a), (c); sandwiched between two glasses, (d); near the surface of (c)

4.2.4 Laser heating as a post heating process

Laser heating the film with the surface open to air

The OM and SEM images in **Figure 33** showed the change in the width of the heat affected area, which increased from 50 µm to 300 µm depending on the speed of the moving arm. The slower the moving arm moves, the more bubbles with surface bulging were observed. In addition, the bubbles were mainly formed in the middle of the heated area. No bubble was detected in **Figure 33** (d), although it showed the surface bulging. For the sample heated the slowest (8 mm/sec), the mean diameter of pores from near the surface to bottom area was decreased from 14 µm to 9 µm. The thickness of the dense un-foamed layer was 12 – 13 µm. There were a few bubbles detected in the film heated with the intermediate speed of the moving arm, 16 mm / sec.

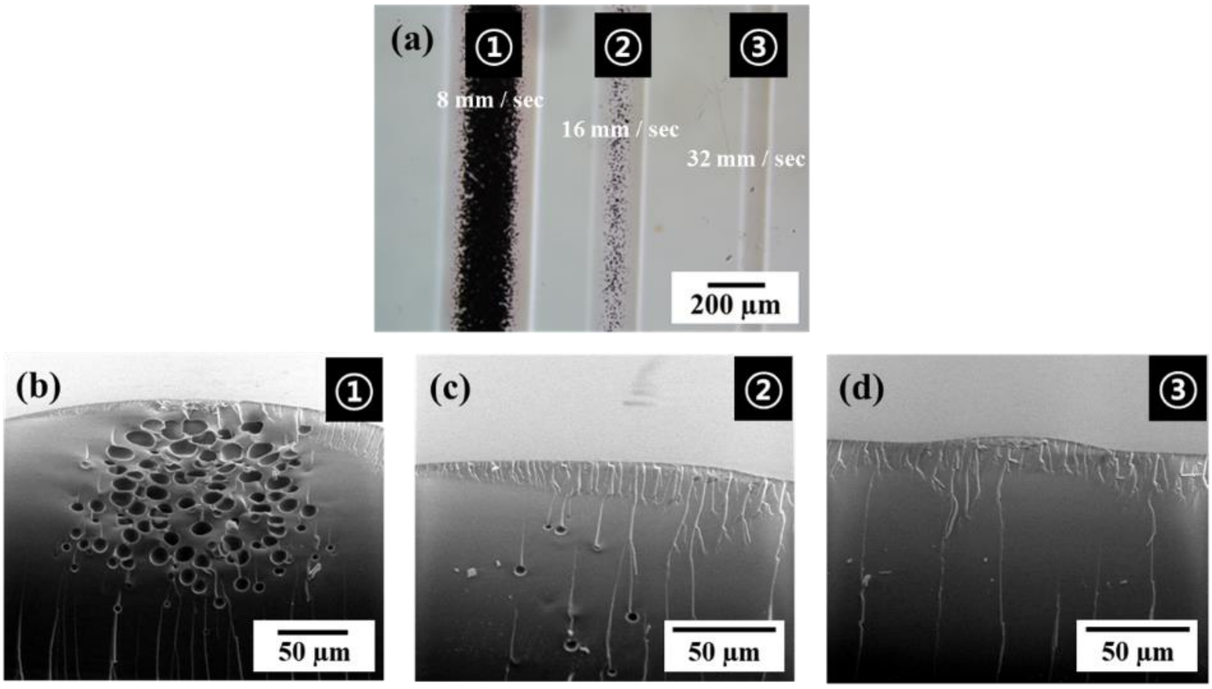

Figure 33. (a) OM image of laser (300 mW) heated line with different speeds of the moving arm (8, 16, 32 mm / sec). (b), (c), (d) corresponding SEM cross section images.

Laser heating the film with the surface confinement

Figure 34 shows the bubbles foamed under the laser pulse and a surface constraining layer of PDMS. One single spot in **Figure 34** (a) represents the area heated for 0.25 ms each. In contrast to the **Figure 33**, samples without surface blocking layer, the surface remained smooth (b). Besides, the mean pore size of the bubbles was significantly decreased to sub-micron level, which is 470 nm, i.e. nanobubbles. In addition, the thickness of the un-foamed dense layer became below 500 nm.

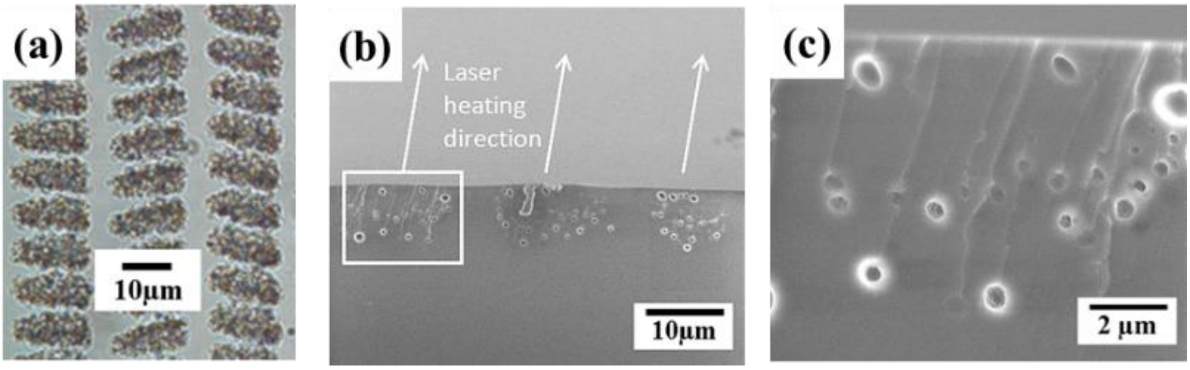

Figure 34. (a) OM and (b) SEM cross section images of laser heated area with surface constrained by a layer of PDMS (c) high magnification of the white rectangular in (b)
160 mW pulse laser (0.25 ms), the speed of moving arm : 32 mm/sec

4.2.5 Effect of surface tension (surfactants)

Figure 35 and **Figure 36** show the effect of the two different commercial surfactants and 1H, 1H, 5H-Octafluoropentyl acrylate on the nucleation of the bubbles. Compared to the PHEMA without surfactant, the samples with BYK 333 and BYK 378 showed more nucleation of the micro size bubbles. The samples with 1H, 1H, 5H-Octafluoropentyl acrylate, on the other hand, had fewer nucleation, leading to bigger microbubbles than those of without surfactant. Apparently, there is no significant effect of the amount of BYK on the nucleation of the bubbles when it comes to micro size bubbles. However, nano size bubbles were detected in the sample with 0.4 wt% of BYK 378 as shown in **Figure 37**. Furthermore, such nanobubbles were detected not only in between microbubbles but also through the entire film from bottom to the surface. The size of the bubbles was in the range of 70 – 90 nm.

When the foaming was stopped before the sample turned white (110 °C for 45 sec), only nano size bubbles were detected without microbubble as shown in **Figure 38**. The size distribution of the bubbles was homogeneous and the mean pore size of bubbles was 60 nm.

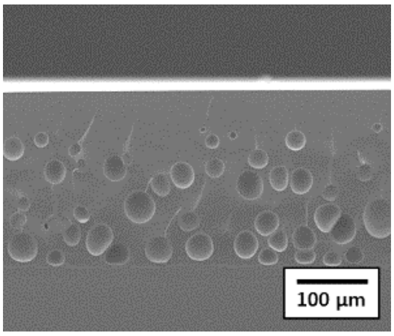

Figure 35. SEM image of foamed PHEMA film at 110 °C for 1 min without surfactant

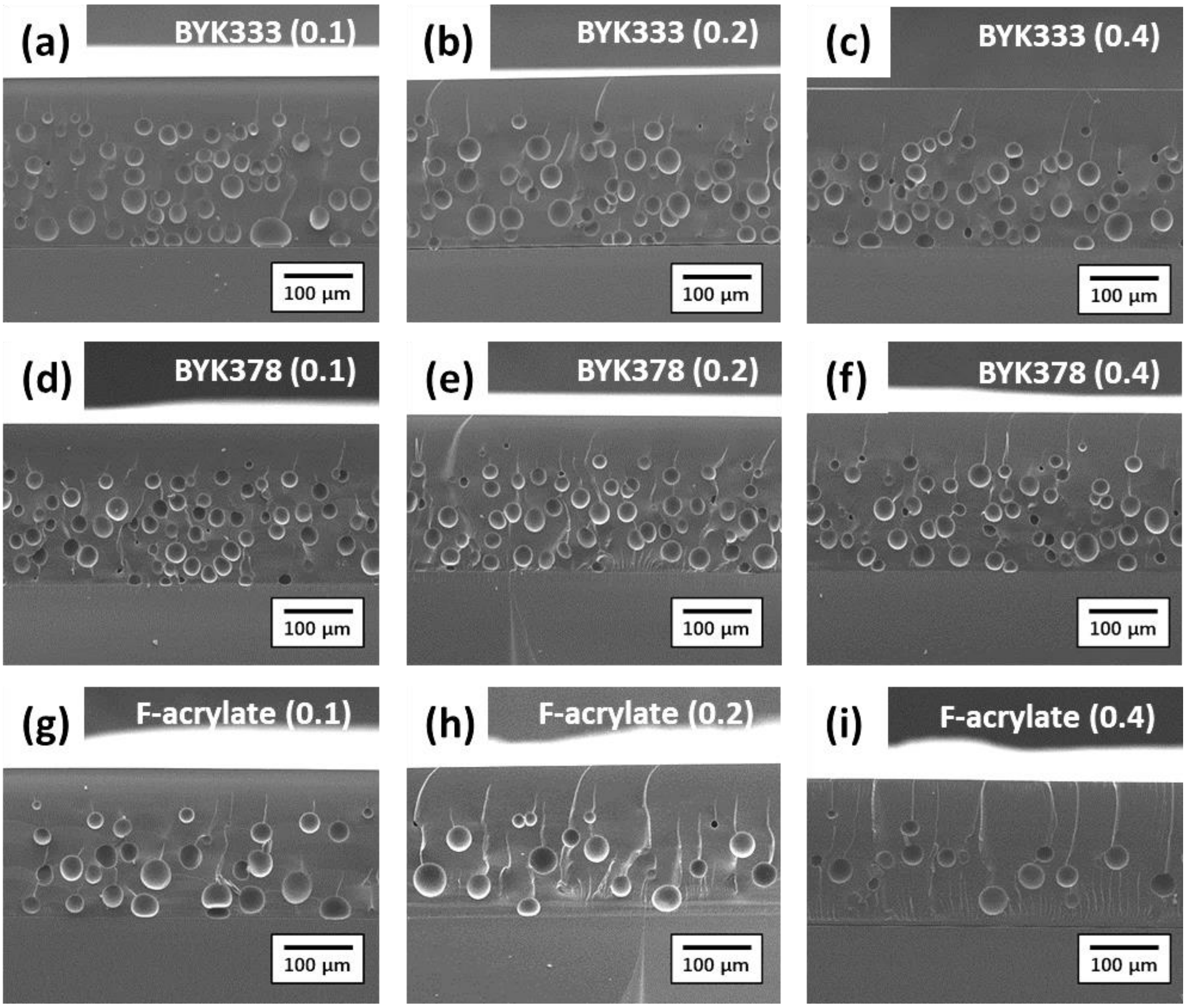

Figure 36. SEM images of foamed PHEMA film at 110 °C for 1 min with different surfactant and amount BYK 333 (a) 0.1, (b) 0.2, (c) 0.4, BYK 378 (d) 0.1, (e) 0.2, (f) 0.4, F-acrylate (g) 0.1, (h) 0.2, (i) 0.4 wt%

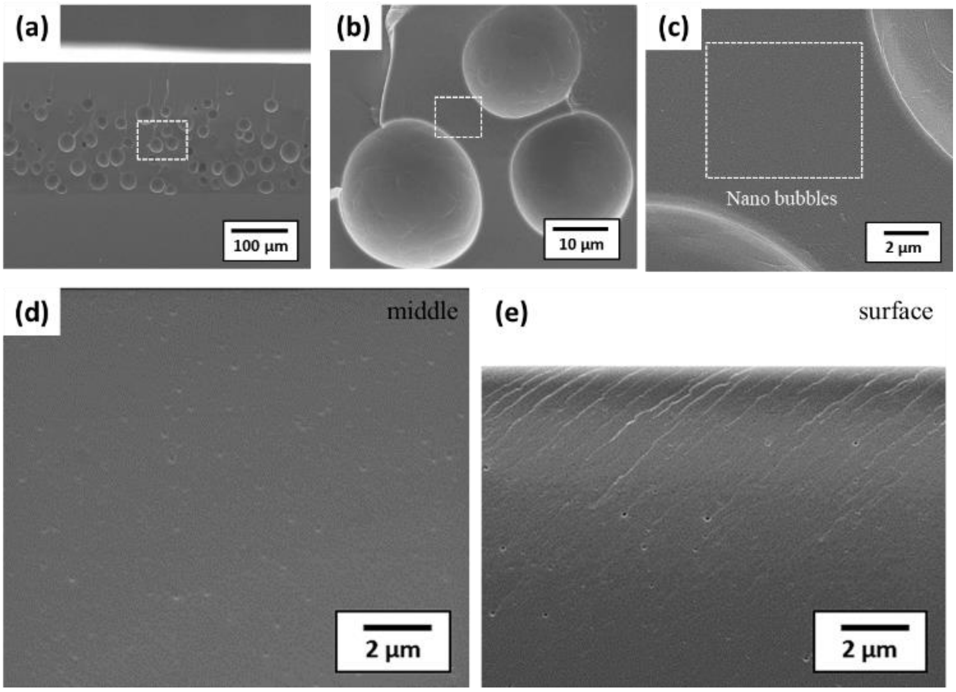

Figure 37. SEM images of foamed PHEMA film with BYK 378 0.4 wt% at 110 °C for 1 min, increasing magnification of rectangular area from (a) to (d), (e); near the surface

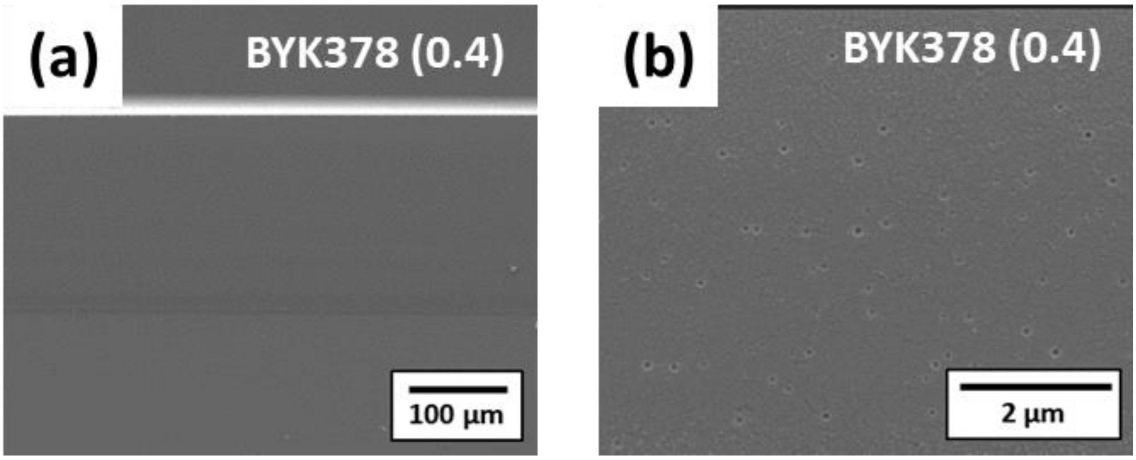

Figure 38. SEM images of foamed PHEMA film with BYK 378 0.4 wt% at 110 °C for 45 sec
(a) low magnification (b) high magnification in the middle of (a)

4.2.6 Kinetics of nitrogen generation (ABVN)

The PHEMA film remained clear until 10 sec and then started to turn opaque in 20 sec. **Figure 39** shows nanobubbles were formed throughout the entire PHEMA film when the film was heated for 10 sec. The mean diameter of the nanobubbles was 120 nm (**Figure 40 (a)).** It was hard to define the size of the smaller bubbles in between nanobubbles.

The nanobubbles grew very fast to microbubbles within another 20 sec as shown in **Figure 41**. Two types of bubbles were detected from the sample foamed for 30 sec - microbubbles in the range of 1 - 5 µm and nanobubbles with a mean diameter of 95 nm**.**

Transmittance was reduced from 90.6 to 28.0, while the haze value was increased from 3.39 to 89.0 during the additional 20 sec of foaming period. Optical properties of transmittance and haze are summarized in **Table 8**.

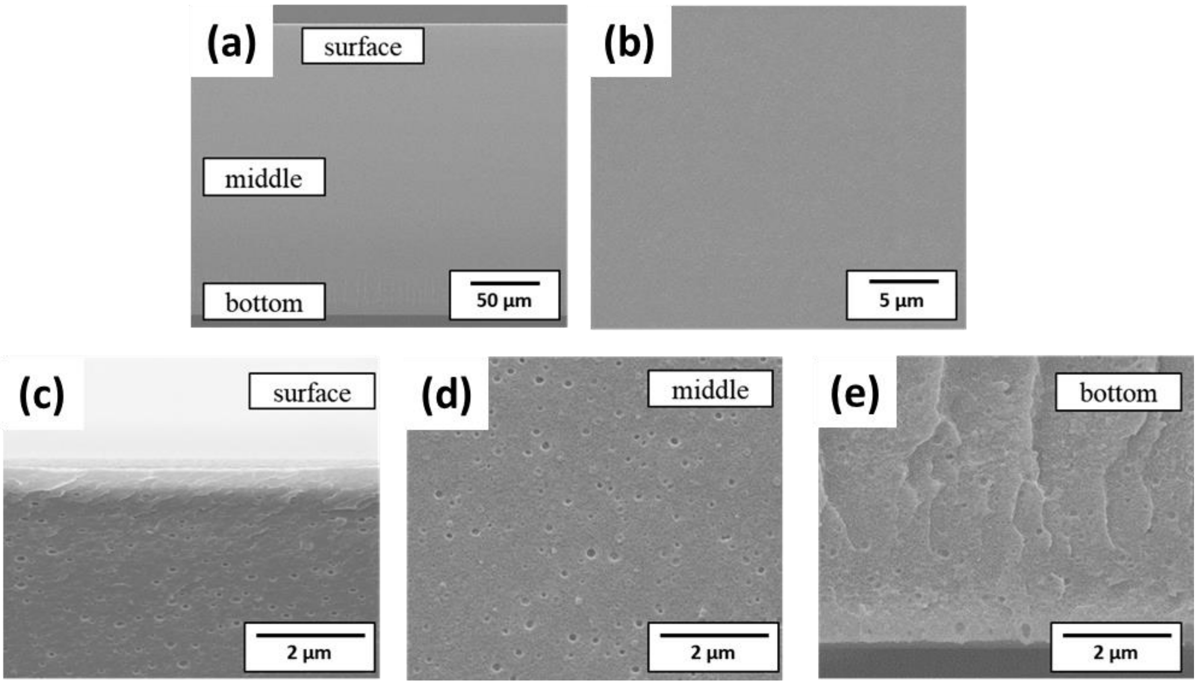

Figure 39. SEM images of foamed PHEMA heated at 110 °C for 10 sec (a) and (b); overview (c), (d), (e); high magnification of surface, middle, and bottom from (a)

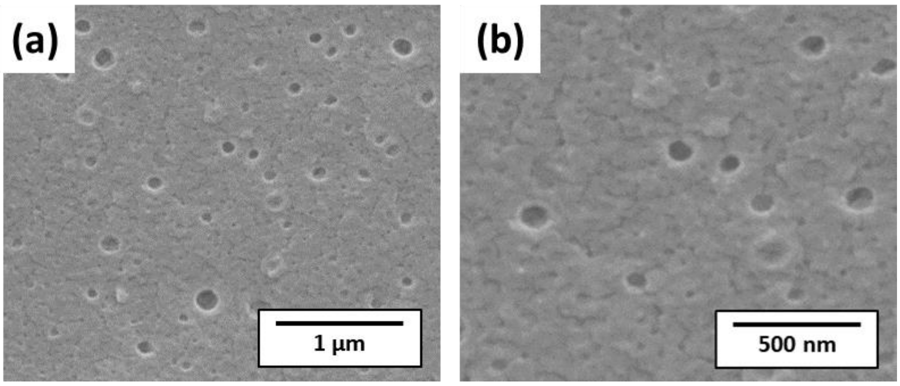

Figure 40. SEM images of high magnification of Figure 39 (d).

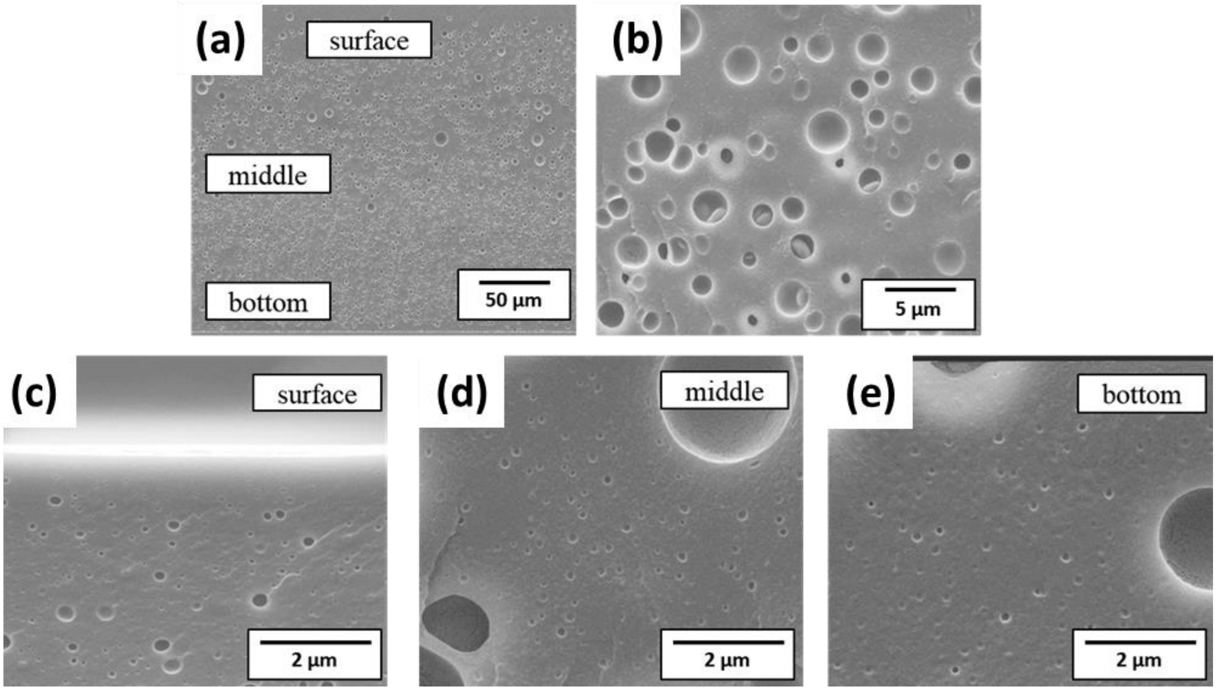

Figure 41. SEM images of foamed PHEMA heated at 110 °C for 30 sec (a) and (b); overview (c), (d), (e); high magnification of surface, middle, and bottom from (a)

PHEMA film (200 µm) with bubbles on microscope glass	Transmittance (%)	Haze (%)
Foamed at 110 °C for 10 sec	90.6	3.39
Foamed at 110 °C for 30 sec	28.0	89.0
PHEMA film (200 µm) without bubble on microscope glass	93.8	2.29

Table 8. Optical properties of the samples under different foaming time

4.2.7 Decomposition of ABVN by thermal heating and UV radiation

Starting from liquid state sol

Both samples turned slightly milky under the UV light within 1 min and no more change was detected with naked eyes. **Figure 42** and **Figure 43** show the SEM images of foamed PHEMA triggered either by heating only or by the combination of thermal heating and UV radiation.

In addition, two types of nanobubbles were observed – bigger bubbles with a mean diameter of 550 nm, and smaller bubbles with a mean diameter of 70 nm surrounded by the bigger bubbles. Once the UV radiation was applied, the density of bigger bubbles increased and the mean diameter of the bubbles decreased to 440 nm, while the size of the smaller bubbles remained same (mean diameter of 70 nm) as shown in white rectangles in **Figure 42** (d) and **Figure 43** (d). The thickness of the dense skin layer was slightly reduced by combining the UV radiation.

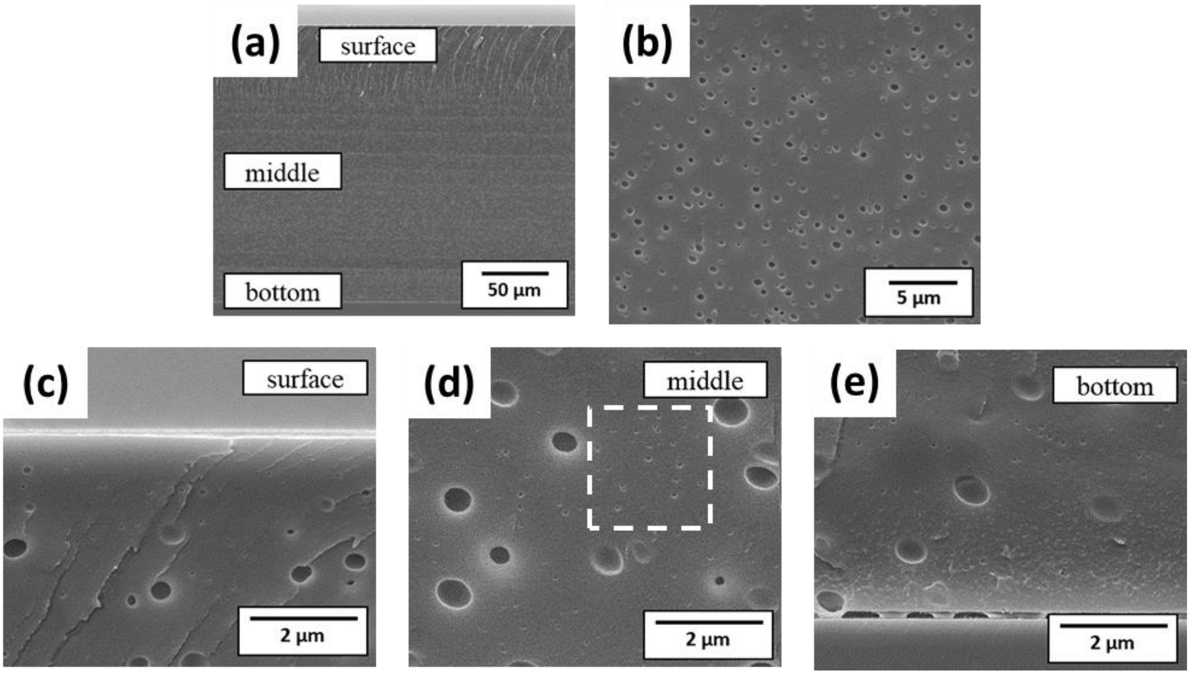

Figure 42. SEM images of foamed PHEMA heated directly at 70 °C for 5 min. (a) and (b); overview (c), (d), (e); high magnification of surface, middle, and bottom from (a)

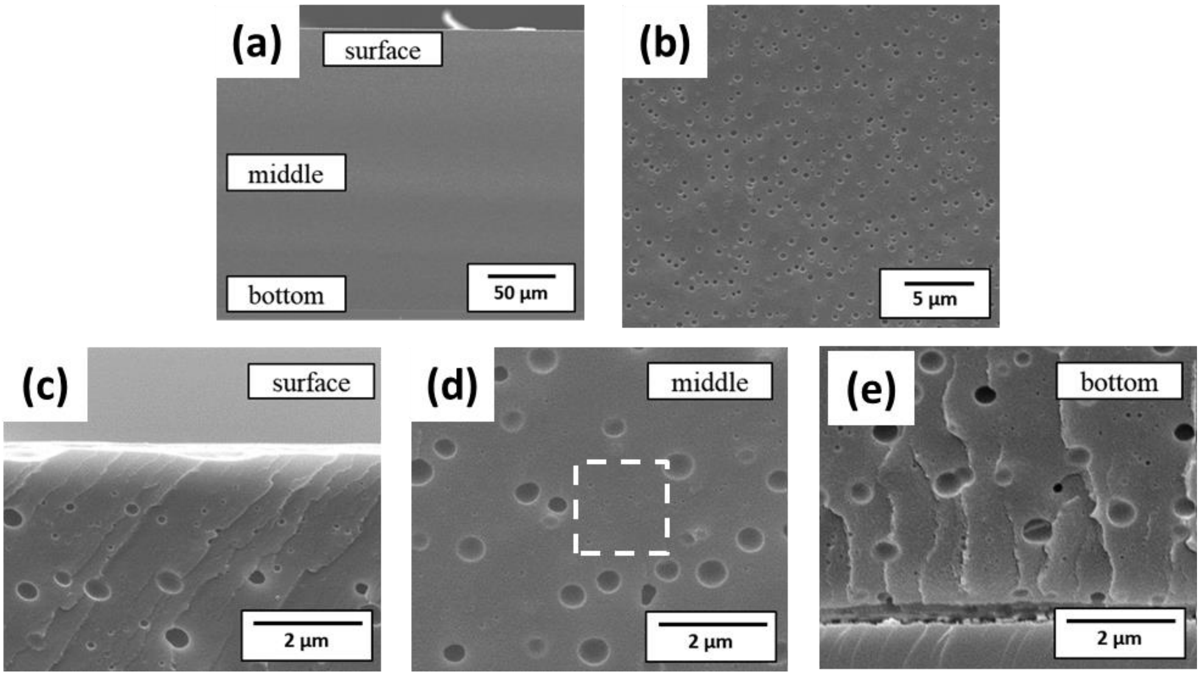

Figure 43. SEM images of foamed PHEMA heated at 70 °C and UV radiated at the same time for 5 min. (a), (b); overview (c), (d), (e); high magnification of surface, middle, and bottom from (a)

Starting from partially cured PHEMA

The film foamed starting from partially cured sol, followed by a combination of heating and UV radiation turned slightly opaque within 30 sec and nothing seemed to change for the naked eyes for the rest of the time. Compared to the samples starting from the liquid state, the density of bubbles significantly increased. The mean pore size of bubbles was 175 nm and the thickness of the dense skin layer was in the range of 200 - 300 nm.

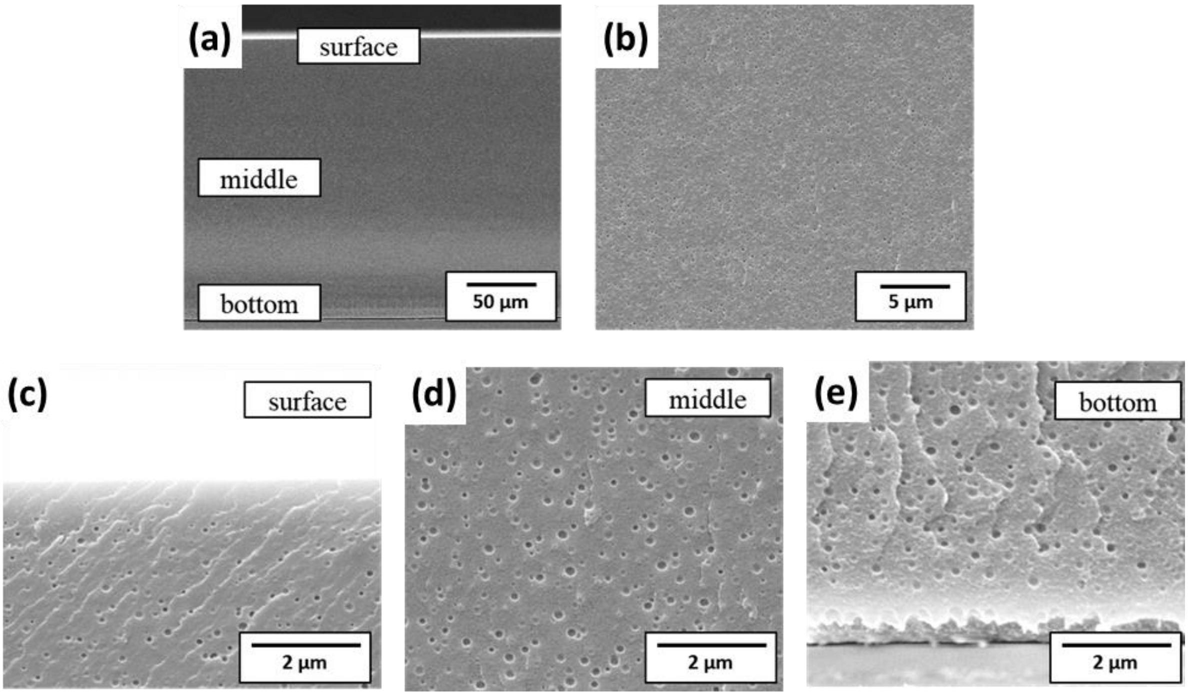

Figure 44. SEM images of foamed PHEMA after partial curing (2.5 min) followed by heated at 70 °C and UV radiation at the same time for 5 min.
(a), (b); overview (c), (d), (e); high magnification of surface, middle, and bottom from (a)

Optical properties of the sample are summarized in **Table 9.** Porous PHEMA showed 83.1 % of transmittance and 10.40 % of Haze. The refractive index of the PHEMA with nanobubbles was decreased from 1.51, without bubble, to 1.44.

PHEMA film (200 μm) with bubbles on the microscope glass		Transmittance (%)	Haze (%)
Starting from partially cured sol	Foamed at 70 °C + UV lamp	83.1	10.40
PHEMA film (200 μm) without bubble on the microscope glass		93.8	2.29
Microscope glass without PHEMA film		93.4	0.37

Table 9. Optical properties of the foamed PHEMA film starting from partially cured sol

5. Discussion

5.1 Azo-chemical initiator (AIBN) as a blowing agent

One step continuous foaming

AIBN was used as a blowing agent to generate gas (**Figure 22)**. The volume of 10 g HEMA monomer and PHEMA polymer is 9.35 ml (density: 1.07 g/cm^3) and 8.70 ml (density: 1.15 g/cm^3), respectively. In principle, when 0.32 g of AIBN (0.002 mol) is added into HEMA monomer and decomposes during the polymerization process, 0.002 mol of N_2 could be generated (**Scheme 1**).
One mol of nitrogen gas occupies 22.4 L at STP (standard temperature and pressure, 0 °C and one atmosphere pressure) by ideal gas law, meaning 0.002 mol corresponding to 44.8 ml of N_2 (0.002 mol *22.4 L/mol = 44.8 ml). At 60 °C, the volume increases up to 54 ml (44.8 * (1 + 60/273) = 54.65 ml), which is more than 6 times the volume of PHEMA, i.e. 8.70 ml. That explains why the volume expansion of the foamed PHEMA is up to 3 - 4 times compared to the initial volume of the solution. However, the missing part of the formed nitrogen gas is very likely diffused out before the solutions were fully cured.

It is worth to discuss the amount of N_2 gas generated by azo chemical, which is one of the essential factors for the generation of bubbles. As shown above, AIBN could produce nitrogen gas, which has 6 times the volume of the matrix. However, this volume is still relatively low compared to the CO_2 uptake used in supercritical fluid foaming. For example, up to 200 - 300 mg CO_2 could be absorbed in 1 g of PMMA at specific conditions [42, 43, 71]. Considering that the volume of 1 g of PMMA is 0.85 ml, the absorbed CO_2 has a volume of 101.80 ml (200 mg) and 152.69 ml (300 mg) at STP - nearly 120 and 180 times that the volume of the PMMA matrix when the external pressure is released. That volume could be increased further when the samples were immersed in a heating bath to initiate foaming (2S foaming). If the surface tension of the matrix is similar at the early stage of nucleation, the critical radius of the nucleation by nitrogen from AIBN is significantly increased compared to the nucleation by supercritical CO_2, according to the **Equation 5,** since the matrix is far less supersaturated.

Two step foaming

AIBN also generates two free radicals that change the reaction kinetics and the length of polymer chains. This makes it difficult to control the nucleation and the growth of bubbles at the same time, which has been always considered as a problem due to the microbubbles simultaneously trapped in polymers. Therefore, the UV starter Irgacure 819 was added into the solution to initiate the reaction and keep AIBN unreacted in the polymer matrix after polymerization. In other words, the process of polymerization and gas generation could be completely separated. It indicates AIBN could be used merely as a chemical blowing agent (CBA) afterward that could produce bubbles when the pre-cured films are post-heated up to the glass transition temperature (T_g) of the matrix. As a result, azo initiator AIBN, which decompose at relatively low temperature of 60 – 80 °C [24, 25], could be used instead of Azodicarbonamide (ADCA), which reacts around 200 °C [28-30]. **Figure 45** shows the absorption spectra of Irgacure 819 which absorbs up to 440 nm and AIBN that absorbs mainly around 340 nm. Therefore, a UV lamp with the wavelength of 405 nm was used to minimize the decomposition of AIBN during pre-curing process (**Figure 46**)

Another substantial benefit of the two-step foaming is that compared to the CO_2 foaming, which requires some hours to days for CO_2 soaking, AIBN could be directly available as a gas delivery substance when the pre-polymerization is finished, which takes less than 5 minutes. This new approach, therefore, takes advantages of both chemical and physical foaming processes and has not been reported in the literature before.

From the results, the transparent film turned opaque after foaming, when it contains AIBN (**Figure 23)**, meaning that bubbles were formed and light was scattered by that bubbles. The vertically stretched shape of the bubbles could be attributed to the expansion caused by ripening and buoyancy while the sample was being heated. The critical radius for the formation and expansion of the bubbles depending on the heating temperature and time will be discussed in detail in the following chapter.

In addition, the dense skin layer near the surface is a well-known phenomenon in chemical or physical foamed materials. Since the kinetics of gas diffusion near the surface is so fast, the material could not reach supersaturation to start the nucleation of bubble. Therefore, it is very difficult to produce bubbles near the surface of the film.

In conclusion, AIBN could be a candidate as a chemical blowing agent, particularly for the two-step foaming. However, the degree of supersaturation should be increased in order to make bubbles small and reduce the thickness of the un-foamed dense skin layer.

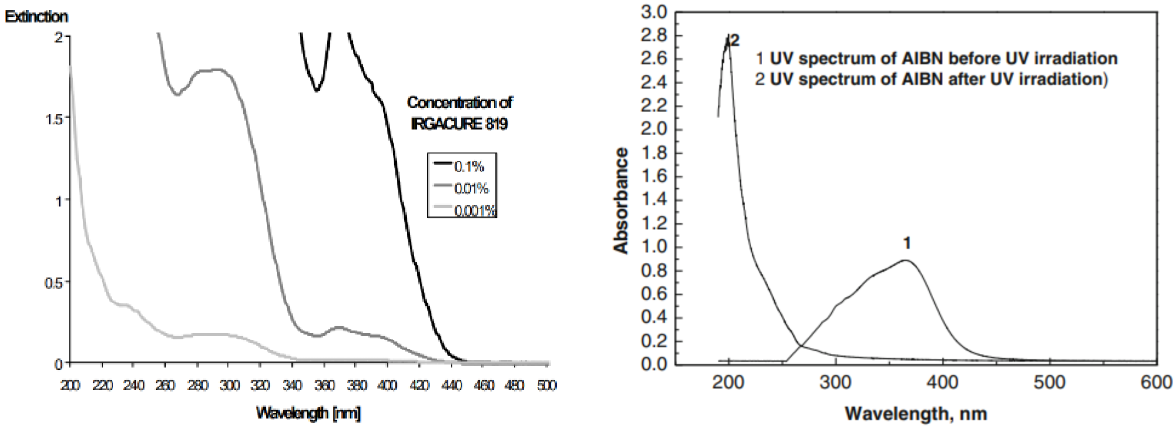

Figure 45. (left) Absorption spectrum of Irgacure 819 in Acetonitrile **[72]** and (right) UV-VIS spectra of AIBN before and after UV irradiation. Reprinted from [23] with permission, copyright (2014) Springer Nature

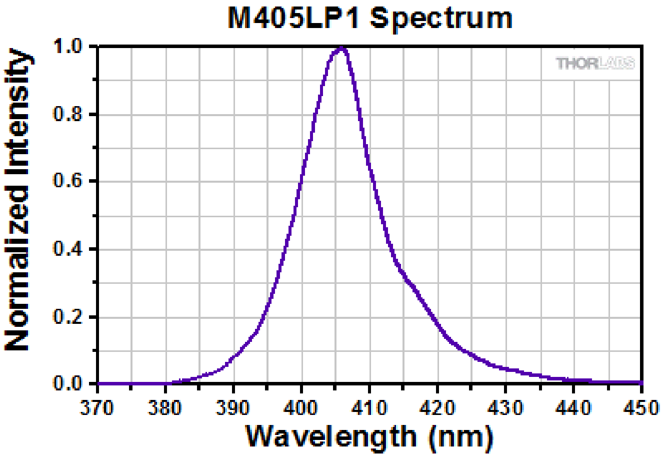

Figure 46. Normalized intensity of UV lamp used for pre-curing process **[73]**

5.2 Factors that affect the nucleation and growth of bubbles

5.2.1. Effect of the temperature

The aim of this experiment is to evaluate the effect of foaming temperature and time on the nucleation and growth of bubbles.

In general, more AIBN is thermally decomposed at higher temperature in shorter time, and generates more gas molecules as shown in **Figure 47**. For example, it takes 10 min until half of AIBN is decomposed at 100 °C (2.7 $K^{-1} * 10^3$) in solution, while it could occur in 2 min at 112 °C (2.6 $K^{-1} * 10^3$). In this experiment, it took only 10 sec until the matrix was supersaturated by nitrogen, and nucleation started at the highest temperature of 120 °C, whereas it took 1.5 min at 100 °C. In addition, the solubility of gas in the matrix decreases as the temperature increases. Moreover, the diffusion coefficient of the gas also increases at higher temperature and it enables for gas molecules to move in the material for the nucleation of bubbles. Therefore, the critical radius of bubbles also decreased when the matrix is quickly supersaturated at the early stage of the nucleation at higher temperature (**Figure 25** (b), (e), (h) in that order). **Equation 6** and **Equation 8** can explain this phenomenon as well.

Although it is possible to qualitatively discuss and demonstrate the effect of foaming temperature and time, it is difficult to directly measure the amount of nitrogen gas 1) dissolved in the metastable matrix or 2) diffused out from the surface or 3) used to make the bubbles, throughout the entire process including the decomposition of AIBN, diffusion of the gas inside and near the surface, supersaturation of the matrix, nucleation of bubbles, ripening of the existing bubbles, and while another nucleation occurs simultaneously. Besides, all those processes have interactive effects on each other.

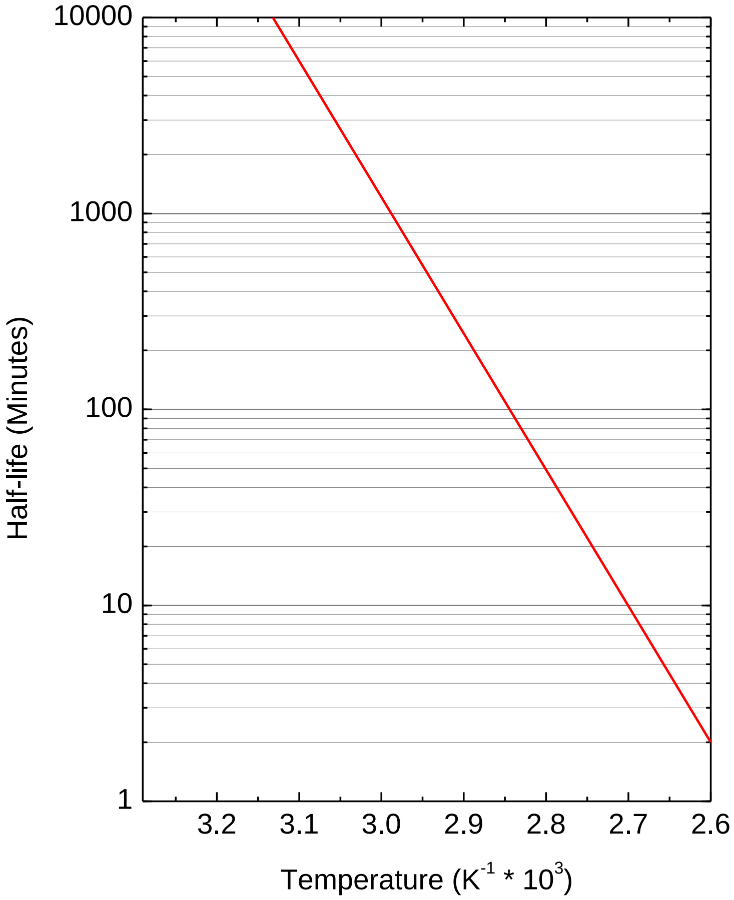

Figure 47. Half-life of AIBN in solution [74]

Still it is worth to compare the results with similar studies on the supercritical CO_2 foaming to verify the explanation. First, the fast generation of nitrogen at higher temperature is compatible with the different rates of pressure release during the 1S supercritical CO_2 foaming. Z.-M. Xu et al. studied the effect of the depressurization rate on the foaming process of polypropylene (PP) and concluded ‘when the depressurization rate is low, the level of supersaturation is low and the driving force for the cell nucleation is weak. Thus, the number of cell nuclei per unit volume and the cell density are small’ (**Figure 48**). [75].

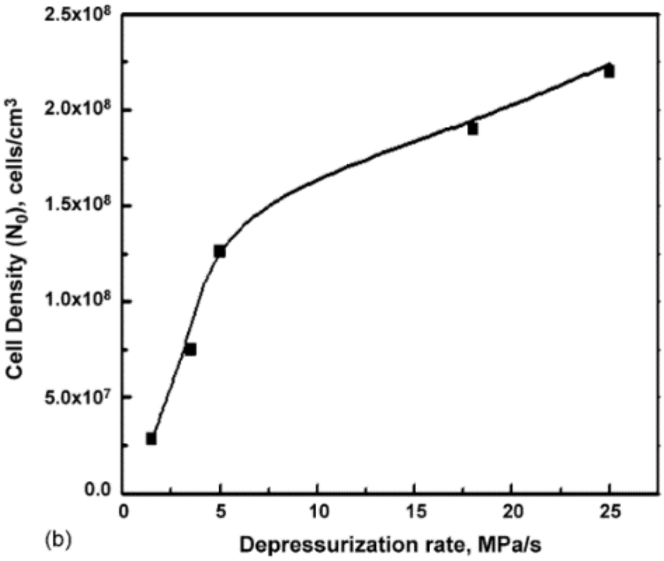

Figure 48. Effect of the depressurization rate on the average cell density of PP.
foaming temperature: 154 °C; saturation pressure: 25 Mpa.
- Reprinted from [75]. Copyright (2007), with permission from Elsevier.

Second, the physical properties of the matrix change as well with increasing temperature during foaming. I. Tsivintzelis et al. studied the effect of the foaming temperature on the structure of the PS foams, while keeping the weight fraction of the dissolved CO_2 constant (w = 0.11) as shown in **Figure 49**. They concluded 'at higher temperatures the expansion of foams becomes easier, due to the viscosity reduction, while the latter one to the fact that the larger amount of dissolved CO_2 tends towards the formation of more expanded foams' [39]. In addition, the morphology change in the bubbles from spherical shape at the early stage to the vertically stretched shape afterwards could be attributed to the ripening and buoyancy effect to the vertical direction as shown in **Figure 50**.

Furthermore, increasing the temperature far above the T_g of the matrix is not recommended as well since the matrix loses its strength at a certain point, and the effect of accelerated diffusion of gas overwhelms other positive effects [53, 76].

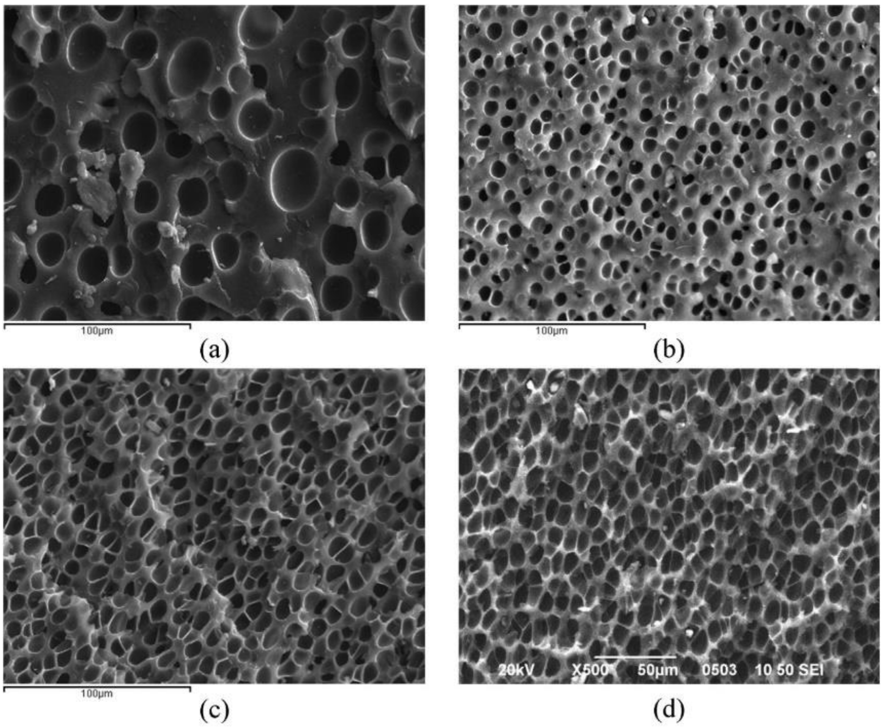

Figure 49. Porous polystyrene structures obtained for dissolved CO_2 weight fraction equal to **w= 0.11** : (a) 178.3 bar, **342 K** (b) 221.1 bar, **351 K**, (c) 279.7 bar, **364.15 K**, and (d) 353.9 bar, **381 K**.
Scale bar (a), (b), (c) 100 µm, (d) 50 µm
– Reprinted from [39] Copyright (2016), with permission from Elsevier.

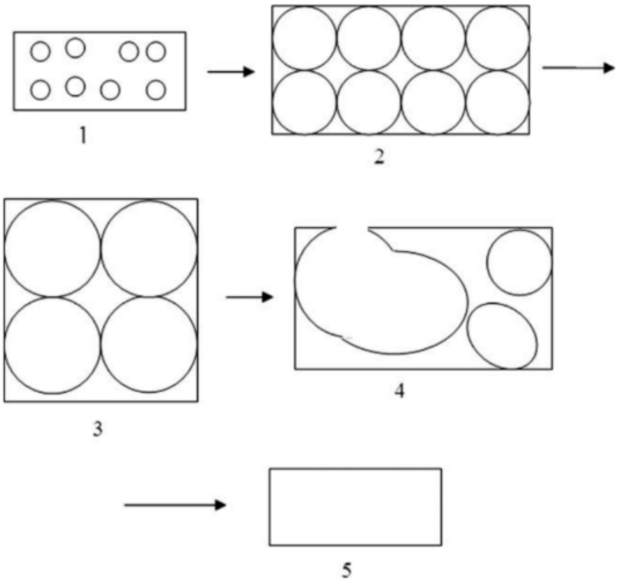

Figure 50. Schematic of formation of cellular structures in foaming process.
– Reprinted from **[53]** with permission.

The reason for the reduced thickness of the dense skin layer could be also explained based on the two effects. Although the diffusion of gas from the material was accelerated by increasing temperature, the kinetic of chemical decomposition of AIBN exceeded the diffusion effect. Therefore, the non-supersaturated layer became thinner with increasing temperature. However, there was still a critical thickness of films, and bubbles could not be formed below the thickness at a given temperature, which is described in **Scheme 7**.

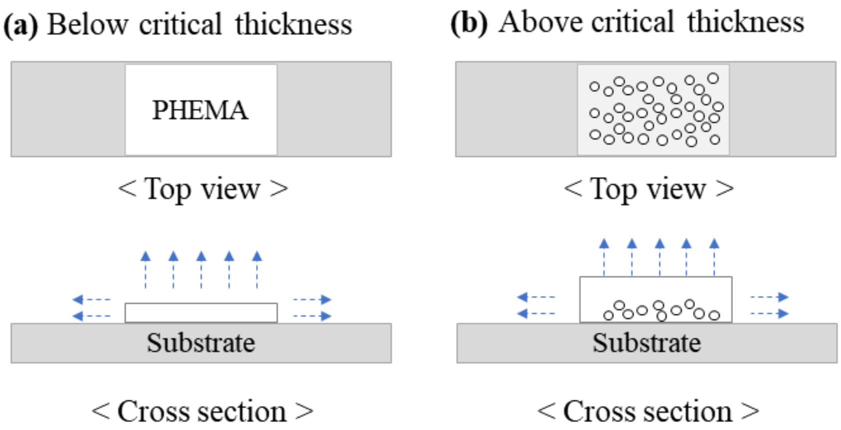

Scheme 7. Effect of the temperature and thickness on the nucleation of bubbles
(a) below the critical thickness gas diffuses out, (b) above the critical thickness, bubbles form and stay

In conclusion, the higher the foaming temperature, the faster AIBN decomposes and bubbles grow at the same time. Besides, the nucleation rate increased as well due to the reduction of viscosity. Nevertheless, to control the foaming temperature and time in the conventional way of heating on the hot plate is insufficient to make nanobubbles. Moreover, the formation of the un-foamed skin layer is still inevitable.

5.2.2 Effect of gas saturation of the matrix – nitrogen soaking

From the previous experiment, it was found that a certain period of time was needed before the nucleation started. In the beginning, the nitrogen gas generated from AIBN could not be utilized to make bubbles, but the gas is dissolved within the matrix. Once the amount of gas formed by chemical decomposition exceeds its solubility within the matrix, supersaturation occurs. The nucleation of bubbles could start only when certain amounts of AIBN are already consumed. Therefore, the nitrogen soaking simply aimed to accelerate the nucleation of bubbles by making the matrix supersaturated at the early stage of the foaming. This kind of technique is so-called ‘Mixed physical/chemical blowing agents’ and is commonly used to produce foams with very low density. However, there is little knowledge on the combination of UV pre-cured film containing AIBN and nitrogen soaking.

The results showed that this hypothesis was seemingly right. The films with the combination of nitrogen soaking and AIBN showed more nucleation of bubbles in a much shorter time (**Figure 27**) compared to other films, e.g. the sample containing AIBN without soaking from the previous chapter (**Figure 25**, (d), (e), (f)) or the reference sample, only N_2 soaked without AIBN (**Figure 29**),

Interestingly, there were two different types of bubbles observed by the SEM, and the boundary between those two areas was clearly observed (**Figure 28**). The bubbles near the surface, which were not detected from non-soaked samples in the previous chapter, were produced mainly due to the fast desorption of the absorbed gas in the polymer matrix triggered by increasing the temperature. That is the key mechanism for the physical foaming process (2S) since the solubility of gas at higher temperature becomes low. However, it was proven from the control sample that the amount of absorbed gas itself was not enough to produce many nucleation sites without the generation of nitrogen by AIBN decomposition (**Figure 29**). It means that the synergistic effects of both, desorption of nitrogen during the soaking process and decomposition lead to the smaller bubbles near the surface.

It is worth to note that the density of bigger bubbles near the bottom of the film was decreased, although the number of smaller bubbles near the surface increased. One possible explanation of less nucleation would be that there are two different types of nitrogen gradient from bottom to surface caused by physical desorption and chemical decomposition of AIBN when the temperature of the film increases. When those synergistic effects accelerate the supersaturation near the surface at the early stage, it results in more nucleation. On the other hand, the remained bottom part becomes less saturated, since the nitrogen generated later by AIBN decomposition is used for the ripening of the already existing bubbles rather than another nucleation.

In conclusion, soaking of the nitrogen gas before the foaming process makes the matrix supersaturated in general and has a positive effect on the nucleation of bubbles. However, if the kinetics of delivering gas from physical and chemical blowing agents are different, inhomogeneous nucleation and abnormal growth could occur. In addition to that, there are a couple of disadvantages in soaking process. First of all, high pressure (> 50 - 200 bar) is required to achieve more absorption of gas, and saturation takes relatively long (2 - 10 h) depending on the thickness of the film [76]. Second, once the pressure is released, gas diffuses out of the film continuously over time. For example, Krause et al. studied the effect of the transfer time on the foaming structure of polysulfone (PSU) film (100 μm) and reported that significant amounts of gas diffuse out within 1 to 20 min, changing the structure of foamed PSU as shown in **Figure 51**. The shorter the transfer time, the more gas is available for the foaming. Besides, the diffusion rate of absorbed gas is the fastest right after releasing the pressure. Forest et al. reported that CO_2 uptake in PMMA could be reduced from 19 wt% after releasing the pressure to 15 wt% within 10 min as shown in **Figure 52** [43].

In this study, the samples also showed poor reproducibility because of the diffusion during the transfer of the samples from the autoclave to the hot plate after releasing the pressure. This spontaneous change within short time is the main drawback of this technique. Therefore, alternative ways to increase the driving force for nucleation are needed.

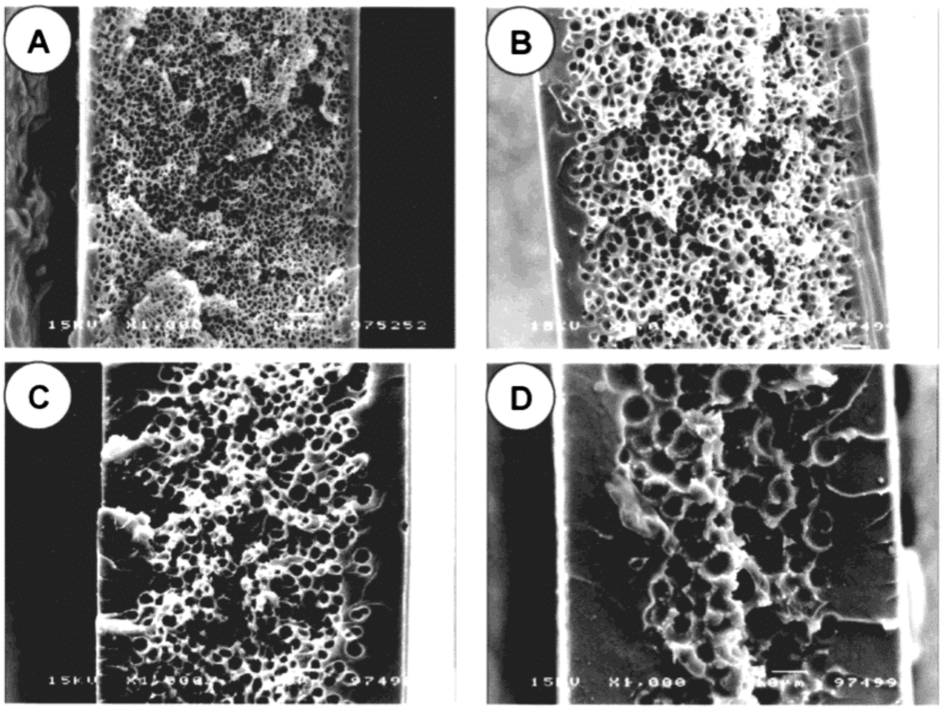

Figure 51. SEM micrographs of foamed PSU films as a function of transfer time, viz., (A) = 1 min, (B) = 5 min, (c) = 10 min, and (D) = 20 min. Magnification: 1000; the white horizontal bar indicates 10 µm. Saturation conditions: 50 bar of CO_2 for 2 h, foaming conditions: 180 °C for 30 sec, T_g of PSU : 193 °C – Reprinted with permission from [76]. Copyright (2001) American Chemical Society

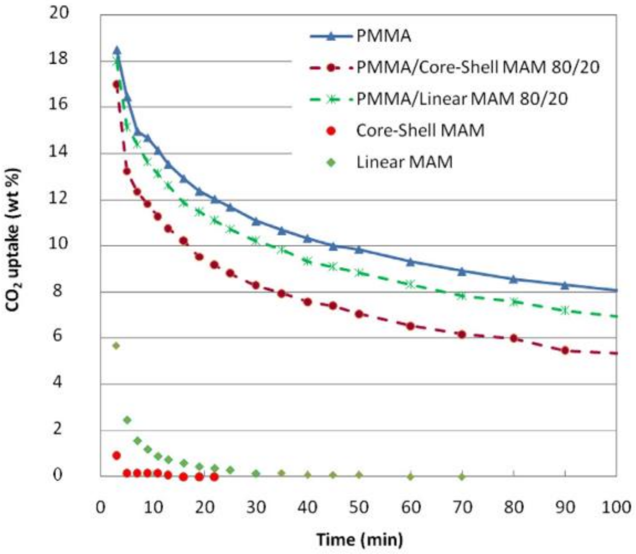

Figure 52. Desorption test for PMMA/cMAM materials after a saturation stage at room temperature: CO_2 uptake as a function of the time (T = 0 at the end of the pressure drop) – Reprinted from [43]. Copyright (2015), with permission from Elsevier.

5.2.3 Effect of the external pressure and surface constraining layer

This experiment was intended to prevent the diffusion of nitrogen gas from the surface to the air in order to make the matrix more supersaturated. That should lead to a smaller critical radius of bubbles compared to that of bubbles generated without external pressure on the surface. However, the results showed the opposite. Although the size of bubbles decreased and the size distribution became narrow (**Figure 31**), there were fewer bubbles found in the samples prepared under the external pressure compared to the ones foamed at ambient condition.

From the free energy point of view, I tried to increase ΔP, and hence the degree of supersaturation by blocking the diffusion from the surface to the outside. However, there is also an energy requirement to overcome the creation of interface of bubble. According to the **Equation 3** and **Equation 6** of the critical free energy for the nucleation, a change in the surface tension has a more significant effect than the degree of supersaturation. If the pressure is induced at the temperature above T_g, the surface tension of the meta stable matrix increases as a result of the external pressure. In addition, the internal pressure of a single bubble is the sum of the Laplace pressure and the pressure of the surrounding. In other words, the reduction of the diameter of bubbles increases the partial pressure in the bubbles, leading to increase the gas solubility to the matrix. All these factors together have affected and changed the behavior of the bubbles.

Interestingly, the bubbles under the applied pressure could not expand and remain as spheres (**Figure 30**), while most nano-foamed materials by using supercritical CO_2 have pores which are randomly stretched to all directions. It verifies the expansion of pores is inevitable during the CO_2 foaming process, although it is assumed that the foaming is performed in a very short period.

The un-foamed skin layer indicates that diffusion is still more dominant near the surface than the nucleation of bubbles at all conditions used so far.

Figure 32 showed the effect of the surface constraining layer on the nucleation of bubbles. Such effect is well-known in the supercritical CO_2 foaming as shown in **Figure 53**. With the surface confinement, more gas molecules are available for the formation of bubbles. That explains the reason for the reduction of the dense skin layer from 30 – 50 µm to below 10 µm when the sample was foamed in between two microscope slides. In other words, the unsaturated layer becomes thinner by suppressed diffusion.

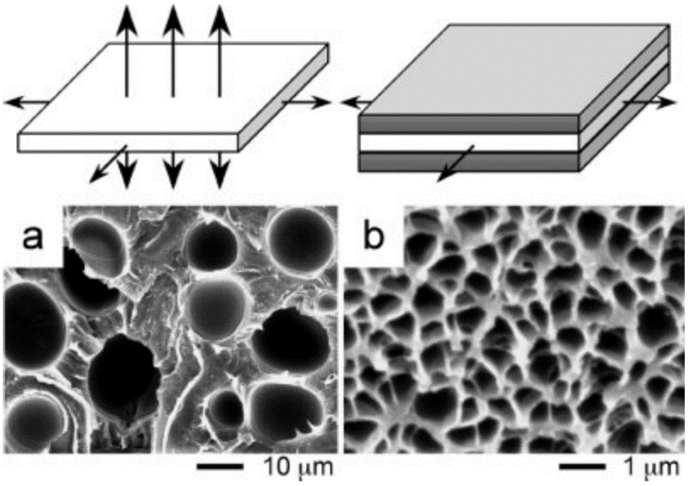

Figure 53. SEM images of PMMA films foamed (a) without and (b) with surface confinement, schematically depicted in the accompanying illustrations, in supercritical CO_2 at 40 °C and 340 atm.
- Reprinted with permission from **[77]**

In conclusion, the application of external pressure could hinder the diffusion of gas from the surface and make the bubbles smaller with spherical shape. However, the side effects of increasing the surface tension, viscosity, and solubility of the matrix exceeded the benefits of the positive effects, reducing the density of bubbles. Besides, the surface constraining layer, as an alternative, proved the effect of the confinement, showing more bubbles and reduced un-foamed layer. Despite the improvement, the mean diameter of 20 µm was too big to avoid scattering and made the film opaque.

5.2.4 Laser heating as a post heating process

This experiment was intended to minimize the area heated to the temperature above the T_g so that the surrounding matrix which is below T_g could hinder the diffusion. In other words, higher aspect ratio of the heated area surrounded by rigid matrix was aimed as shown in **scheme 8**. I expected, therefore, more nucleation of bubbles in the heated region.

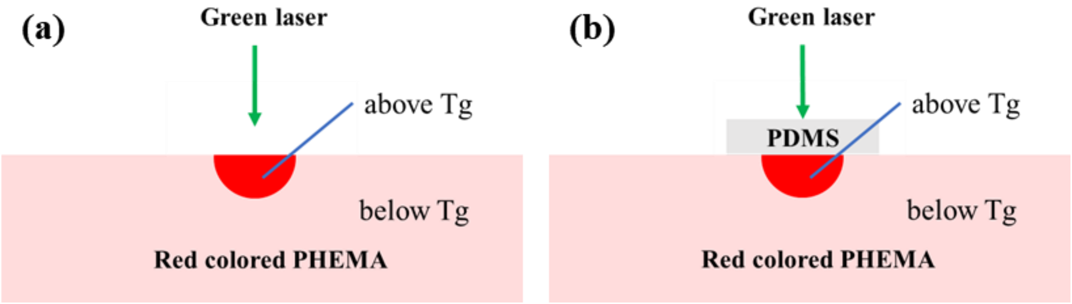

scheme 8. laser heating by absorption of green laser in the red colored PHEMA
(a) open surface and (b) surface confinement with PDMS

Laser heating with open surface

When the surface is open to air, it was impossible to generate nano size bubbles under various conditions, and only micro sized one formed and the surface was always bulged. Considering the width of the focused laser spot was below 100 μm and each speed of the movable arm with the sample was 8, 16, and 32 mm/sec, the heating did not last longer than 12, 6, 3 ms at any point. It took around 10 sec until the first nucleation started on the hot plate at 120 °C, it is assumed that the temperature in the middle was skyrocketed in a short time. Probably, this over-heating by laser quickly decomposed AIBN, making the film oversaturated in a short time. The surface tension of the matrix, on the other hand, would decrease as the temperature of polymer increased far beyond the T_g. Swelling to the vertical direction is reasonable since the other area of the film remained below T_g.

However, the size of bubbles and the thickness of the un-foamed layer were significantly reduced compared to the films foamed by conventional heating on the hot plate (**Figure 34 (b)**). It indicates the benefit of fast heating in isolated area. i.e. fast decomposition of AIBN and suppressed diffusion.

It should be noted that small variation of the heating time in ms range could make a huge impact on the microstructure of the material and surface roughness, which can be the biggest drawback of this process.

Laser heating with surface constraining layer

Since the effect of a surface confinement was shown from the previous experiment (**Figure 32** from (4.2.3)), a PDMS layer was used to block the diffusion from the surface and tightly compressed on the PHEMA sample.
Each single spot heated for 0.25 ms (**Figure 34)** indicates that the temperature of the spot was increased far above the T_g of the matrix, thus the bubbles could be generated in such a short period. In addition, as a result of the PDMS layer, the gas diffusion from the surface was efficiently suppressed and no bulging was found in the heated area. Finally, nanobubbles were achieved. This sample showed the smallest bubbles with the lowest size distribution.

On the other hand, the power of the laser and corresponding radiation time should be controlled very precisely. Otherwise, a small deviation from the required conditions will lead to either no nucleation of bubbles or micro size bubbles.

In conclusion, using a laser could be an alternative way for heating the film and it is the fastest way to increase the temperature of the film to above T_g. I expected, therefore, the biggest ΔP, supersaturation by AIBN decomposition. However, over-heating of the matrix far above the T_g is inevitable to achieve small bubbles and the surface bulging occurred. To solve the problem, surface confinement was suggested afterward. Despite the positive progress in the size of bubbles down to nanobubble and narrow distribution, using a laser seems unpractical due to the difficulty of the precise control of the experimental parameters. Besides, (red) dyeing chemical is also required in order to absorb the (green) laser.

5.2.5 Effect of surface tension (surfactants)

According to the Gibb's energy equation (**Equation 6)** for the nucleation of bubble, the critical energy is proportional to the γ^3 and inversely proportional to the ΔP^2. That means, the surface tension of the surrounding matrix has the biggest impact on the nucleation. It is worth to note that increasing the amount of absorbed gas also has a positive effect itself on reducing the surface tension of mixture according to **Equation 7**. Therefore, for the CO_2 foaming process, higher uptake of the saturated gas has only positive effect on the nucleation. However, the surface tension of the metastable polymer is not directly measurable and keeps changing. Nevertheless, it is approximated with the surface tension of the microscopic interface at equilibrium. [25]

$$\gamma_{mix}^{1/r} = \left(1 - w_{CO_2}\right) \gamma_{pol}^{1/r}$$

Equation 8. the surface tension of mixture with neat polymer and CO_2 gas↵

Many researches have focused not only on controlling the foaming pressure and temperature but also adding surfactants or nanoparticles to increase the nucleation [78-82]. Besides, blending or block-co-polymers with different surface tension and gas affinity have been also used for tuning the porosity [45, 46, 48-51, 82-87]. However, preparing the starting materials is rather complicated compared to neat polymers.

Therefore, I tested in these experiments various surfactants to characterize their effect on the nucleation of bubbles. Commercially available BYK 378 and BYK 333 are both polyether-modified polydimethylsiloxanes and widely used to reduce the surface tension in polyurethane and acrylate-based coating sols. Unfortunately, their exact composition is a trade secret. 1H, 1H, 5H-Octafluoropentyl acrylate **(Figure 54)** is a fluoro acrylate used to reduce the surface tension.

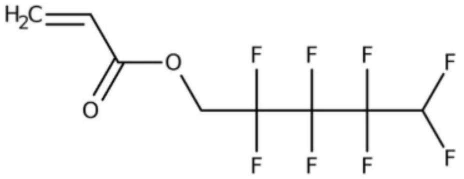

Figure 54. 1H, 1H, 5H-Octafluoropentyl acrylate

The addition of BYK surfactants to the mixture led to more microbubbles, showing the effect of reducing the surface tension. The number of microbubbles is proportional to the number of stable bubbles at the early stage. The experiments showed, furthermore, that the chosen different concentrations of BYK surfactants did not lead to a significant effect on the overall formation of ‘micro’ bubbles. On the other hand, the foamed HEMA that contained 1H, 1H, 5H-Octafluoropentyl acrylate had fewer microbubbles than the reference sample. The higher the concentration of it is, the less the microbubbles form. The reason for this is somewhat unclear, a potential explanation could be that the fluoro acrylate, which is not a typical surfactant, participates in the polymerization reaction and is consumed during the process. When the first bubbles nucleate, it could be that the fluoro acrylate is forming a kind of shell on their surface with the fluoropentyl-chain turned towards the inside of the bubble. During the ongoing polymerization this shell could be solidified faster, hindering a further growth of the bubble. Therefore, the rest of the formed nitrogen is not used for ripening of the bubble but instead it is diffusing out. This effect seems to be stronger with increasing amount of fluoro acrylate.

Interestingly, nanobubbles were found within the sample with 0.4 wt% of BYK 378 (**Figure 37**). The nanobubbles were detected in between big microbubbles, while no nanobubbles were found within the other samples. It indicates that there are different nucleation and growth mechanisms of bubbles between the sample with 0.4 wt% of BYK 378 and the others. If the surface tension decreases down to the certain point at which the critical radius of the nucleation became sub-micron, nanobubbles could be generated and remain stable according to the **Equation 5**. Those bubbles could grow as well with time by the diffusion of gas called ripening or by merging when two bubbles encounter. When two bubbles merge into one, the interfacial energy is reduced and so does the energy of the system [1].

However, if the critical radius for the nucleation of bubbles does not get to the nano level, only big microbubbles could be generated and detected with low density. In that case, the growth of the microbubbles occurred merely by the diffusion of gas molecules, without the appearance of nanobubbles.

To proof the hypothesis, every film with different surfactants and concentration was foamed until just before it turned to opaque. There were only nanobubbles found in the sample containing 0.4 wt% BYK 378 without any appearance of microbubbles (**Figure 38**), showing the assumption was correct. Nanobubbles were not detected for the other samples.

5.2.6 Kinetics of nitrogen generation (ABVN)

In this experiment, ABVN was used instead of AIBN since ABVN decomposes faster than AIBN at the same temperature as shown in **Figure 55**. The temperature for 10 hours half-life of AIBN and ABVN is 65 °C and 51 °C, respectively. Likewise, it takes 10 min for AIBN until it decomposes by half in a solution at 100 °C (2.7 K^{-1}* 10^3), while it takes only 1 min for ABVN.

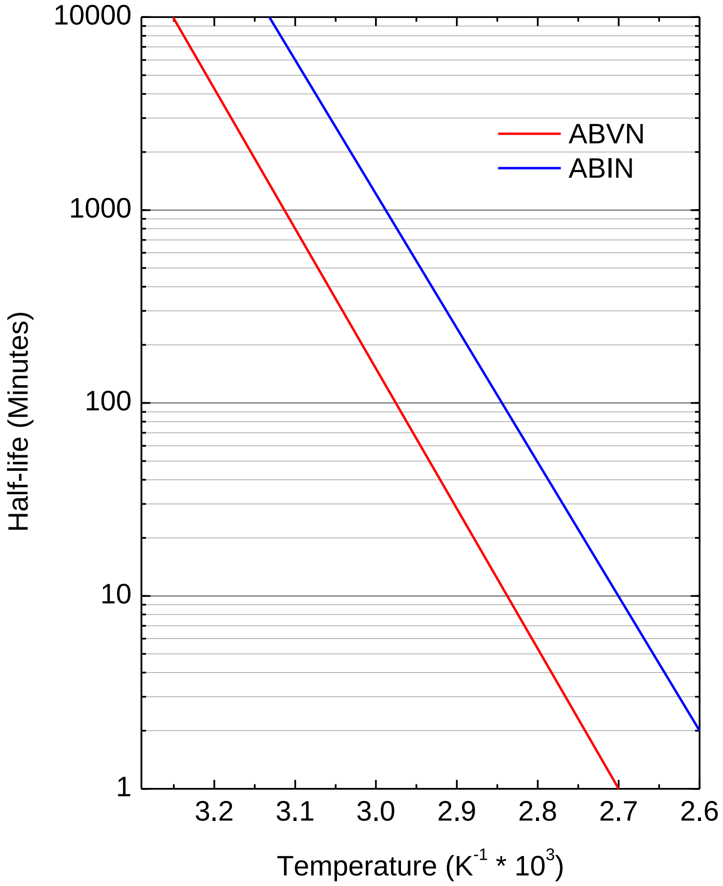

Figure 55. Half-life of ABVN and AIBN in solution [74]

According to the gas-burette experiment from Liang-Zhi Guo et al., when using ABVN , the volume of the nitrogen gas is 4.3 (0.64/0.15), 3.3 (1.51/0.46), and 2.9 (4.68/1.61) times higher than that of AIBN at 60 °C, 70 °C, and 80 °C within 10 min as shown in **Figure 56** [27]. In this experiment, the weight ratio of ABVN was two times higher than that of AIBN.

Since the molecular weight of AIBN and ABVN is 164.21 g and 248.37 g, the molecule ratio of ABVN is 1.3 times higher than that of AIBN. In brief, ABVN could generate much more nitrogen gas in shorter time than AIBN, i.e. at least 3.8 times (2.9 * 1.3= 3.8) at 80 °C within 10 min.

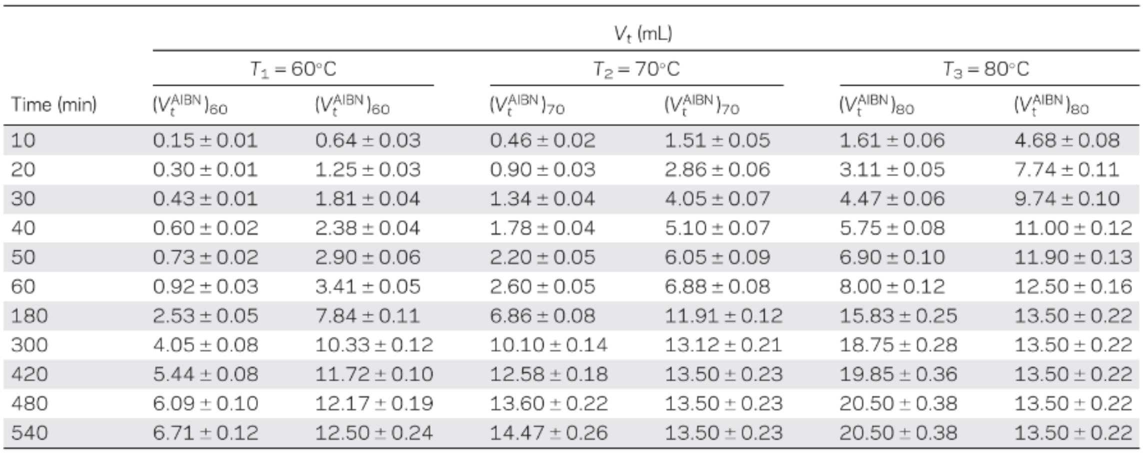

	V_t (mL)					
	$T_1 = 60°C$		$T_2 = 70°C$		$T_3 = 80°C$	
Time (min)	$(V_t^{AIBN})_{60}$	$(V_t^{AIBN})_{60}$	$(V_t^{AIBN})_{70}$	$(V_t^{AIBN})_{70}$	$(V_t^{AIBN})_{80}$	$(V_t^{AIBN})_{80}$
10	0.15 ± 0.01	0.64 ± 0.03	0.46 ± 0.02	1.51 ± 0.05	1.61 ± 0.06	4.68 ± 0.08
20	0.30 ± 0.01	1.25 ± 0.03	0.90 ± 0.03	2.86 ± 0.06	3.11 ± 0.05	7.74 ± 0.11
30	0.43 ± 0.01	1.81 ± 0.04	1.34 ± 0.04	4.05 ± 0.07	4.47 ± 0.06	9.74 ± 0.10
40	0.60 ± 0.02	2.38 ± 0.04	1.78 ± 0.04	5.10 ± 0.07	5.75 ± 0.08	11.00 ± 0.12
50	0.73 ± 0.02	2.90 ± 0.06	2.20 ± 0.05	6.05 ± 0.09	6.90 ± 0.10	11.90 ± 0.13
60	0.92 ± 0.03	3.41 ± 0.05	2.60 ± 0.05	6.88 ± 0.08	8.00 ± 0.12	12.50 ± 0.16
180	2.53 ± 0.05	7.84 ± 0.11	6.86 ± 0.08	11.91 ± 0.12	15.83 ± 0.25	13.50 ± 0.22
300	4.05 ± 0.08	10.33 ± 0.12	10.10 ± 0.14	13.12 ± 0.21	18.75 ± 0.28	13.50 ± 0.22
420	5.44 ± 0.08	11.72 ± 0.10	12.58 ± 0.18	13.50 ± 0.23	19.85 ± 0.36	13.50 ± 0.22
480	6.09 ± 0.10	12.17 ± 0.19	13.60 ± 0.22	13.50 ± 0.23	20.50 ± 0.38	13.50 ± 0.22
540	6.71 ± 0.12	12.50 ± 0.24	14.47 ± 0.26	13.50 ± 0.23	20.50 ± 0.38	13.50 ± 0.22

Figure 56. Changes in the amount of gas give off by AIBN and ABVN over time
at different temperatures in gas-burette experiment
– Reprinted from **[27]** with permission.

The entire foaming time was significantly reduced to 10 sec (**Figure 39**), while the density of bubbles was highly increased. In addition, the sample with ABVN started to turn white in about 20 seconds, which is much faster than that of AIBN, i.e. 45 sec – 1 min. **Figure 41** showed how fast nanobubbles can grow to microbubbles within 20 sec when ABVN is used. Beside the microbubbles, there were also nanobubbles detected throughout the entire material, even in between the microbubbles. Therefore, it is reasonable to assume that the nucleation of nanobubbles started before 10 sec, and additional nucleation and ripening continuously occurred, which is in accordance with the hypothesis and previous experiments.

However, the foaming time should be carefully controlled, especially when only nanobubble are required. In other words, the process time becomes a critical point at the temperature above the T_g of the matrix. The foaming time should be presumably less than 20 sec for that purpose.

Since the microbubbles scatter light and make the sample opaque (white), the haze value was increased from 3.39 (foamed for 10 sec) to 89.0 (foamed for 30 sec).

The process factors that affect the thermodynamics of nucleation and growth of bubbles were optimized stepwise through this work and summarized in **Table 10**. First, UV lamp with a wavelength of 405 nm was used to pre-cure the film and keep the azo initiator unreacted at the same time. Second, AIBN was replaced by ABVN to accelerate gas generation. Third, surface tension was reduced by adding BYK 378 surfactant. Lastly, by controlling the foaming temperature and time, nanobubbles were achieved in the transparent PHEMA film (200 μm) on the microscope glass with the transmittance of 90.6 %.

Process condition		**Thermodynamic effect**
Monomer	HEMA	Pre-cured by using UV lamp (405 nm) unreacted ABVN in the pre-cured PHEMA
Photo initiator	Irgacure 819	
Blowing agent	ABVN (instead of AIBN)	***ΔP: supersaturation ↑***
Surfactant	BYK 378 (0.4 wt%)	***γ: surface tension ↓***
Foaming condition	Heating at 110 °C for 10 sec	***ΔP: supersaturation↑***

Table 10. Summary of process factors and thermodynamic effect on the nucleation of bubbles

5.2.7 Decomposition of ABVN by thermal heating and UV radiation

A UV lamp with the wavelength of 405 nm was used to make pre-cured PHEMA films in the previous experiments in order to keep AIBN unreacted. That is because AIBN has UV absorption ranges between 290 nm and 410 nm (λ_{max}: 347 nm) as shown in **Figure 45**. Likewise, other azo chemicals have similar absorption ranges, which λ_{max} at 350 nm is. That means, UV radiation with the wavelength around 350 nm could break the nitrogen double bond and accelerate the decomposition of azo chemicals, when it is combined with thermal heating.

The wavelength and intensity of the UV lamp (1000 W) used for the experiment are shown in **Figure 57** and **Table 11**. Since the maximum intensity of the lamp is 360 nm, close to 350 nm, more nitrogen generation was expected.

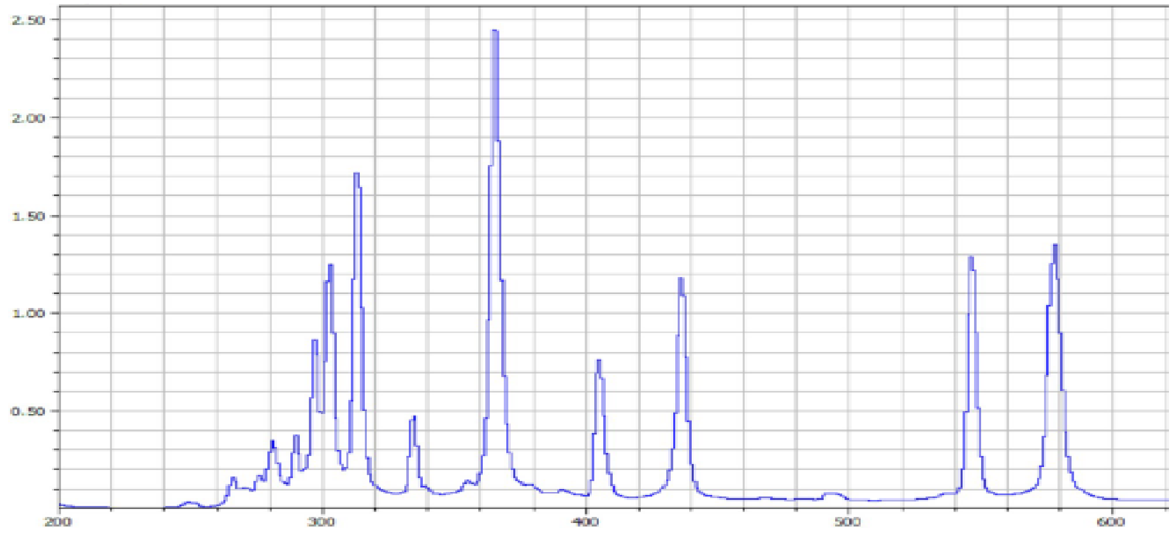

Figure 57. Wavelength and intensity of the UV lamp used for this experiment

UV range	**Intensity** (mW/cm^2)
UV-A	20,800
UV-B	18,200
UV-C	2,894
All	86,300

Table 11. Intensity of UV-A, B, C, and all wavelengths

Starting from liquid state sol

When the foaming starts from the liquid sol, the surface tension is the lowest, which is in favor of reducing the critical diameter of the nucleation of bubbles. On the other hand, due to the low viscosity of the matrix, diffusion and ripening could occur more aggressively. In addition, it took more time until the matrix is fully polymerized, while solidifying the bubbles, compared to the foaming from the pre-cured PHEMA. As a result, inhomogeneity and abnormal growth of bubbles were clearly visible.

For the effect of the combining UV lamp with thermal heating, it was confirmed that the density of nanobubbles increased, while the size of bubbles decreased (**Figure 42** and **Figure 43**). It indicates that the decomposition of ABVN was accelerated by UV radiation. Not only the amount of gas, but also the free radicals generated from ABVN could affect the polymerization kinetics, which result in fast solidification. Therefore, the bubbles would have less time for the ripening and growth.

Starting from partially cured PHEMA

Compared to the liquid sol, the partially cured sol has higher surface tension and viscosity (i.e. lower diffusivity). This implies both positive and negative effects on the formation of nanobubbles. Whereas higher surface tension requires more energy for the nucleation of bubbles, higher viscosity would slow down the diffusion, meaning that bubbles could not grow faster. Considering the fact that the size of the smaller bubbles did not change much and the bigger bubbles showed narrow size distribution and better homogeneity (**Figure 44**), the benefit of lower diffusivity seems to be greater than the disadvantage of increasing surface tension.

The process factors that affect the thermodynamics of nucleation and growth of bubbles in this chapter are summarized in **Table 12**.

Process condition		Thermodynamic effect
Monomer	HEMA	***γ: surface tension ↓*** *(compared to the fully cured PHEMA)*
Photo initiator	Irgacure 819	
Blowing agent	ABVN (instead of AIBN)	***ΔP: supersaturation ↑***
Surfactant	BYK 378 (0.4 wt%)	***γ: surface tension ↓***
Foaming condition	Heating 70 °C	***ΔP: supersaturation↑***
	High power UV (1000 W)	***ΔP: supersaturation↑***

Table 12. Summary of process factors and thermodynamic effects on the nucleation of bubbles

From the previous chapter, nanobubbles were produced by heating the pre-cured PHEMA film to the temperature above the T_g of the matrix. For the partially cured film, on the other hand, foaming was conducted below the T_g temperature, meaning less nitrogen was produced at lower temperature. Instead, UV lamp (1000 W) was added in order to accelerate the decomposition of ABVN. In addition, the partially cured PHEMA requires less energy for introducing a new interface between the matrix and bubble than the pre-cured PHEMA. It is worth to note that once the films turned slightly milky under the UV within 30 sec, there was no specific change in color for the rest of the time. It means no further nucleation or growth of the bubbles happened since the foaming temperature was below the T_g of PHEMA. The mean diameter of the bubbles, 175 nm after 2 min of foaming, indicates that no substantial growth occurred.

In conclusion, two different approaches, either above or below T_g, were optimized to achieve nanobubbles in the PHEMA film. Different optical properties from those approaches are summarized in **Table 13**. Furthermore, the refractive index of 1.44 means that there is 10 % volume fraction nitrogen gas by Lorentz-Lorenz equation in order to reduce the refractive index from 1.51.

For the possible applications, experimental parameters could be selected based on the thermodynamic considerations.

PHEMA film (200 µm) with bubbles on the microscope glass	Transmittance (%)	Haze (%)
Pre-cured PHEMA foamed at 110 °C for 10 sec	90.6	3.39
Partially cured PHEMA foamed at 70 °C + UV lamp	83.1	10.40

Table 13. Comparison of transmittance and haze values from PHEMA with nanobubbles under different process conditions

6. Possible applications

6.1 Embossing hologram security mark

6.1.1 Materials and methods

A PHEMA with embossed structure was prepared by using a commercial embossing foil as a master. A mixture of HEMA and Irgacure 819 was used to copy the structure from the master foil and fully cured by UV radiation. Another mixture of HEMA, Irgacure 819, BYK 378, and ABVN was filled in the embossed structure and sandwiched between two microscope slides as shown in **Scheme 9**. The foaming process was the same as optimized before, i.e. 2 min by UV radiation (405 nm) followed by the combination of thermal heating at 70 °C and high-power UV radiation (1000 W) for 1 min.

In addition, the sample was tested if specific diffraction patterns are observed when laser goes through the patterned area as shown in **Scheme 10**. The microstructure and distribution of the nanobubbles was characterized by using SEM.

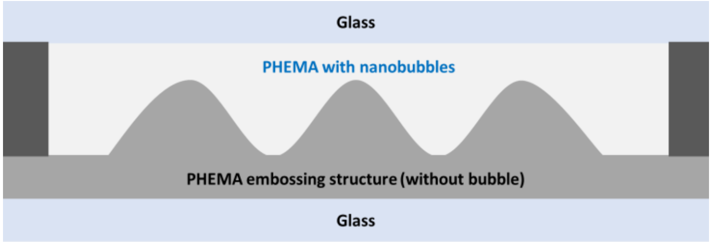

Scheme 9. Experimental set up for the security mark _ invisible embossing structure

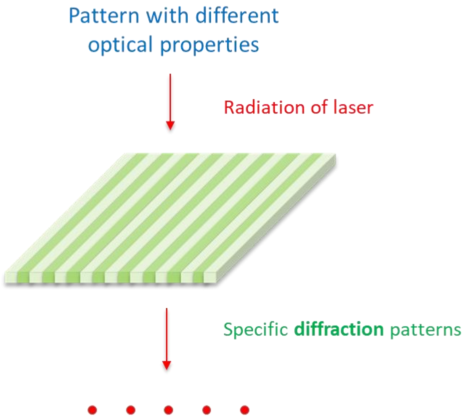

Scheme 10. Diffraction patterns depending on the microstructure of the dense and porous area

6.1.2. Results

The security mark coating containing nanobubbles in the embossing structure was transparent and objects behind the coating could be seen clearly as shown in **Figure 58**. However, the linear structure of the master embossing structure was hard to be detected by naked eyes. Apparently, it seems to be a homogeneous and clear coating.

Figure 58. Photo of the transparent embossing security mark (blue circle)

However, a linear diffraction pattern appeared on the screen when the red laser light went through the sample as shown in **Figure 59**.

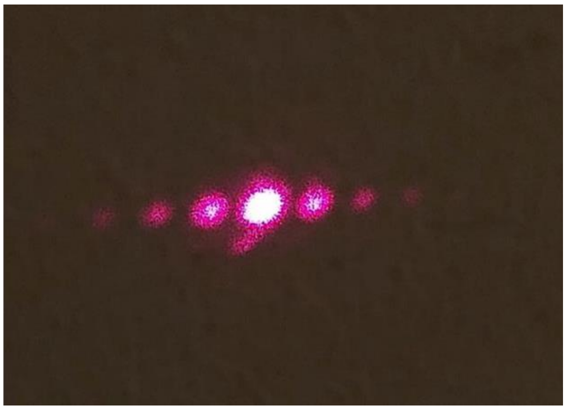

Figure 59. Diffraction patterns on the black screen by red color laser

From the SEM images in **Figure 60**, it is clear that the two areas have different microstructure and contrast. Nanobubbles were generated in the upper part of the porous PHEMA layer, while no bubble was detected in the bottom area. Nanobubbles in the range of 50 -100 nm were detected as shown in **Figure 61**.

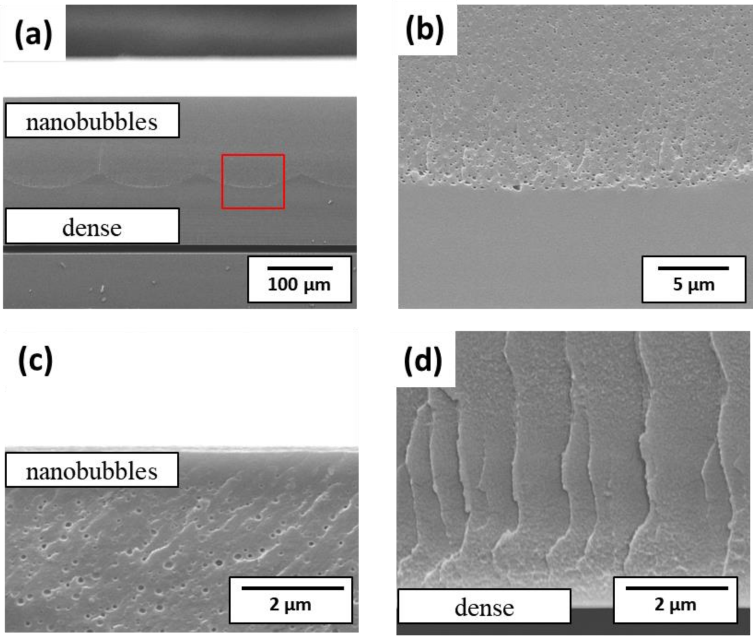

Figure 60. SEM images of embossing security PHEMA film (a); overview, (b); boundary between dense and porous area from red rectangle in (a), (c), (d); high magnification of porous PHEMA with nanobubbles and dense area

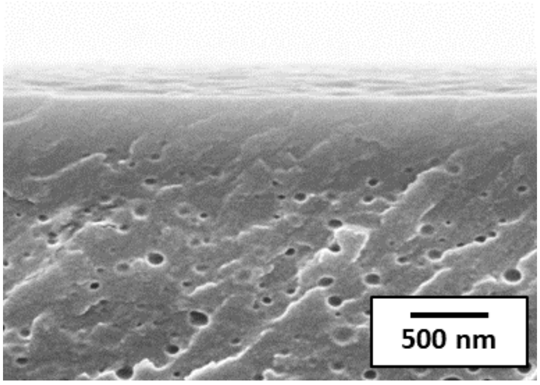

Figure 61. High magnification of Figure 37 (c)

6.1.3 Discussion

The embossing security mark (200 μm) composes of nearly half of the dense PHEMA without bubble and the porous PHEMA with nanobubbles (**Figure 60**) in the structure. Considering that the transmittance of the dense PHEMA and porous PHEMA of 200 μm thickness were 93.8 and 83.1, respectively, the coating with the two mixed materials could remain transparent as shown in **Figure 58**. In other words, the security mark is a regular arrangement of the more transparent and less transparent materials. Therefore, it is difficult to see the embossed structure, although there is a regular distance of around 100 μm within the structure. That is why this type of coating could be used as 'invisible security mark'.

However, the two parts of the coating have different refractive index of 1.51 without bubble, and 1.44 with nanobubbles. Therefore, these 'structural information' could be easily detected by using laser as shown in **Scheme 10** and **Figure 59**. Since diffraction patterns caused by interference depend on the microstructure of the materials that have different refractive index, various diffraction patterns could be achieved by changing the internal structure of the materials. For example, 3D microstructure could be also achieved either by using interconnected 3D master structure or by making multilayer coating. It is proven further that nanobubbles could be fabricated in a layer less than 10 μm (data not shown), which means 4-5 different structured coating layers could be embedded in a transparent coating of around 50 μm. Moreover, the surface of the coating is flat as shown in **Figure 60** and **Figure 61**. It indicates that it is impossible to copy this internal information by camera or copy machine. In other words, it is invisible information from the 'internal microstructure'. Therefore, this type of security mark has numerous potential applications such as transparent coating in direction of digital information technology (IT) device.

The main advantages of this application seem to be relatively lower cost and shorter process time compared to other techniques. When preparing different microstructure, only a simple process with minor tuning of the starting monomer solution (i.e. addition of ABVN and surfactant) followed by UV radiation and heating would be required. In addition, it is

considered to be very cost-effective, even compared to the process of fabricating neat polymers without bubble.
Moreover, the entire process of making two different micro structured layers took less than 10 min (less than 5 min for each layer) in this application when the two mixtures are prepared by hand. Besides, no further process such as extraction or evaporation of unwanted part is needed after foaming.

Therefore, this process seems promising for various industry applications in terms of cost-effectiveness and producibility.

6.2 Light out-coupling scattering point in optical waveguide

6.2.1 Materials and methods

A PLA (polylactic acid) optical wave guide with 400 µm was 3D printed. The end tip of the PLA wire was hand dip coated in a mixture of HEMA, Irgacure 819, BYK 378, and ABVN. The dip coated PLA wire was transferred to the N_2 flowing chamber and hold horizontally. The coated area was UV (1000 W) radiated while the wire is continuously rotating as shown in **Scheme 11**.

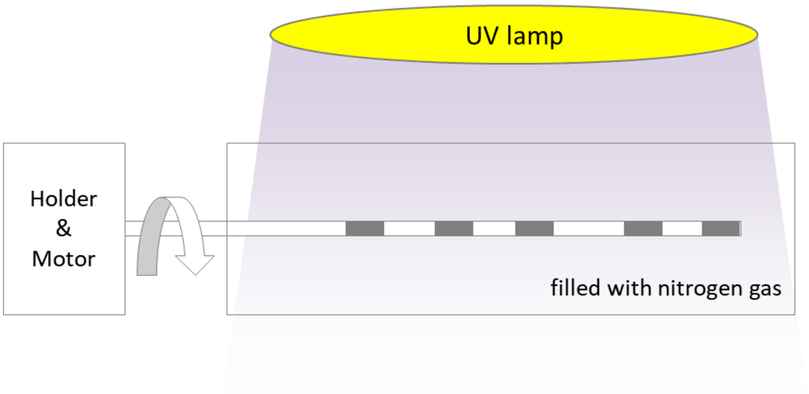

Scheme 11. Preparation of the PLA optical wave guide with nanobubbles

Out-coupling efficiency was quantitatively measured by in-coupling green laser into the fiber and the scattering effect was demonstrated as shown in **Scheme 12**. The sample was characterized for the size and distribution of the bubbles by using SEM.

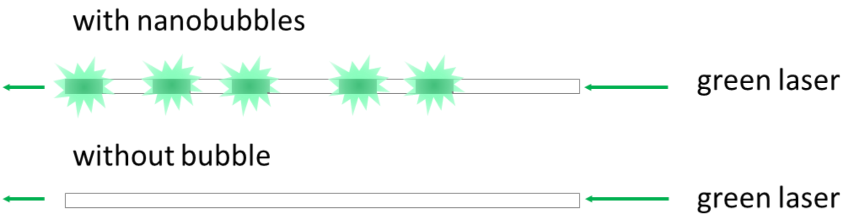

Scheme 12. Demonstration of the scattering effect by nanobubbles in the PLA optical fiber

6.2.2 Results

The coated areas by PHEMA with nanobubbles turned white after foaming as shown in **Figure 62** (a). Sub-micron sized bubbles were detected near the fiber **Figure 62** (c), while relatively bigger microbubbles (1 – 2 μm) with less density were found near the surface **Figure 62** (d).

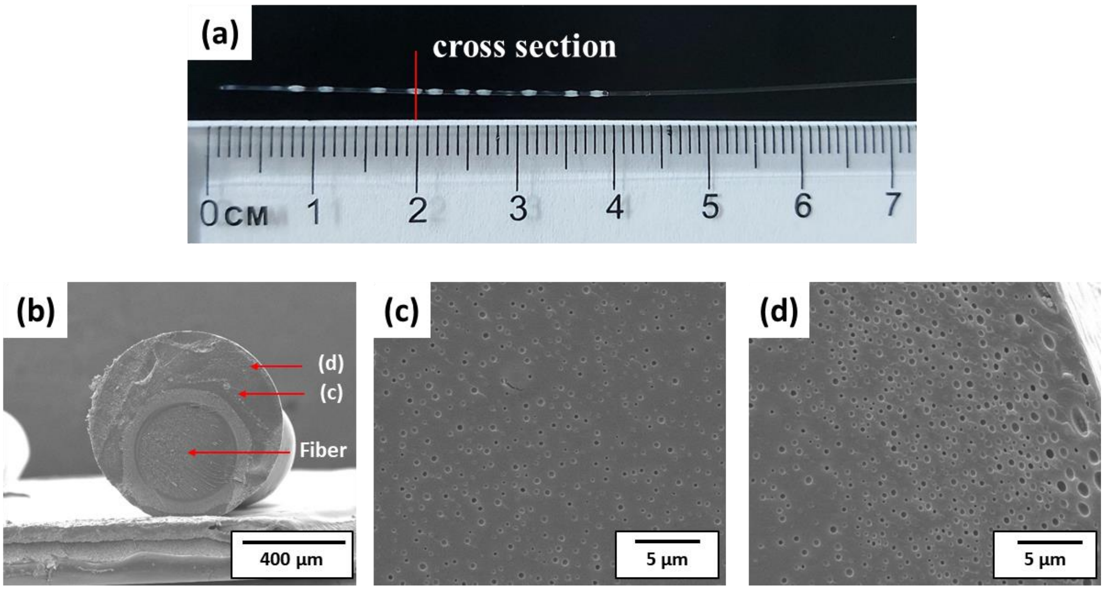

Figure 62. (a); Photo of PLA optical fiber with nanobubbles (white spots), (b) SEM cross section of the fiber, (c) and (d); high magnification of the area shown in (b)

Figure 63 shows that the bubbles in the PHEMA work as a light out-coupling scattering point. Compared to the PLA fiber without bubble, which shows no scattering except at the end tip (b), the green laser scattered at the points corresponding to the coating layer with bubbles.

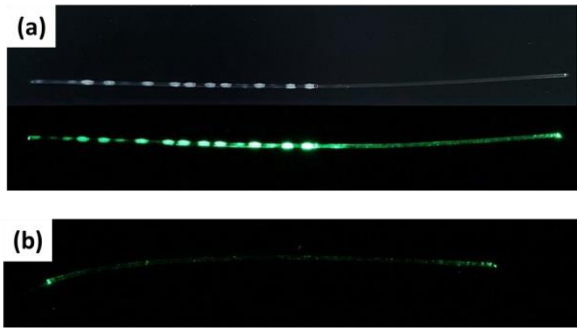

Figure 63. (a); Light out-coupling scattering effect by nanobubbles, (b) control sample without bubble

6.2.3 Discussion

Demand for light out-coupling in medical applications has been increased recently since medical treatment or reaction could be triggered by light in the human body. However, as described in the literature research, a proper method to introduce sub-microbubbles has not been developed. Besides, using nanoparticles for medical applications does not seem promising. Recently, Shabahang et al. reported thermally induced microbubbles in polyethersulfone (PES) optical fibers for custom side-scattering profiles [88]. However, a PES fiber that absorbs water vapor from atmosphere needed to be heated up to 150 – 200 °C so that microbubbles could be formed by evaporation of the absorbed moisture. Furthermore, this procedure is not suitable for other materials that do not absorb moisture from the air or have low T_g temperature.

In this experiment, the PLA fiber was simply dip coated and the foaming process was performed at room temperature without thermal heating. The T_g temperature of the PLA fiber is around 35 °C, which imply that this material becomes flexible in human body and can be applied to various medical applications. However, thermally induced foaming of the PLA fiber is not proper for this purpose. To our knowledge, there has been no report regarding such technique of introducing sub-micron bubbles at room temperature, even in a short period of time.

From the SEM measurement and demonstration by green laser, it was shown that nanobubbles in PHEMA film efficiently work as scattering points. There was clear difference between the fiber with nanobubbles and without out-coupling coating (**Figure 63**). The amount of the scattered light could be tuned by changing the thickness of the out-coupling coating or by changing the size of the bubbles. Furthermore, the distance between each scattering point could be controlled by dropping the sol at the specific point, which would lead to a customized light out-coupling fiber system in the future as shown in **Scheme 13**. Besides, similar as the application above (6.1), out-coupling points could be designed during the fabrication of the optical fiber as shown in **Scheme 14**. If bubbles are generated as small spot, it could be also used as in-coupling scattering window so that light could be delivered into the fiber, which broadens the feasibility of this technique further.

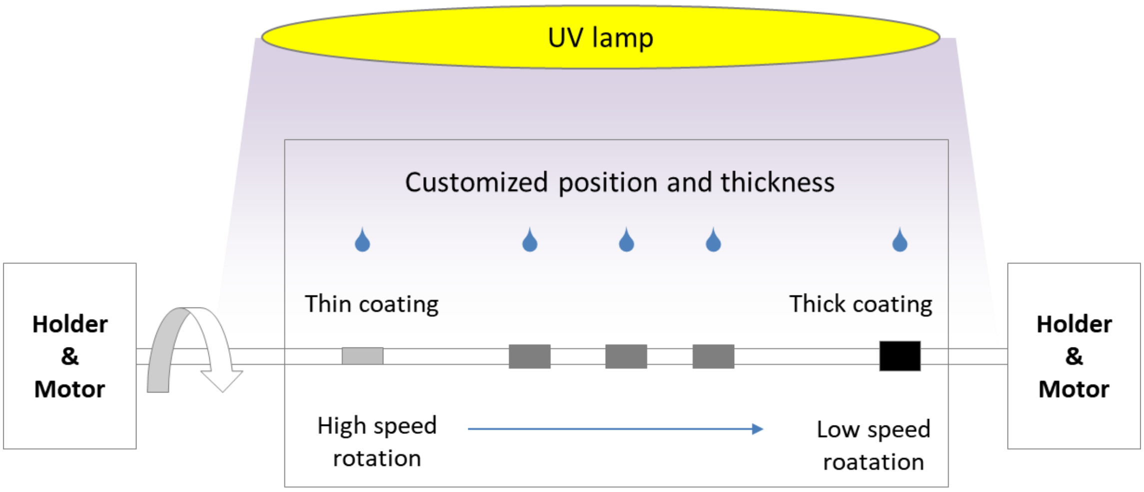

Scheme 13. Possible way of making customized light out-coupling optical fiber

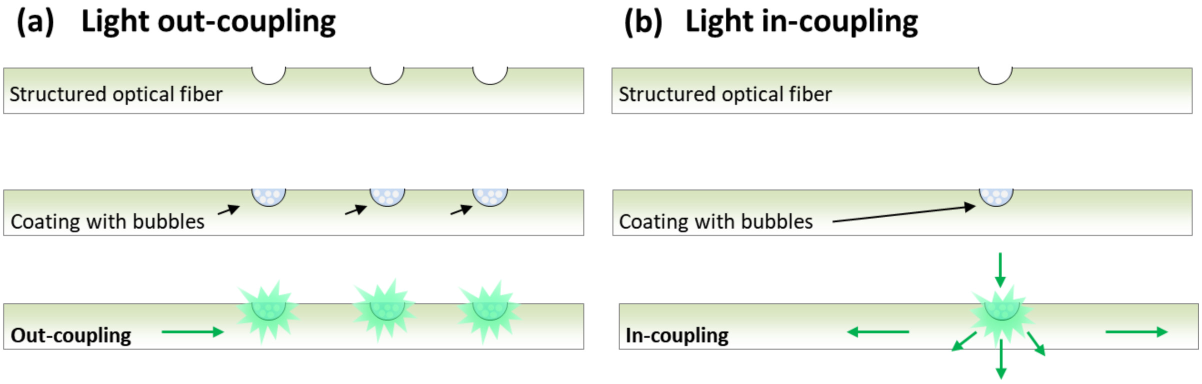

Scheme 14. (a) Light out-coupling, (b) in-coupling point by nanobubbles

7. Summary and outlook

Azo initiators like AIBN and ABVN were used in this work as a chemical blowing agent to generate nanobubbles in a transparent PHEMA film. Compared to other chemical blowing agents used for extrusion or injection molding that decompose at high temperature around 200 °C, AIBN and ABVN could decompose by UV irradiation or thermal heating at relatively low temperature, around 60 °C or below. In order to keep azo initiators unreacted during the polymerization process, additional photo initiator and UV lamp with specific wavelength (405 nm) were used for preparing UV cured-PHEMA film or partially cured solution. Bubbles were foamed afterwards by heating the film under various conditions. The effects of temperature, pressure, a surface constraining layer, and surfactants on the nucleation and growth of the bubbles in the film were evaluated based on the thermodynamics and conventional nucleation theory (CNT). Previous reports from other researchers about the super critical foaming by CO_2 were often used for discussion in order to understand the mechanism of the nucleation and growth for each experiment.

It was found that both, reducing the surface tension of the matrix and increasing the degree of the supersaturation were crucial factors to fabricate nanobubbles in the film. In other words, the combination of adding the surfactant BYK 378, using ABVN instead of AIBN, and controlling the foaming conditions, i.e. time and temperature, resulted in nanobubbles in the film. In addition, the surface constraining layer, which prevents nitrogen from diffusion, and gas soaking helped further to increase the nucleation of the bubbles. Finally, I optimized those critical factors and found two possible ways to achieve the nanobubbles. One that starts from the UV-cured film and the other one that starts from the partially cured sol depending on the foaming temperature, i.e. 110 °C and 70 °C, respectively. The mean diameter of bubbles under the optimized conditions was 120 nm and 175 nm for the two conditions. The films of 200 μm thickness on the microscope glass have transmittance of 93.8 and 83.1, respectively. The existence of nanobubbles and their shape were clearly visualized by SEM. It is worth to note that the entire process time for this process was about 5 min or below and does not require high pressure or any further treatment. This kind of technique has not been reported yet.

I tested the transparent film with micro and nanobubbles for various applications such as security mark and out-coupling for optical fibers. They are shown in chapter 6.1 and 6.2.
For the invisible security coating, it remained transparent after the foaming of the nanobubbles. The structural information could be easily detected by using laser pointer although nothing was detected with naked eyes.
For the light out-coupling application, it was also qualitatively demonstrated that nanobubbles could work as scattering points. The fabrication process was very fast and could be conducted at room temperature.

There are more possibilities to reduce the refractive index further. For example, addition of nanoparticles and cross-linking agents would also increase the heterogeneous nucleation sites of bubbles or hinder the diffusion of the gas. Co-polymerization or patterning the structure of the polymer matrix would be very interesting as well. Lastly, mixed physical/chemical blowing agents combined with conventional supercritical CO_2 would be a new field of research based on these experiments. The size and density of the bubbles from those possible applications could be tuned depending on their purposes by manipulating process parameters as it was shown in this study.

A wide range of the new approach is also expected in UV curable polymer system. Although only HEMA monomer and PHEMA systems are reported in this study, azo initiators are widely used in polymer synthesis and soluble in various solvents such as acetone, ethyl acetate, and toluene. Therefore, this approach would work for other polymer systems including PMMA. This could open a new door to various applications in every field of material science.

Finally, this study would bring also more insights for the thermodynamic discussion of the existence and stability of isolated nanobubbles in metastable states or in polymers. In particular, starting from the clear demonstration of the nanobubbles, a series of sequential steps such as ripening of the bubbles, and expansion of the matrix, give comprehensive information to validate each process of foaming.

Reference

1. Alheshibri, M., et al., *A History of Nanobubbles.* Langmuir, 2016. **32**(43): p. 11086-11100.
2. Miyazaki, D., *Fresnel Equations*, in *Computer Vision: A Reference Guide*, K. Ikeuchi, Editor. 2014, Springer US: Boston, MA. p. 305-307.
3. Mitchell, B.S., *An Introduction to Materials Engineering and Science: For Chemical and Materials Engineers.* John Wiley & Sons, In., 2004: p. 900 - 902.
4. S.Glasstone, *Text book of Physical Chemistry, IInd ed.* . D. Van Nostrand Company Inc., New York, 1946.
5. Imai, Y., *Inorganic Nano-fillers for Polymers*, in *Encyclopedia of Polymeric Nanomaterials*, S. Kobayashi and K. Müllen, Editors. 2021, Springer Berlin Heidelberg: Berlin, Heidelberg. p. 1-7.
6. Hu, Y., et al., *Preparation and properties of transparent PMMA/ZrO2 nanocomposites using 2-hydroxyethyl methacrylate as a coupling agent.* Polymer, 2011. **52**(1): p. 122-129.
7. Garnweitner, G., et al., *Large-Scale Synthesis of Organophilic Zirconia Nanoparticles and their Application in Organic–Inorganic Nanocomposites for Efficient Volume Holography.* Small, 2007. **3**(9): p. 1626-1632.
8. Luo, K., S. Zhou, and L. Wu, *High refractive index and good mechanical property UV-cured hybrid films containing zirconia nanoparticles.* Thin Solid Films, 2009. **517**(21): p. 5974-5980.
9. Groh, W. and A. Zimmermann, *What is the lowest refractive index of an organic*

polymer? Macromolecules, 1991. **24**(25): p. 6660-6663.

10. Harvey, A.H., S.G. Kaplan, and J.H. Burnett, *Effect of Dissolved Air on the Density and Refractive Index of Water.* International Journal of Thermophysics, 2005. **26**(5): p. 1495-1514.

11. Ahn Nguyen, H.J.S., *colloidal science of flotation.* 2003.

12. Pallas, N.R.a.H., Y, *Colloids and Surfaces* 1990: p. 169-194.

13. Epstein, P.S. and M.S. Plesset, *On the Stability of Gas Bubbles in Liquid-Gas Solutions.* The Journal of Chemical Physics, 1950. **18**(11): p. 1505-1509.

14. JOHNSON, B.D. and R.C. COOKE, *Generation of Stabilized Microbubbles in Seawater.* Science, 1981. **213**(4504): p. 209-211.

15. Bunkin, N. and F.V. Bunkin, *Bubstons are stable gas microbubbles in highly diluted solutions of electrolytes.* Zhurnal Eksperimentalnoi i Teoreticheskoi Fiziki, 1992. **101**: p. 512-527.

16. Bunkin, N., et al., *Existence of charged submicrobubble clusters in polar liquids as revealed by correlation between optical cavitation and electrical conductivity.* Colloids and Surfaces A: Physicochemical and Engineering Aspects, 1996. **110**: p. 207-212.

17. Kim, J.-Y., M.-G. Song, and J.-D. Kim, *Zeta Potential of Nanobubbles Generated by Ultrasonication in Aqueous Alkyl Polyglycoside Solutions.* Journal of Colloid and Interface Science, 2000. **223**(2): p. 285-291.

18. Kikuchi, K., et al., *Characteristics of hydrogen nanobubbles in solutions obtained with water electrolysis.* Journal of Electroanalytical Chemistry, 2007. **600**(2): p. 303-310.

19. Kikuchi, K., et al., *Concentration determination of oxygen nanobubbles in electrolyzed water.* Journal of Colloid and Interface Science, 2009. **329**(2): p. 306-309.

20. Ohgaki, K., et al., *Physicochemical approach to nanobubble solutions.* Chemical Engineering Science - CHEM ENG SCI, 2010. **65**: p. 1296-1300.

21. Uchida, T., et al., *Transmission electron microscopic observations of nanobubbles and their capture of impurities in wastewater.* Nanoscale Research Letters, 2011. **6**(1): p. 295.

22. Barbara Pabin-Szafko , E.W.a.Z.C., *Selected radical azoinitiators in the synthesis of solvent-borne acrylic pressure-sensitive adhesives.* Chemistry & chemical technology, 2009. **13**.

23. Zhao, Q.-L., et al., *Photoinduced ICAR ATRP of Methyl Methacrylate with AIBN as Photoinitiator.* Journal of Polymer Research, 2014. **21**(5): p. 444.

24. Chen, S., L. Jiang, and Y. Dan, *Preparation and thermal response behavior of poly(N-isopropylacrylamide-co-a crylic acid) microgels via soap-free emulsion polymerization based on AIBN initiator.* Journal of Applied Polymer Science, 2011. **121**(6): p. 3322-3331.

25. Paljevac, M., et al., *Two-step syneretic formation of highly porous morphology during copolymerization of hydroxyethyl methacrylate and ethylene glycol dimethylacrylate.* Materials Today Communications, 2016. **7**.

26. Přádný, M., et al., *macroporous hydrogels based on 2-hydroxyethyl methacrylate. Part 7: Methods of preparation and comparison of resulting physical properties.* e-Polymers, 2010. **10**(1).

27. Guo, L.-Z., et al., *Application of azodiisobutyronitrile and azobisisoheptonitrile in*

low-density unsaturated polyester resin manufacturing. Journal of Applied Polymer Science, 2014. **131**(10).

28. Weber, H., De Grave, I., Röhrl, E. and Altstädt, V. , *Foamed Plastics*, in *Ullmann's Encyclopedia of Industrial Chemistry*. 2016. p. 1-54.

29. Han, C.D., Y.W. Kim, and K.D. Malhotra, *A study of foam extrusion using a chemical blowing agent.* Journal of Applied Polymer Science, 1976. **20**(6): p. 1583-1595.

30. Krutko, I., I. Danylo, and V. Kaulin, *Kinetics of azodicarbonamide decomposition in the presence of an initiator for obtaining solid foams.* Voprosy Khimii i Khimicheskoi Tekhnologii, 2019: p. 26-34.

31. Park, H.E. and J.M. Dealy, *Effects of Pressure and Supercritical Fluids on the Viscosity of Polyethylene.* Macromolecules, 2006. **39**(16): p. 5438-5452.

32. Ushiki, I., et al., *Solubilities and diffusion coefficients of carbon dioxide and nitrogen in poly(methyl methacrylate) at high temperatures and pressures.* The Journal of Supercritical Fluids, 2019. **152**: p. 104565.

33. Witkowski, A., M. Majkut, and S. Rulik, *Analysis of pipeline transportation systems for carbon dioxide sequestration.* Archives of Thermodynamics, 2014(No 1 March): p. 117-140.

34. Okolieocha, C., et al., *Microcellular to nanocellular polymer foams: Progress (2004–2015) and future directions – A review.* European Polymer Journal, 2015. **73**: p. 500-519.

35. *Glass Transitions in Polymer C02 Mixtures at Elevated Pressures.* Journal of Polymer Science: Part B: Polymer Physics, 1991. **29**: p. 631.

36. Bos, A., et al., *CO2-induced plasticization phenomena in glassy polymers.* Journal of

Membrane Science, 1999. **155**(1): p. 67-78.

37. Hachisuka, H., et al., *Glass Transition Temperature of Glassy Polymers Plasticized by CO2 Gas.* Polymer Journal, 1990. **22**(1): p. 77-79.

38. Tsivintzelis, I., A.G. Angelopoulou, and C. Panayiotou, *Foaming of polymers with supercritical CO2: An experimental and theoretical study.* Polymer, 2007. **48**(20): p. 5928-5939.

39. Tsivintzelis, I., et al., *Foaming of polymers with supercritical fluids: A thermodynamic investigation.* The Journal of Supercritical Fluids, 2016. **110**: p. 240-250.

40. Guo, H. and V. Kumar, *Solid-state poly(methyl methacrylate) (PMMA) nanofoams. Part I: Low-temperature CO2 sorption, diffusion, and the depression in PMMA glass transition.* Polymer, 2014. **57**.

41. Guo, H., A. Nicolae, and V. Kumar, *Solid-state poly(methyl methacrylate) (PMMA) nanofoams. Part II: Low-temperature solid-state process space using CO2 and the resulting morphologies.* Polymer, 2015. **70**: p. 231-241.

42. Nawaby, A.V., et al., *Polymer–CO2 systems exhibiting retrograde behavior and formation of nanofoams.* Polymer International, 2007. **56**(1): p. 67-73.

43. Forest, C., et al., *CO2 nano-foaming of nanostructured PMMA.* Polymer, 2015. **58**: p. 76-87.

44. Reglero Ruiz, J.A., et al., *Low-Density Nanocellular Foams Produced by High-Pressure Carbon Dioxide.* Macromolecular Materials and Engineering, 2011. **296**(8): p. 752-759.

45. Pinto, J., et al., *Nanocellular CO2 foaming of PMMA assisted by block copolymer nanostructuration.* Chemical Engineering Journal, 2014. **243**: p. 428-435.

46. Pinto, J., et al., *Block Copolymers Self-Assembly Allows Obtaining Tunable Micro or Nanoporous Membranes or Depth Filters Based on PMMA; Fabrication Method and Nanostructures.* The Journal of Physical Chemistry C, 2014. **118**(9): p. 4656-4663.

47. Pinto, J., et al., *Temperature influence and CO2 transport in foaming processes of poly(methyl methacrylate)-block copolymer nanocellular and microcellular foams.* Journal of Supercritical Fluids The, 2014. **94**.

48. Dumon, M., et al., *Block Copolymer-Assisted Microcellular Supercritical CO2 Foaming of Polymers and Blends.* Cellular Polymers, 2012. **31**(4): p. 207-222.

49. Yokoyama, B.H., et al., *Tunable Nanocellular Polymeric Monoliths Using Fluorinated Block Copolymer Templates and Supercritical Carbon Dioxide.* Advanced Materials, 2004. **16**(17): p. 1542-1546.

50. Yokoyama, H. and K. Sugiyama, *Nanocellular Structures in Block Copolymers with CO2-philic Blocks Using CO2 as a Blowing Agent: Crossover from Micro- to Nanocellular Structures with Depressurization Temperature.* Macromolecules, 2005. **38**(25): p. 10516-10522.

51. Taki, K., Y. Waratani, and M. Ohshima, *Preparation of Nanowells on a PS-b-PMMA Copolymer Thin Film by CO2 Treatment.* Macromolecular Materials and Engineering, 2008. **293**(7): p. 589-597.

52. Shirvan, M.M.M., M. Famili, and A. Golbang, *A Review on the Application of Nucleation Theories in Thermoplastic Foams.* Plastic and Polymer Technology, 2016. **4**: p. 11-32.

53. Janani, H. and M.H.N. Famili, *Investigation of a strategy for well controlled inducement of microcellular and nanocellular morphologies in polymers.* Polymer

Engineering & Science, 2010. **50**(8): p. 1558-1570.

54. Tomasko, D., et al., *Development of CO 2 for polymer foam applications.* Journal of Supercritical Fluids - J SUPERCRIT FLUID, 2009. **47**: p. 493-499.

55. Le Droumaguet, B., et al., *Engineering functional doubly porous PHEMA-based materials.* Polymer, 2014. **55**(1): p. 373-379.

56. Liu, Q., et al., *Preparation of Macroporous Poly(2-Hydroxyethyl Methacrylate) Hydrogels by Enhanced Phase Separation.* Biomaterials, 2000. **21**: p. 2163-9.

57. Lazzari, M. and M.A. López-Quintela, *Block Copolymers as a Tool for Nanomaterial Fabrication.* Advanced Materials, 2003. **15**(19): p. 1583-1594.

58. Nisticò, R., *Block copolymers for designing nanostructured porous coatings.* Beilstein Journal of Nanotechnology, 2018. **9**: p. 2332-2344.

59. Matsen, M.W. and F.S. Bates, *Unifying Weak- and Strong-Segregation Block Copolymer Theories.* Macromolecules, 1996. **29**(4): p. 1091-1098.

60. Lynd, N.A., A.J. Meuler, and M.A. Hillmyer, *Polydispersity and block copolymer self-assembly.* Progress in Polymer Science, 2008. **33**(9): p. 875-893.

61. Pulko, I. and P. Krajnc, *High internal phase emulsion templating--a path to hierarchically porous functional polymers.* Macromol Rapid Commun, 2012. **33**(20): p. 1731-46.

62. Kovačič, S., D. Štefanec, and P. Krajnc, *Highly Porous Open-Cellular Monoliths from 2-Hydroxyethyl Methacrylate Based High Internal Phase Emulsions (HIPEs): Preparation and Void Size Tuning.* Macromolecules, 2007. **40**(22): p. 8056-8060.

63. Pulko, I., et al., *Emulsion templated open porous membranes for protein purification.* Journal of Chromatography A, 2011. **1218**(17): p. 2396-2401.

64. Butler, R., C. M. Davies, and A. I. Cooper, *Emulsion Templating Using High Internal Phase Supercritical Fluid Emulsions*. Vol. 13. 2001. 1459-1463.

65. Butler, R., I. Hopkinson, and A.I. Cooper, *Synthesis of Porous Emulsion-Templated Polymers Using High Internal Phase CO2-in-Water Emulsions.* Journal of the American Chemical Society, 2003. **125**(47): p. 14473-14481.

66. Kimmins, S.D. and N.R. Cameron, *Functional Porous Polymers by Emulsion Templating: Recent Advances.* Advanced Functional Materials, 2011. **21**(2): p. 211-225.

67. Parale, V., K.-Y. Lee, and H.-H. Park, *Flexible and Transparent Silica Aerogels: An Overview.* Journal of the Korean Ceramic Society, 2017. **54**: p. 184-199.

68. Hegde, N.D. and A. Venkateswara Rao, *Organic modification of TEOS based silica aerogels using hexadecyltrimethoxysilane as a hydrophobic reagent.* Applied Surface Science, 2006. **253**(3): p. 1566-1572.

69. Mahadik, D.B., et al., *Elastic and Superhydrophobic Monolithic Methyltrimethoxysilane-based Silica Aerogels by Two-step Sol-gel Process.* 2016. **23**.

70. Shimizu, T., et al., *Transparent, Highly Insulating Polyethyl- and Polyvinylsilsesquioxane Aerogels: Mechanical Improvements by Vulcanization for Ambient Pressure Drying.* Chemistry of Materials, 2016. **28**(19): p. 6860-6868.

71. Handa, Y.P. and Z. Zhang, *A new technique for measuring retrograde vitrification in polymer–gas systems and for making ultramicrocellular foams from the retrograde phase.* Journal of Polymer Science Part B: Polymer Physics, 2000. **38**(5): p. 716-725.

72. Bishop, T.E., *Multiple Photoinitiators for Improved Performance.*

73. THORLABS, *M405LP1-C5 - 405 nm, 570 mW (Typ.) Collimated LED for Nikon*

Eclipse, 1400 mA 2015.

74. Wako, <*wako_azo_polymerization_initiators_catalog_25.pdf*>.

75. Xu, Z.-M., et al., *Foaming of polypropylene with supercritical carbon dioxide.* The Journal of Supercritical Fluids, 2007. **41**(2): p. 299-310.

76. Krause, B., et al., *Microcellular Foaming of Amorphous High-Tg Polymers Using Carbon Dioxide.* Macromolecules, 2001. **34**(4): p. 874-884.

77. Siripurapu, S., et al., *Low-Temperature, Surface-Mediated Foaming of Polymer Films.* Advanced Materials, 2004. **16**(12): p. 989-994.

78. Famili, M.H.N., H. Janani, and M.S. Enayati, *Foaming of a polymer–nanoparticle system: Effect of the particle properties.* Journal of Applied Polymer Science, 2011. **119**(5): p. 2847-2856.

79. Pinto, J., et al., *Nanoporous PMMA foams with templated pore size obtained by localized in situ synthesis of nanoparticles and CO2 foaming.* Polymer, 2017. **124**: p. 176-185.

80. Monnereau, L., et al., *Supercritical CO2 and polycarbonate based nanocomposites: A critical issue for foaming.* Polymer, 2014. **55**(10): p. 2422-2431.

81. Costeux, S. and L. Zhu, *Low density thermoplastic nanofoams nucleated by nanoparticles.* Polymer, 2013. **54**(11): p. 2785-2795.

82. Siripurapu, S., et al., *Controlled Foaming of Polymer Films through Restricted Surface Diffusion and the Addition of Nanosilica Particles or CO2-philic Surfactants.* Macromolecules, 2005. **38**(6): p. 2271-2280.

83. Jose Antonio Reglero Ruiz, P.V., Michel Dumon, *Foaming Behaviour and Compressive Properties of Microcellular Nanostructured Polystyrene.* Cellular

Polymers, 2009. **28**(6): p. 363.

84. Li, L., et al., *CO2 Foaming in Thin Films of Block Copolymer Containing Fluorinated Blocks.* Macromolecules, 2006. **39**(14): p. 4746-4755.

85. Hirao, A., K. Sugiyama, and H. Yokoyama, *Precise synthesis and surface structures of architectural per- and semifluorinated polymers with well-defined structures.* Progress in Polymer Science, 2007. **32**(12): p. 1393-1438.

86. Han, X., et al., *CO2 foaming based on polystyrene/poly(methyl methacrylate) blend and nanoclay.* Polymer Engineering & Science, 2007. **47**(2): p. 103-111.

87. Zhang, R., et al., *Thermally robust nanocellular thin films of high-Tg semifluorinated block copolymers foamed with supercritical carbon dioxide.* Soft Matter, 2011. **7**(8).

88. Shabahang, S., S. Forward, and S.-H. Yun, *Polyethersulfone optical fibers with thermally induced microbubbles for custom side-scattering profiles.* Optics express, 2019. **27**(5): p. 7560-7567.